2014

# THE NATURE AND ORIGIN OF CYCLICITY IN THE CLEVELAND MEMBER OF THE OHIO SHALE (UPPER DEVONIAN), NORTHEASTERN KENTUCKY, U.S.A.

Alice C. O'Bryan
*University of Kentucky*, obryana1@gmail.com

**STUDENT AGREEMENT:**

I represent that my thesis or dissertation and abstract are my original work. Proper attribution has been given to all outside sources. I understand that I am solely responsible for obtaining any needed copyright permissions. I have obtained needed written permission statement(s) from the owner(s) of each third-party copyrighted matter to be included in my work, allowing electronic distribution (if such use is not permitted by the fair use doctrine) which will be submitted to UKnowledge as Additional File.

I hereby grant to The University of Kentucky and its agents the irrevocable, non-exclusive, and royalty-free license to archive and make accessible my work in whole or in part in all forms of media, now or hereafter known. I agree that the document mentioned above may be made available immediately for worldwide access unless an embargo applies.

I retain all other ownership rights to the copyright of my work. I also retain the right to use in future works (such as articles or books) all or part of my work. I understand that I am free to register the copyright to my work.

**REVIEW, APPROVAL AND ACCEPTANCE**

The document mentioned above has been reviewed and accepted by the student's advisor, on behalf of the advisory committee, and by the Director of Graduate Studies (DGS), on behalf of the program; we verify that this is the final, approved version of the student's thesis including all changes required by the advisory committee. The undersigned agree to abide by the statements above.

Alice C. O'Bryan, Student

Dr. Frank R. Ettensohn, Major Professor

Dr. Edward W. Woolery, Director of Graduate Studies

# THE NATURE AND ORIGIN OF CYCLICITY IN THE CLEVELAND MEMBER OF THE OHIO SHALE (UPPER DEVONIAN), NORTHEASTERN KENTUCKY, U.S.A.

---

THESIS

---

A thesis submitted in partial fulfillment of the requirements for the degree of Master of Science in the College of Arts and Sciences at the University of Kentucky

By
Alice C. O'Bryan
Lexington, Kentucky

Director:
Dr. Frank R. Ettensohn, Professor of Earth and Environmental Sciences
Lexington, Kentucky
2014

ABSTRACT OF THESIS

# THE NATURE AND ORIGIN OF CYCLICITY IN THE CLEVELAND MEMBER OF THE OHIO SHALE (UPPER DEVONIAN), NORTHEASTERN KENTUCKY, U.S.A.

The Cleveland Shale displays a characteristic and distinctive pattern of promontories and recessed intervals on weathered outcrops, which appears to represent cyclicity. This weathering pattern can be observed in other shales, both within and outside the Appalachian Basin; so determining the nature of these cycles may be critical for understanding the origin of, not only the Cleveland Shale, but also of black shales in general. Cyclicity in the Cleveland was examined on a decimeter-to-meter scale using lithologic characterization, gamma-ray stratigraphy and x-ray fluorescence, and on a millimeter-to-centimeter scale using organic petrography. Lithologic characterization and gamma-ray stratigraphy revealed Milankovitch-band fourth- and fifth-order cyclicity related to changes in the earth's orbital eccentricity (100 ka) and obliquity of the earth's axis (42 ka), respectively. Sedimentological changes associated with these cycles were identified through organic petrography and x-ray fluorescence. A depositional model was developed from these data sets, which suggests that cyclic changes in local climate — from cold and wet to warm and dry — controlled advancing and retreating glaciation in the adjacent Acadian mountains as well as concomitant sea-level rise and fall in the Black-Shale Sea. Such changes would have controlled sediment influx to the sea and are thought to be reflected in the cycles.

KEYWORDS: Organic petrography, black shale, Devonian, cyclicity, depositional model

Alice C. O'Bryan

August 12, 2014

THE NATURE AND ORIGIN OF CYCLICITY IN THE CLEVELAND MEMBER OF THE OHIO SHALE (UPPER DEVONIAN), NORTHEASTERN KENTUCKY, U.S.A.

By

Alice C. O'Bryan

Dr. Frank R. Ettensohn

Director of Thesis

Dr. Edward W. Woolery

Director of Graduate Studies

August 12, 2014

ACKNOWLEDGMENTS

I would like to express my deep gratitude to Dr. Frank Ettensohn and the other members of my committee, Dr. Jim Hower and Dr. Cortland Eble. I have benefited enormously from the knowledge, guidance, and assistance provided throughout the completion of this thesis. Thank you for your contributions to my growth as a scientist and organic petrographer.

I would also like to extend my thanks to the staff of the Kentucky Geological Survey Well Sample and Core Library, Patrick Gooding, Ray Daniel, and Ryan Pinkston, for allowing me access to the core facility and allowing me to sample the D2 core.

Finally I would like to thank my parents and family for their unconditional love and support throughout my academic career and during the past three years in particular.

## TABLE OF CONTENTS

## LIST OF TABLES

## LIST OF FIGURES

# CHAPTER 1: INTRODUCTION

## 1.1. Background

Although there has been long-standing interest in black shales for their hydrocarbon and mineral content (e.g., Thiessen et al., 1925; Conant et al., 1961), black shales as oil and gas sources have become a popular topic of study since the 1970s during the first oil crisis. Once the crisis had passed, interest in these shales waned in favor of conventional hydrocarbon resources. However, as the world supply of petroleum has continued to decrease, interest in non-traditional hydrocarbon resources, in particular oil and gas shales, has grown. The two largest accumulations of oil-shale deposits are found in the United States; the largest is the Eocene Green River Formation in Colorado, Utah, and Wyoming and a close second are the Upper Devonian to Lower Mississippian oil and gas shales of Indiana, Kentucky, Ohio and Tennessee. The explored portions of these deposits are known to contain a mean of 7.5 million barrels ($1.19 \times 10^6$ $m^3$) of undiscovered oil (MMBO), which is about 14% of the total undiscovered oil in the Appalachian Basin Province (Milici et al., 2003). The Devonian siltstones and shales also contain a significant amount of continuous, or unconventional, gas resources; the current quantitative estimate is that these rocks contain a mean of 1293.6 billion cubic feet ($3.663 \times 10^{10}$ $m^3$) of undiscovered gas (BCFG) (Milici et al., 2003). Given this resource potential, there are ample reasons to enhance our understanding of the origins of these shales.

Kentucky is an excellent place to study Devonian black shales as they crop out in certain parts of the state. Additionally, Kentucky has an extensive collection of black-shale cores stored at the Well Sample and Core Library operated by the Kentucky Geological Survey. One of these cores, the D2 from Bath County was selected for study (Fig. 1.1). This core contains the full thickness of Cleveland Shale, the uppermost member of the Ohio Shale in Kentucky, and a well-known black-shale unit with significant hydrocarbon potential.

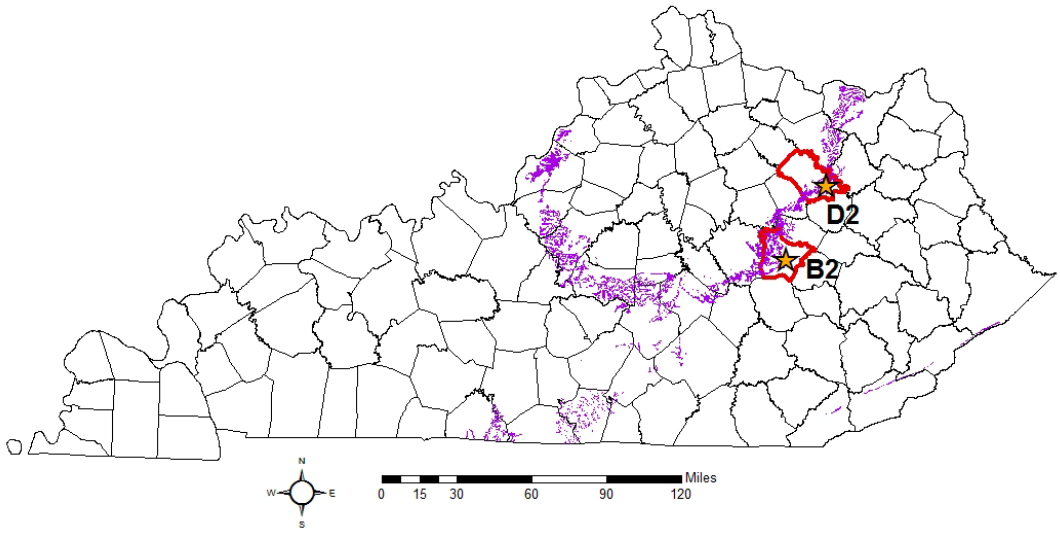


Figure 1. 1. Locations of D2 core (Bath County), as well as of the Devonian outcrop belt in Kentucky (purple).

## 1.2. Purpose

Despite the continued economic interest in these shales, their nature and origin are still incompletely understood. It is the intention of this study to further enhance this understanding. This study will focus on the Cleveland Member of the Ohio Shale, one of the most promising and economically significant stratigraphic intervals in North America (Ettensohn, 1995). A distinctive and widespread

characteristic of the Cleveland Member is the pattern of promontories and recessed intervals displayed on weathered outcrops (Fig. 1.2).


Figure 1. 2. "Ribbed" black shales from Cleveland Member of the Ohio Shale in Rowan County off of State Route 801 (Ettensohn et al., 2009a)

The promontories contain more organic matter than the recessed intervals, which makes them more massive and less prone to weathering (Ettensohn et al., 2009a). Although this weathering pattern has been well documented, the nature and origin of the cyclicity has yet to be determined. Considering the characteristic cyclicity, not only of these black shales, but of black shales in general, understanding

the origin of this cyclicity may be critical in understanding the origin of the shales themselves.

### 1.3. Stratigraphy

The Cleveland Shale is part of the larger black-shale sequence in Kentucky which includes up to ten units (Ettensohn et al., 1988) (Fig. 1.3A, 1.3B). The sequence is underlain by a basal unconformity, which places the Upper Devonian black shales overlying rocks ranging in age from Late Ordovician to the Middle Devonian (Ettensohn et al., 1988). The basal-most units of the black-shale sequence in central and west-central Kentucky are the Middle Devonian Portwood Member, commonly referred to as the Duffin or the Blocher Members of the New Albany Shale. The Portwood is largely a carbonate unit composed of organic-rich limestone or dolostone, dolomitic breccia, and dolomitic or calcareous gray to black shales; the top and bottom of this unit are defined by sandy lag horizons. This is the only "black-shale" unit that contains an in-place, benthic fossil assemblage. The Blocher is a massive, black, calcareous or dolomitic shale, with thin, dark dolostone and siltstone layers present locally. It is heavily bioturbated and contains benthic fossils, but breccias and gray shales like those in the Portwood are absent. Together, the Portwood and Blocher represent the least radioactive members of the Appalachian black-shale sequence; they can be observed on a gamma-ray curve as a series of negative deflections with prominent, rounded shoulders at the base of the unit. The Rhinestreet Shale Member of the West Falls Formation is a lower Upper Devonian black shale in eastern Kentucky (Fig. 1.3B), which has a homogenous, organic-rich microfacies. This unit produces one to three narrow, positive deviations on a

gamma-ray log (Fig. 1.3B). It is overlain by the upper Olentangy Shale, an Upper Devonian, greenish-gray, clay shale (Fig. 1.3B), which represents a time of yoking between the Appalachian Basin and the Illinois Basin (Ettensohn, 2008) (Fig. 1.4).

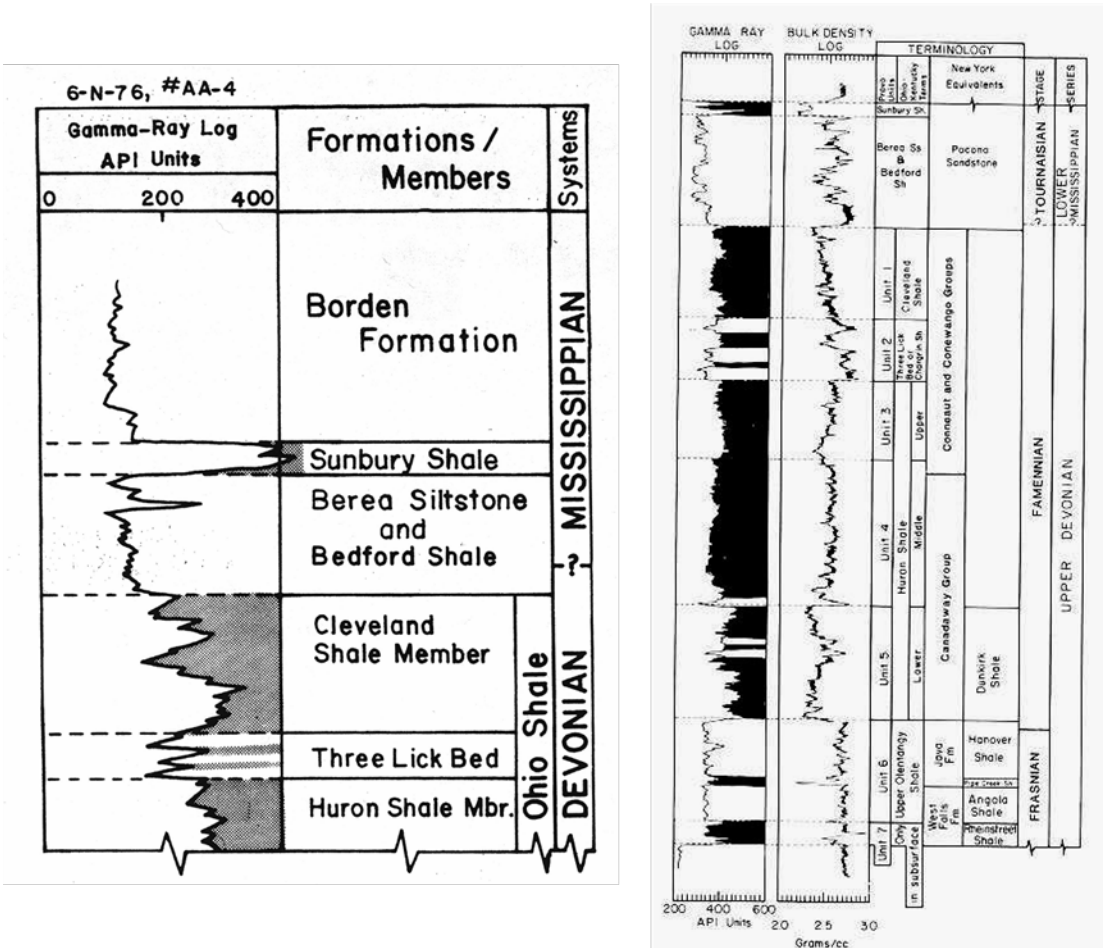


Figure 1. 3A. (left): Gamma-ray log for Ohio Shale through the Borden Formation. The Cleveland Shale's characteristic high-low-high pattern of deflections is clearly visible (Ettensohn et al., 2009b). B (right): Typical gamma-ray and bulk-density log signatures for Appalachian black-shale sequence (Ettensohn et al., 1988).

The shale in this unit is commonly bioturbated; dolomitic mudstones and calcareous lenses and concretions are locally present in the organic-deficient microfacies. In cores and at the outcrop scale, the upper Olentangy Shale can be

delimited by sandy lag horizons which occur at the base and top of the unit. On gamma-ray logs, the upper Olentangy can be identified by a series of uniformly negative deviations with right-angle shoulders at the top and bottom (Fig. 1.3B).

The units described above are generally not a part of the Ohio Shale in east-central Kentucky. In east-central Kentucky, where the study area is located, the Cleveland Shale is one of three units that comprise the Ohio Shale: in stratigraphically ascending order they are the Huron Shale Member, the Three Lick Bed, and the Cleveland Shale Member (Fig. 1.3A). The Ohio Shale is the Appalachian Basin equivalent of the New Albany Shale in the Illinois Basin across the Cincinnati Arch (Ettensohn et al., 1988). The Huron can be divided into three subunits based largely on gamma-ray signatures (Fig. 1.3A). The lower Huron is a very radioactive unit that displays a distinctive high-low-high pattern on gamma-ray logs, a response to laminated, organic-rich and organic-deficient microfacies. The middle Huron is the thickest part of the unit, and displays a uniform series of negative deviations caused by the increasing silt and clay content in the laminated, organic-rich microfacies. The *Protosalvinia* (*Foerstia*) biostratigraphic zone is a regional marker bed that is present in the Huron at, or just below, the contact of the middle and upper Huron. The upper Huron, consisting of laminated, organic-rich microfacies, is the thinnest part of the Huron. It is marked by moderately high, uniformly positive deviations, which distinguish it from the underlying middle Huron. The Three Lick Bed is a regional marker bed that can be correlated from outcrop to outcrop across central Ohio, north-central Tennessee, and into both the Appalachian Basin in eastern Kentucky and the Illinois Basin of west-central Kentucky (Figs. 1.3A, B, 1.4.).

The Three Lick Bed consists of three beds of gray shale separated by two beds of ribbed black shale (Fig. 1.3A), and appears on gamma-ray logs as three closely spaced negative deviations separated by two positives ones (Fig. 1.3A, B). The Cleveland Shale, the unit studied here, is the uppermost member of the Ohio Shale. Like the lower Huron, this unit has a high-low-high pattern of deflections on gamma-ray logs (Fig 1.3A, B), but unlike the Huron, this unit is composed almost entirely of laminated organic-rich microfacies. The Cleveland has a very high

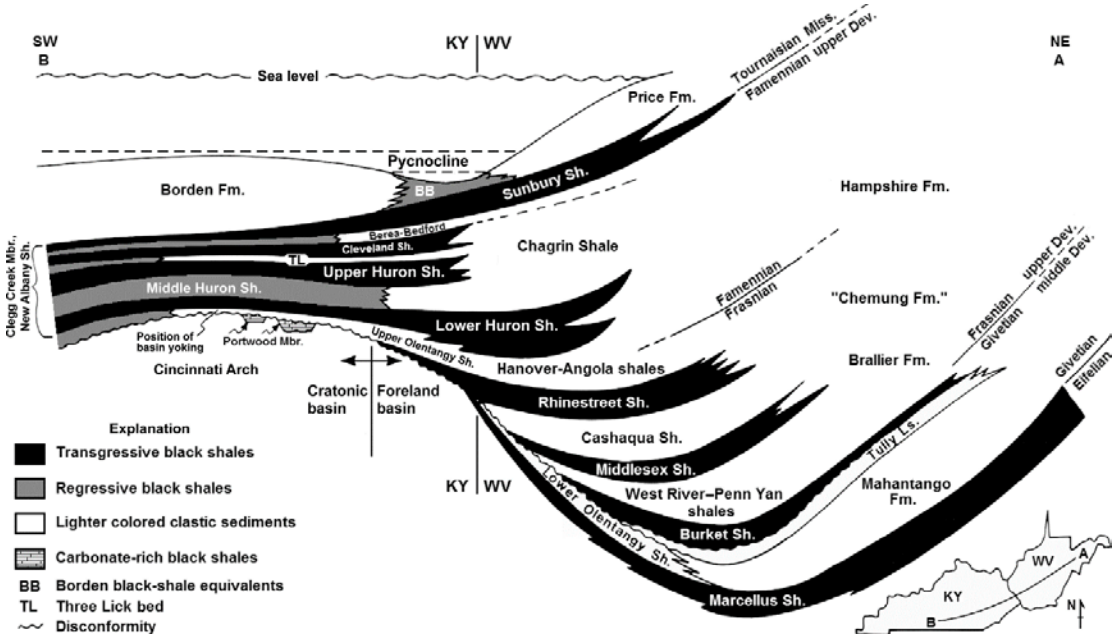


Figure 1. 4. A schematic northeast–southwest section (AB) through the central Appalachian Basin in West Virginia and Kentucky, showing entire Appalachian black-shale sequence in relation to the shape of the basin and time (Ettensohn and Lierman, 2012).

organic-carbon content, high concentrations of heavy elements, and phosphate concretions, all of which are associated with the increased radioactivity of the unit (Ettensohn et al., 1988).

The Bedford-Berea Sequence is an Upper Devonian clastic sequence and, as such, is the least radioactive unit in the Appalachian black-shale sequence (Fig. 1.3A, B). It is composed of gray silty shales, black shales, and minor sandstones that intertongue complexly. The Sunbury Shale is the youngest unit in the black-shale sequence, and is generally the most radioactive unit with a narrow, sharp, high-low-high pattern of very positive deflections on gamma-ray logs (Fig. 1.3A, B). Like the Cleveland, it has high concentrations of organic carbon, abundant phosphorite nodules, and high concentrations of heavy metals. It is composed of homogenous, organic-rich microfacies (Ettensohn et al., 1988).

### 1.4. Tectonic, paleogeographic, and paleoclimatic setting

The breakup of Rodinia in late Neoproterozic time generated several smaller continents including Gondwana and Laurentia, the latter representing the ancestral North American continent. After western Europe (Baltica) collided with Laurentia in Silurian time, the continent was called Laurussia. The modern Appalachian area underwent several marked climatic changes as Laurentia/Laurussia drifted across different latitudes. From Late Precambrian through Early Cambrian time, it had a humid to sub-humid climate and was located between latitudes 40–60° south. In Middle Cambrian to Late Mississippian time, when the Cleveland was deposited, Laurentia resided between latitudes 15–35° south and had an arid, subtropical climate (Ettensohn, 2008) (Fig. 1.5.), although local climate within the basin may have been cold and humid, with relatively low mean annual temperatures (Elrick et al., 2009). The Late Mississippian to Late Permian Laurussian climate was humid to perhumid, and tropical due to the continent's location between +/-5° of the equator.

From the Late Permian time onward, Laurussia was in the northern tropical belt between the paleoequator and 5° north (Ettensohn, 2008).

The modern Appalachian Basin is a multistage, composite, retro-arc foreland basin. It was the product of tectonic loading during the four nearly continuous orogenies on the eastern margin of Laurentia/Laurussia during the assembly of Pangaea: the Taconian, Salinic, Acadian/Neoacadian, and Alleghanian. Of these, the Acadian/Neoacadian was largely responsible for the Appalachian black-shale sequence (Ettensohn, 2008). The Acadian/Neoacadian orogeny itself can be divided

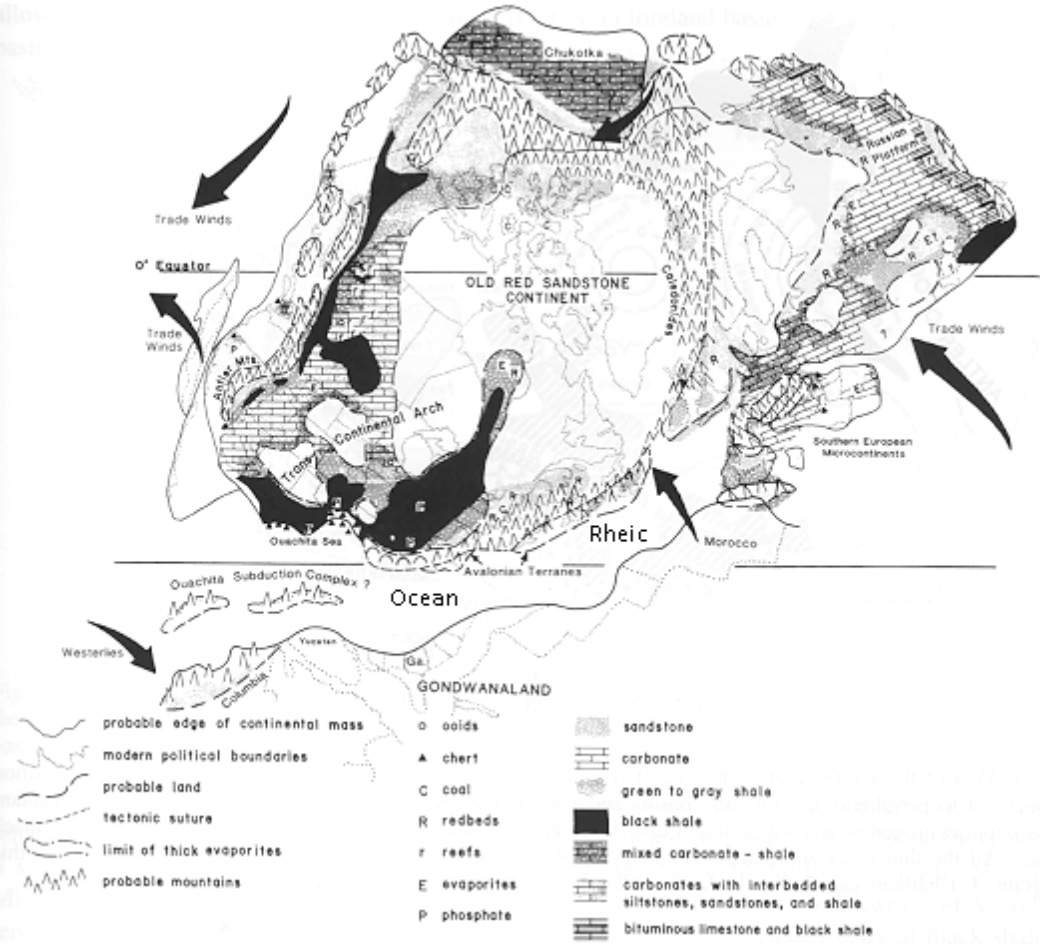


Figure 1. 5. Paleogeographic reconstruction of Laurussia during Late Devonian time. Location of study area is noted (Ettensohn et al., 1988).

into four tectophase cycles, each giving rise to an unconformity-bound sedimentary sequence (Ettensohn, 1985). The first tectophase saw the microcontinent Avalonia docking at the St. Lawrence Promontory and the subsequent infilling of a basin in New England and the Canadian Maritime provinces (Ettensohn, 2008). Tectophases two and three overlapped significantly with the docking of the Carolina Terrane at the New York promontory, and deformation continued to migrate southward with the impending collision of the Carolina Terrane and the Virginia Promontory. This series of events produced the Catskill Delta complex and was responsible for the

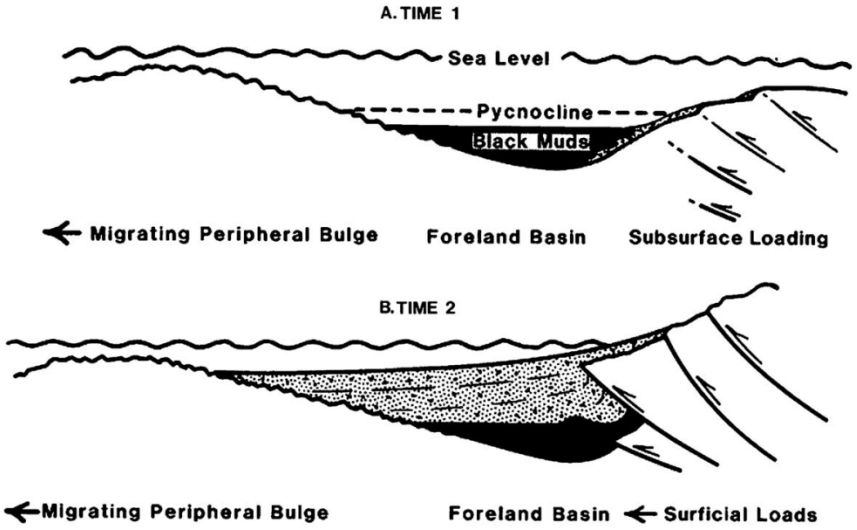


Figure 1. 6. Schematic diagrams showing relationships between foreland-basin generation, sediment infill, and deformational loading (Ettensohn, 2008).

deposition of the Marcellus Shale and other related black shales in the Appalachian foreland basin. The fourth, and final, tectophase involved Neoacadian dextral sheer and accretion of the Carolina terrane at the Virginia promontory and the accretion of the Dahlonega terrane and Hillabee back-arc volcanics at the Alabama

Promontory. An important formation deposited during the fourth tectophase is the Sunbury Shale, which is the darkest, most organic-rich, and most radioactive of all the shales in the Appalachian black-shale sequence (Ettensohn and Lierman, 2012). The sediments that accumulate as a tectophase proceeds typically reflect the same general stratigraphic sequence (Ettensohn, 2008; Ettensohn and Lierman, 2012) (Fig. 1.7). As deformational loading in the orogeny proceeds a foreland basin develops just cratonward of the load, and on the distal margin of the basin, as subtle bulge is generated and moves cratonward such that bulge uplift generates a regional unconformity on and near the bulge (Fig. 1.6A). This period of erosion and non-deposition is typically followed by the deposition of shallow-water, transgressive sediments, related to rapid subsidence of the foreland basin. Since most of the aforementioned deformational loading occurs in the subsurface, there is often no external sediment source, and decaying organic matter in the water column becomes the major sediment (Fig. 1.6A). As the basin continues to subside and deepen, the waters become suboxic to anoxic, allowing for organic matter to be buried and preserved, eventually forming black, organic-rich shales (Fig. 1.7). The deposition of dark shales continues as long as deformational loading occurs, but once enough relief and sufficient drainage nets have been generated in the deformational load to form a major sediment source, coarse, immature debris is transported into the basin, generating flysche-like sedimentation (Figs. 1.6B, 1.7). While the basin is infilled with sediment, the surface load continues to be eroded. As the basin fills and the subaerial load erodes, a thin interval of either carbonates or mixed carbonates and shale is deposited in the resulting shallow sea (Fig. 1.7). As

the orogen continues to erode, and the surface load is largely removed, isostatic rebound leads to the formation of a broad peripheral sag that migrates towards the rebounding area over time (Ettensohn, 1995). The sediments that accumulate in this low area typically reflect a transgressive sequence of open-marine shales or shales and carbonates. The final phase of the typical foreland-basin sedimentary cycle is deposition of fine-grained siliciclastic sediments as the clastic wedge progrades cratonward. These sediments are often described as "post-orogenic," "molasse-like," or "deltaic," and generally consist of siltstone, silty-shale, shale, mudstone, redbeds, or shaly carbonate facies (Ettensohn, 1995, 2004, 2008) (Fig. 1.7). Of course, in this study, it is the early phase of organic-rich, black-shale deposition that is being critically examined.

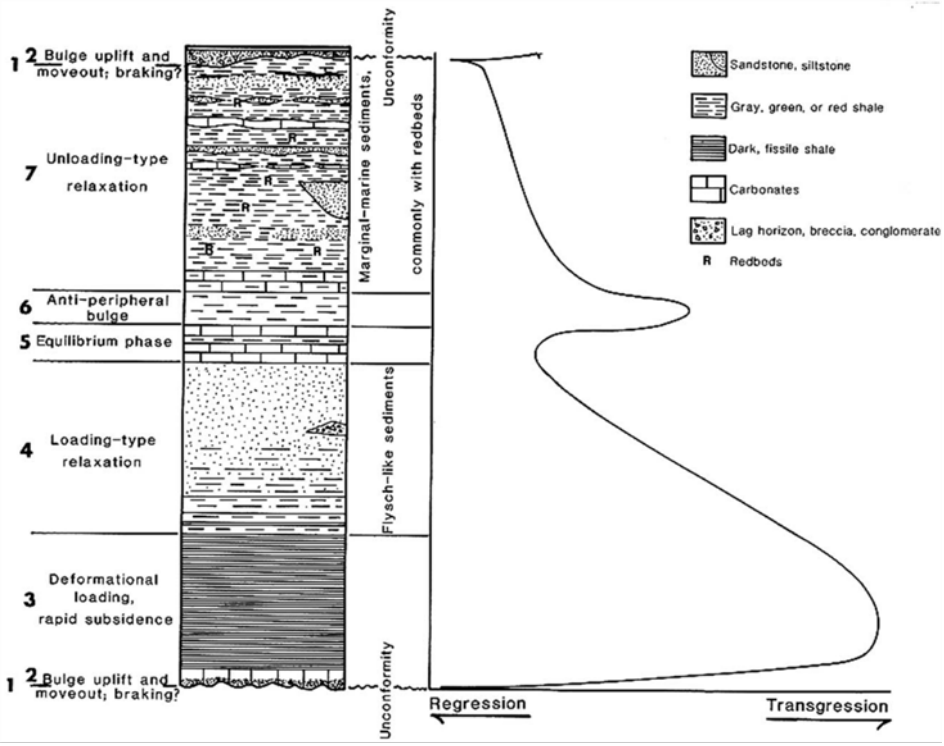


Figure 1. 7. Parts of an ideal tectophase cycle for subduction-type orogenies (Ettensohn and Lierman, 2012).

Late Devonian time has often been characterized as a greenhouse world, but this interpretation is now being questioned. Glacial deposits in South America (Elrick et al., 2009) and in the Appalachian Basin Province (Brezinski et al., 2008, 2009, 2010; Ettensohn, 2008) provide clear evidence that glaciation was present at this time, but the full extent of glacial cover is still unclear. The South American glacial deposits have been known for some time (Caputo, 1985), but were interpreted as being deposited only at latitudes greater than 70° (Frakes et al., 1992).

Probable glacial deposits from the Appalachian Basin, equivalent to the Cleveland Shale, are known from the Spechty Kopf and Rockwell formations, a diamictite-mudstone-sandstone sequence (Fig. 1.8A) in the central Appalachian Basin, long viewed to represent subaqueous debris flows (Bjerstedt and Kammer, 1988; Sevon, 1969, 1979) or tsunami deposits (Sevon et al., 1997). New work has reinterpreted these deposits to represent a sequence of glacial deposits (Brezinski et al., 2010). More than 500-km away, in the Upper Devonian Cleveland black shales of northeastern Kentucky, an in-situ dropstone (Fig. 1.8B) has been described, and related, via stratigraphy and biostratigraphy, to the central Appalachian diamictites (Ettensohn et al., 2009a).

Boulders of this type have been known in Kentucky for some time (Ettensohn et al., 2008). However, none had previously been found in-situ, and they had previously been interpreted to be the result of Pleistocene glaciation. The age and lithology of the in-situ boulder indicate an Appalachian or Laurentian origin, and the shape of the boulder, with flattened sides with rounded edges and corners (Fig.

1.8B), indicates that it is most likely a glacial erratic (Ettensohn et al., 2008). Knowing that the boulder has a glacial origin, however, does not explain its presence in the black shale; the only mechanism through which this quandary can


Figure 1. 8. A. Example of a diamictite from the central Appalachian Basin (Sideling Hill, MD). B. In-situ Robinson boulder (Ettensohn et al., 2009a).

be explained is ice-rafting (Ettensohn et al., 2008). Previous models require glacial ice to have been transported at least about 200km across an alluvial plain from the Acadian highlands to the epicontinental sea in the Appalachian Basin (Fig. 1.9). It is

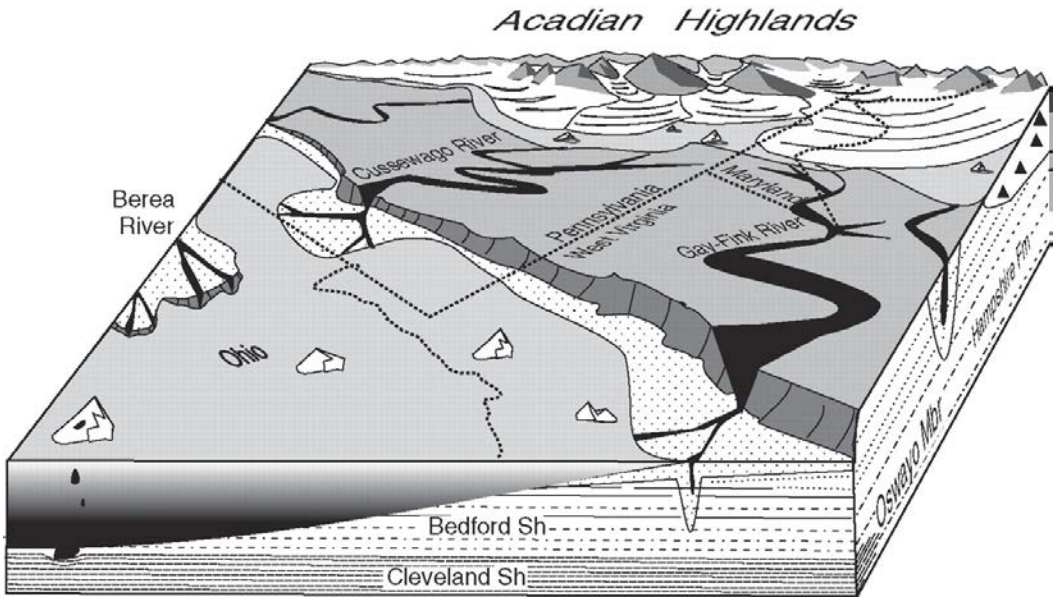


Figure 1. 9. Block diagram of interpreted depositional scenario giving oblique perspective of the central Appalachian Basin during the latest Devonian (Brezinski et al., 2009).

more likely that glacial tongues extended across the alluvial plain separating the highlands from the sea, and that calving icebergs launched boulder-bearing icebergs into the sea (Ettensohn et al., 2008). Ultimately, the conclusion to be drawn from this work is that Late Devonian cooling was more severe and had more extreme global effects than previously thought, or it is possible that the Neoacadian mountains (thrust sheets on Fig. 1.10) were high enough to support alpine glaciers that moved westwardly toward the Black Shale (Cleveland) Sea (Figs. 1.6, 1.10).

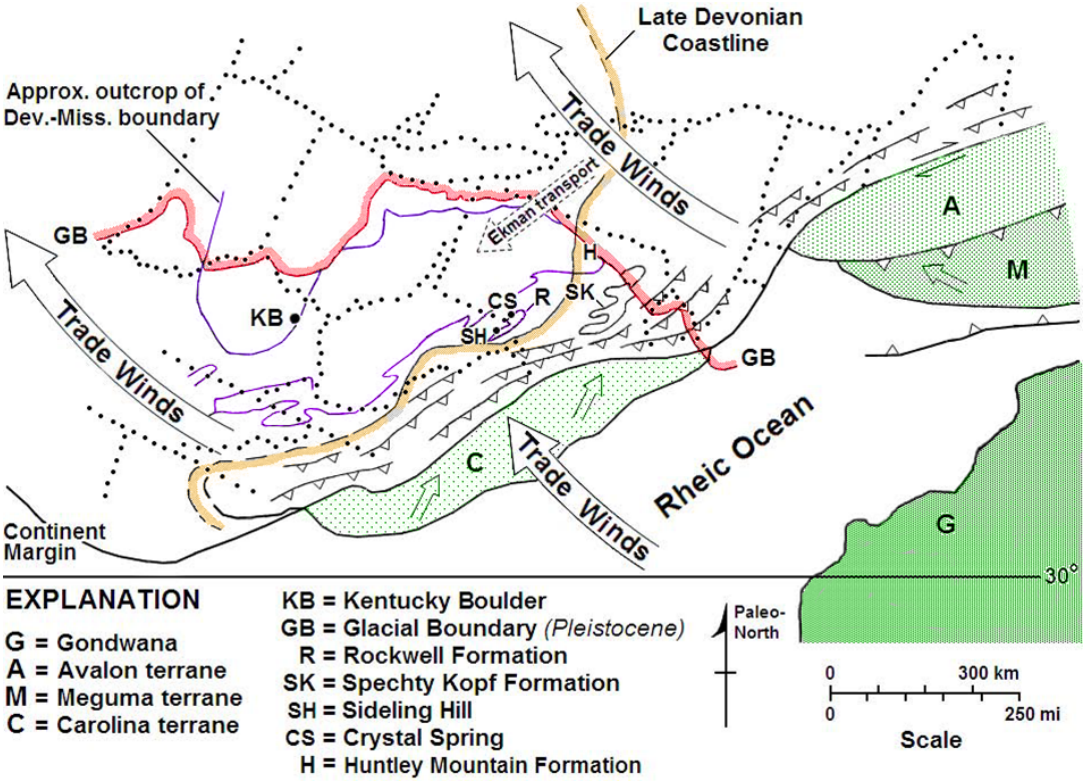


Figure 1. 10. Late Devonian paleogeographic reconstruction of southeastern Laurussia showing location of probable Kentucky dropstone relative to likely Late Devonian wind and current directions (Ettensohn et al., 2008).

## CHAPTER 2: PREVIOUS WORK

Jaminski et al. (1998) undertook the task of characterizing the fine-scale compositional variations within the Cleveland Shale in order to create a depositional model for controls on the accumulation of sedimentary organic matter at lamina to basin-wide scales. The Cleveland was selected for study because of the characteristic ribbed pattern the unit displays in outcrop (Fig. 1.2.); this ribbing reflects decimeter-scale compositional variation. Characterization of the laminated organic-rich sediments that comprise this unit allowed for the evaluation of the "instantaneous" environmental conditions during the time of deposition, which are recorded in individual laminae. Ultimately, it was proposed that the cyclicity observed in the Cleveland had a climatic origin, and a model was developed wherein weakly coupled freshwater and terrigenous clastic fluxes, both climate-sensitive parameters, were the controlling factors for cyclicity (Jaminski et al., 1998). These authors based their conclusions on organic petrography, carbon-sulfur elemental analysis, major- and trace-element analysis, and degree of pyritization. Their model, which included slow accumulation of organic matter, provides time for extensive bacterial reworking of organic matter. Such reworking would account for the high total-carbon content of the Cleveland Shale, as well as for the large amounts of degraded, amorphous organic matter. The authors suggested that increasing freshwater fluvial discharge into the basin, coupled with increasing clastic sediment flux, would have depressed and strengthened the pycnocline (Jaminski et al., 1998). This, in turn, would have reduced upward mixing of bottom waters, lowered the surface productivity and decreased the deposition rate of organic-rich sediments.

The inverse would have occured following a decrease in freshwater fluvial discharge into the basin (Jaminski et al., 1998).

A second important consideration is the control on the accumulation of organic matter within the black shales. It has been proposed that the "master variable," when discussing organic-matter accumulation, is relative sea-level change, with the rise and fall of the world's oceans controlling clastic dilution, biological productivity, and preservation of organic matter (Sageman et al., 2003). A rise in the local sea level can lead to sediment starvation and the concentration of organic matter, as well as less seasonal and more episodic mixing of bottom waters. The decreased regularity of the mixing would have provided a longer build-up interval for remineralized nutrients, so that when episodic mixing occurred, it was followed by a period of enhanced organic production due to nutrients having been released in the enriched bottom waters. Correspondingly, a fall in the local sea level would have initiated increased sediment delivery and enhanced water-column mixing in the basin. Such increased sediment delivery to the basin would have diluted the sea-surface, organic matter, allowing respiratory demand to be met by the increased oxygen supply and preventing the accumulation of organic-enriched strata (Sageman et al., 2003).

The presence of icebergs in the Devonian epicontinental sea would have also had impacts on the chemical and biologic activity in iceberg-prone areas. Recent work indicates that icebergs are hotspots of enhanced organic productivity and carbon sequestration (Smith et al., 2007). These hotspots, as well as changes in sea level and climate, would have left distinct signatures in the stratigraphic record. For

example, the absence of glaciation would have very likely generated unique chemical signatures when compared to the presence of glaciation. In fact, stable-isotope geochemistry has been a particularly useful proxy for determining changes in seawater temperature, regression, and glaciation (Brezinski et al., 2010). There have been numerous studies of the stable-isotope composition of Devonian strata in the Appalachian Basin, and of the greater continental US, as well as throughout the world. In particular, oxygen isotopes from conodont-apatite, collected from Early-Middle Devonian rocks in the Western US (Nevada) and the Czech Republic (Prague Basin), show large, rapid isotopic shifts that are best explained by growth and melting of continental ice sheets (Elrick et al., 2009; Elrick and Scott, 2010). This same trend was documented by Joachimski et al. (2009) in a series of conodont-apatite samples from Europe, North America, and Australia, where a complete paleotemperature record for the latest Silurian through Devonian time was developed. After the period of cooling in Middle Devonian time (the minimum temperature was approximately 22°C), average sea-surface temperatures rose throughout the Frasnian and Early Famennian time to an average of 30-32°C. At this point, a short-term cooling trend, marked by the increase of $\delta^{18}O$ in conodont apatite, very likely records to glaciation in Latest Devonian time (Joachimski et al., 2009).

The interval of black shales between the Huron Shale Member of the Ohio Shale and the Sunbury Shale (Figs. 1.3A, B) has been geochemically and petrographically examined by previous workers to determine the chemistry of the kerogen and to aid in correlative efforts. Variations in organic-matter source and

associated environmental conditions are reflected in the petrographic composition of the shale (Rimmer et al., 2004). Previous work has established that the overall percentage of organic matter increases up-section. This increase is mostly related to the bituminite composition, as the proportion of vitrinite and inertinite remains relatively constant throughout (Robl et al., 1987). The bituminite and alginite concentrations, on the other hand, have a variable, and generally inverse, relationship. In fact, the constancy of the vitrinite and inertinite content indicates that there was a fairly uniform source of terrigenous material throughout the period of deposition. The vitrinite was probably sourced from Devonian forests in the northeastern United States and transported to the Appalachian basin by rivers along the coast. The fusinite is most likely oxidized plant debris that was transported to the basin as charcoal (Robl et al., 1987). Alternatively, some of the fusinite may represent oxidized marine kerogen (Rimmer et al., 2004).

## CHAPTER 3: METHODS

Since the 1970's and the Arab oil embargo, there has been an ongoing interest in these Devonian-Mississippian black shales, initially as oil shales, and for the last six years, as gas shales. In the 1970's these shales were extensively cored along the circumference of the Jessamine Dome (Fig. 1.1) in order to characterize them for oil and gas reserves. The core examined in this study, D2, was part of this Eastern Gas Shales Project (EGSP).


Figure 3. 1. Example of the D2 core laid out in storage box.

## 3.1. Lithologic Characterization and Gamma-Ray Stratigraphy

### *3.1.1. Lithologic Characterization*

The D2 core, which contains the entire thickness of the Cleveland Shale, was examined and described from the Three Lick Bed to the Bedford/Berea (Fig. 1.3A, B). The lithologic characterization of the core included the division of the Cleveland into discrete cycles of lighter-gray and darker-gray shales (Fig. 3.1.). The subdivision into cycles was based on the degree of fissility, color, and wettability.

### *3.1.2 Gamma-Ray Stratigraphy*

Gamma-ray curves and radioactivity profiles are useful for lithologic discrimination of siliciclastic rocks (Rider, 1986), and in areas such as the Appalachian Basin, where the thick shale deposits have a generally homogenous appearance, gamma-ray stratigraphy is the basis upon which formation boundaries are determined (Ettensohn et al., 1979; Ettensohn et al., 1988). U.S. Department of Energy studies in the 1970s (such as Ettensohn et al., 1988) established a link between color, amount of organic material and the intensity of gamma radiation, showing that dark-grey to black shales could be distinguished from light-grey to green shales based on gamma-ray signatures. The dark-grey to black shales generally contain more organic matter than the lighter shales, and consequently, have more intense gamma-ray signatures. This increase in radioactivity is closely tied to the clay mineralogy of the unit and to the amount of included organic matter. Clay minerals, which contain abundant K and $^{40}K$, as well as U and Th, are easily adsorbed onto the clay lattice (Fertl, 1982). In addition, radiation in the dark shales

is generated by U, closely associated with the abundant organic matter (Conant and Swanson, 1961), which can trap additional U through the reduction of U from seawater (Durrance, 1986). The radiation in green shales is mostly generated by $^{40}K$ incorporated into clay minerals (W.H. Blackburn, oral communication, 1978, *in* Ettensohn et al., 1979). Additional sources of radioactivity include U and Th adsorbed onto clay lattices (Fertl, 1982). Siltstones and sandstones are significantly less radioactive than the shales, because as grain size increases, the clay content generally decreases, which leads to decreased radioactivity (Rider, 1986).

For this study a synthetic gamma-ray curve was generated with a hand-held scintillometer. These synthetic curves are not exactly the same as gamma-ray curves, as they comprise of a series of closely spaced, connected points in which radioactivity is measured in counts per second, in contrast to gamma-ray curves which are continuous and measured in API units, a standardized unit established by the American Petroleum Institute in 1959 based on the use of a permanent calibration facility (Ettensohn et al., 1979). However, the two curves are similar enough that they can be quantitatively correlated (Ettensohn et al., 1979). Such synthetic curves are generated by laying the core out on a flat surface and measuring the radioactivity in counts per second using a hand-held scintillometer. Scintillometer measurements were taken at approximately the middle of each designated cycle; if the designated cycle exceeded 10 cm in length, multiple scintillometer measurements were taken. The radioactivity measurements were then plotted against depth below surface. Lithologic descriptions and scintillometer

measurements were carried out at the Kentucky Geologic Survey Well Sample and Core Library.

### 3.2. Organic Petrography

Two standard methods exist for conducting microscopic studies of organic matter in shale: reflected-light petrography and transmitted-light with kerogen concentrates. This study utilized reflected-light petrography, because the benefits of reflected-light petrography include: 1) the ability observe organic matter in original context with orientation preserved, 2) the ability to distinguish autochthonous and reworked vitrinite and inertinite, and 3) the ability to distinguish between different types of liptinitic particles. Using transmitted-light and kerogen concentrates can also be useful because it makes the identification of palynomorphs easier. A variety of plants have been identified from Devonian strata, indicating that the typical Devonian plant community included progynmosperm trees, such as *Archaeopteris*, lycopsids, early vascular plants and ferns, such as *Rhacophyton* (Berry and Fairon-Demaret, 2001; Hawkins, 2006); however, sorting prior to deposition, especially in marine environments, may have taphonomically eliminated all but the most resistant plant material (Berry and Fairon-Demaret, 2001). Therefore, attempting to identify palynomorphs would not have been a useful addition to this study. Also, the use of kerogen concentrates and transmitted light means that all the liptinitic particles, plus bituminite, are classified as amorphous organic matter, because it becomes impossible to distinguish the different types of liptinitic particles (Teichmüller, 1986).

The petrographic identification of organic matter in shale is based on the principles of organic petrography established through the study of coal. The International Committee for Coal and Organic Petrography (ICCP) has published several papers that describe the standard methods for identification of vitrinite, huminite, and inertinite; official guidelines for the microscopic identification of liptinite have not yet been published. However, the principles of coal petrography cannot be directly applied to shale petrography, as modifications must be made for the nature of the material being studied. Some of these organic-shale-specific modifications are detailed in Hutton (1987) and Hutton et al. (1994).

Organic particles are classified into maceral groups based on reflectance, morphology, relief, and fluorescence. These particles are commonly grouped into four large categories: inertinite, vitrinite, liptinite, and mineral material (Fig. 3.2.), each of which can be subdivided further. For example, inertinite, which consists of preserved charcoal, includes the subgroups fusinite, semifusinite, and inertodetrinite. Vitrinite, which consists of preserved woody material, includes the subgroups vitrinite and vitrodetrinite. Liptinite, derived from soft-bodied and lipid-rich materials, consists of alginite (telalginite and lamalginite), sporinite, bituminite, and liptodetrinite. The macerals of the liptinite group can have either a terrestrial or marine source; alginite and bituminite represent marine, algal material, whereas sporinite represents preserved, terrestrial spores. It can be difficult to assign either a terrestrial or marine source to liptodetrinite particles as, by definition, they cannot be assigned to any of the other liptinite groups (ICCP, 1976). Inertinite and vitrinite are both primarily derived from terrestrial plant material; they can be distinguished

based on reflectance and color. Inertinite is more highly reflective than vitrinite and tends to be white to very-light grey; inertinite is also more likely to exhibit complete cell lumens, though some cell structure may occasionally be visible in vitrinite. Liptinites are the primary fluorescing macerals and are best identified under blue-light excitation. It is worth noting, however, that, depending on thermal maturity, vitrinite may also exhibit fluorescent properties (Teichmuller and Durand, 1983;

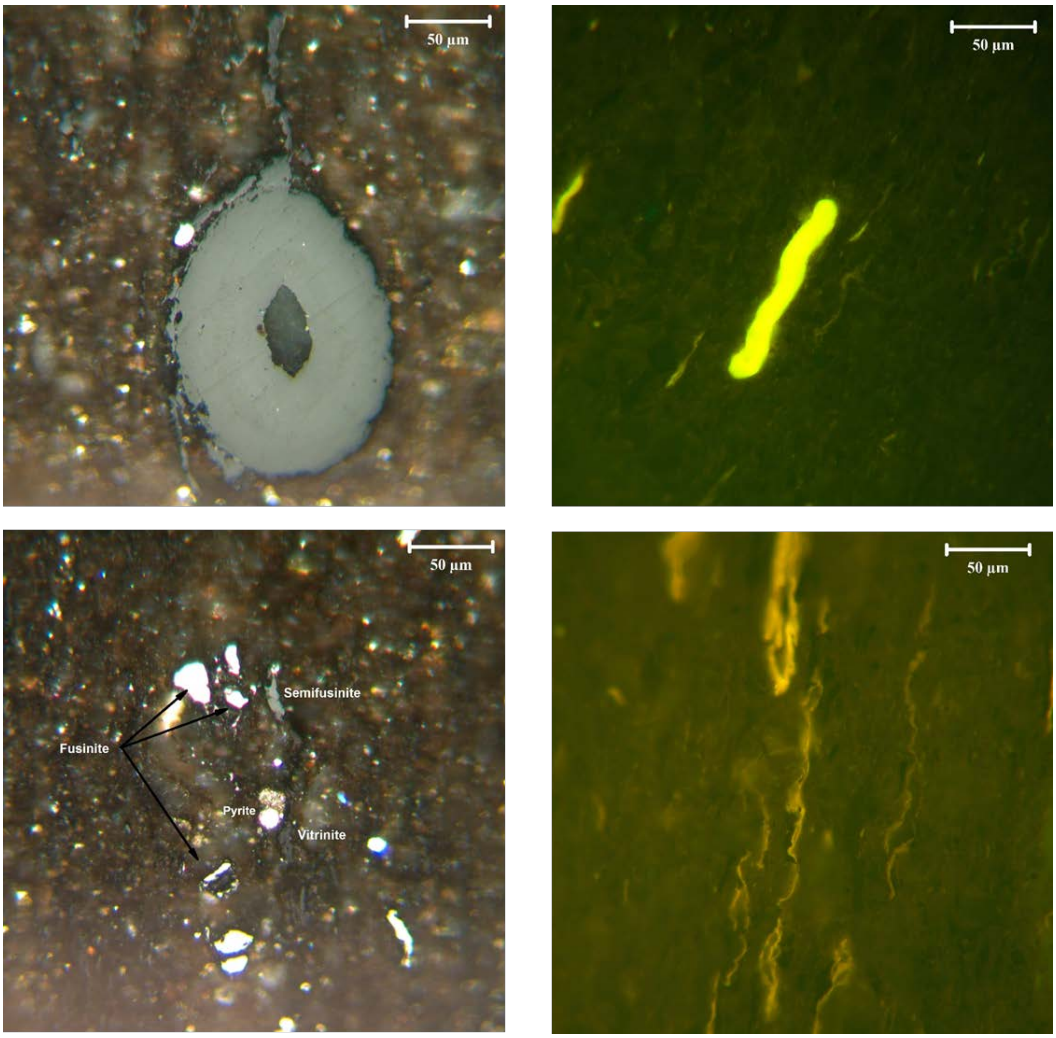


Figure 3. 2. Upper right: Vitrinite; upper left: single telalginite; lower left: fusinite, semifusinite, vitrinite, and pyrite; lower right: lamalginite.

ICCP, 1998). Depending on the maturity of the sample, liptinite particles can fluoresce a variety of colors, ranging from yellow-green to red-brown, and at very high maturities, fluorescence may disappear completely. Loss of florescence, however, is generally not an issue in oil and gas shales, as the maturity is typically low enough that the liptinitic material maintains its fluorescent properties. Moreover, the different types of liptinite are distinguished based on the intensity of the fluorescence and morphology. Telalginite has a strong yellow-green fluorescence and can appear as spherical particles or flattened, elongate disks, and commonly the internal structure of the algal precursor is visible. In addition, the boundaries of telalginite particles are smooth and unadorned. Lamalginite also fluoresces yellow-green but tends to fluoresce at a weaker intensity relative to telalginite; lamalginite particles also tend to be thinner, more elongate, and have a less regular appearance than telalginite. In contrast, the sporinite observed in these samples has flattened, ellipsoid shapes and fluoresces red-brown.

Bituminite is a type of amorphous organic matter which often comprises a significant portion of the organic matter in oil and gas shales (Stasiuk and Goodarzi, 1988). Definitions of bituminite differ between labs and a variety of terms, including amorphinite, sapropelic groundmass, sapropelinite I and II and humosapropelinite, and heba- and fluoramorphonite (Stasiuk and Goodarzi, 1988) have been used to describe bituminite. Attempts to standardize the identification of bituminite have been made (e.g., *Stach's Textbook of Coal Petrology* [Stach et al., 1982], "Petrographic classification of oil shales" [Hutton, 1987], and *Organic Petrology: a new handbook incorporating some revised parts of Stach's Textbook of*

*Coal Petrology* [Taylor et al., 1998]), however, the ICCP has not updated the official guidelines for bituminite identification and classification since the publication of the *International Handbook of Coal Petrology* (2nd ed.) in 1976.

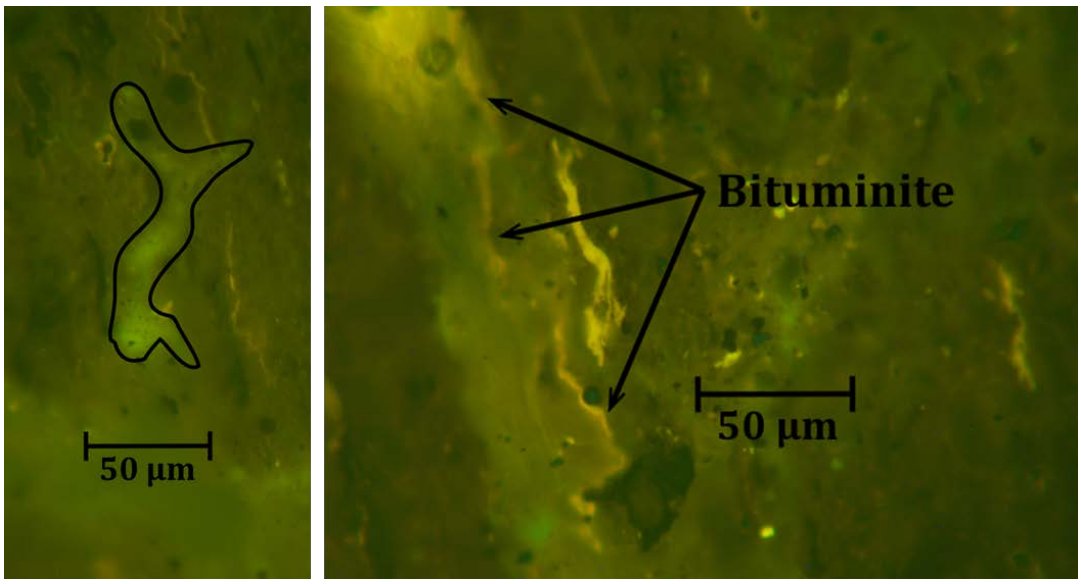


Figure 3. 3. Examples of bituminite observed in the D2 core. Left: Bituminite with amorphous appearance and diffuse margins. Right: Bituminite occurring as Schlieren strands with an amorphous appearance and no visible internal structure.

The definition of bituminite utilized in this study largely follows the definition of Teichmüller (1974) and Teichmüller and Ottenjann (1977) who first established criteria for the identification of bituminite. In accordance with this definition bituminite may display a relatively weak, pale green-yellow or dull orange-brown fluorescence under blue-light excitation and can occur in several different forms. It can have a fine, granular appearance where the granules have diffuse, smudgy margins, it may have a diffusive, amorphous appearance with no recognizable internal structure, or it may occur as fine streaks or lenses (Araujo et

al., 2010) (Fig. 3.3). Bituminite can also be incorporated into the matrix material as a "fine, delicate mesh," this form of bituminite can cause the mineral matrix to display a weak fluorescence (Teichmüller, 1986).

Macerals with the -detrinite suffix are identified by their small size. The official ICCP guidelines for the identification of inertinite state that particles which are less than 10 μm in the maximum dimension for compact grains (e.g., equant or spherical), less than 10 μm in the minimum dimension, and 2 μm in the maximum dimension for elongate or thread shaped grains, are classified as inertodetrinite. The official guidelines for huminite and vitrinite specify the same dimensions, with the addition that all fragments that cannot be grouped with certainty are to be called detrovitrinite, even if they are greater than 10 μm. Because no official guidelines for liptinite macerals have been published, the same dimensional guidelines have been applied to the identification of liptodetrinite for the purposes of this study.

Using the above guidelines, a four-foot section from the lower Cleveland Member of the D2 core from 89–93 ft was prepared for organic petrology. Preparation was accomplished by dividing the core into approximately 1-in sections, preserving the original orientation, and preparing them as 1.5- inch polished pellets with epoxy resin according to standard procedures (Pontolillo and Stanton, 1994) at the University of Kentucky Center for Applied Energy Research (CAER). The prepared pellets were examined by oil immersion on a Leitz petrographic microscope under plane-polarized, reflected, white light and blue-light excitation. Combined white-light and blue-light point-count analysis to 500 points, or to an end point above 500 at the end of a transect, was conducted on each pellet.

Petrographic composition was determined based on the concentration of macerals (total inertinite, total vitrinite, and total liptinite) and mineral matter. The organic macerals were classified using the ICCP System 1994 nomenclature (ICCP, 1998, 2001) with organic-shale-specific modifications based on Hutton (1987) and Hutton et al. (1994), as well as those previously described.

### 3.3. X-ray Fluorescence and Total Organic Carbon

A limited number of x-ray fluorescence measurements to determine major-element oxides and trace-element concentrations were taken using a TYCO portable XRF gun on loan to the KGS from CIMAREX. Twenty-three total measurements were taken between 94.5 and 86.1 ft (depth in core); the average spacing was 0.3 ft (0.09 m). This provided readings for the following elements in ppm: Cr, Si, Al, P, Ti, U, Cu, Th, Ni, Co, Ag, Pd, Nb, Zn, Mn, Mo, Zr, Sr, Rb, Pb, Se, Fe, K, S, Sh, W, Re, Bi, Hg, Au, V, Sc, As, Ca, Ta, Sb, Cd, Hf, Cl, and Mg. The measurements taken with the portable XRF gun are internally consistent and can be used to generate cycle curves.

Ti, K, and Si are elements that have been used as proxies for clastic influx when normalized against Al. Ti/Al can be used as a proxy for coarse clastic influx because Ti occurs in clay, sand, and silt-sized particles, whereas Al only occurs in clay minerals. Ti concentration has also been used as an indicator of paleo-wind strength (Boyle, 1983; Shimmield, 1992; Bertrand et al., 1996). K/Al represents the fraction of clastic input, and changes in the K/Al ratio indicate that there were changes in clay mineralogy. For example, increasing K/Al is suggestive of micaceous clay or possibly fine-grained K-feldspar (Rimmer, 2004). Si occurs in all grain sizes, but a significant increase in Si/Al can indicate an increase in quartz silt and sand.

Both Al-normalized and trace-element ratios can be used as paleo-redox proxies (Rimmer, 2004). For this study Mo/Al, V/(V+Ni), and V/Cr were used.

Total organic carbon was determined by measuring total carbon with a Leco SC-432 carbon/sulfur analyzer, and then subtracting out inorganic carbon through standard coulometric techniques (Huffman, 1977). These measurements were carried out at KGS facilities at the University of Kentucky.

# CHAPTER FOUR: RESULTS

The D2 core was collected in 1980 in Bath County, Kentucky, in the Olympia quadrangle as part of the Eastern Gas Shales Project and has been stored at either the CAER or the KGS Core Library since then. The bottom of the Cleveland Shale was identified in the core by its contact with the Three Lick Bed; the top was identified by its contact with the overlying Berea-Bedford Formation. The core was chosen because it was deemed to be "average" in thickness and character for the black-shale sequence in the eastern Kentucky outcrop belt.

## 4.1. Lithologic Characterization

In the studied core segment of the lower Cleveland Shale, lithologic characterization revealed 56 complete cycles and one incomplete cycle over 48 ft (14.63 m), which gives an average cycle thickness of 0.85 ft (0.26 m). The minimum cycle thickness was 0.20 ft (0.06 m)(cycles 39 and 38) and the maximum cycle thickness was 3.25 ft (0.99 m) (cycle 42). Cycle 33 marks the location of the middle of the studied core segment with approximately 24 ft (7.32 m) of core above and below this point. The cycles become thicker toward the top of the unit in the core. The first 33 cycles have an average thickness of 0.77 ft (0.23 m), whereas the second 23 cycles (34 through 56) are 0.98-ft (0.30-m) thick on average, about 1.3-times thicker than the cycles in the lower section of the core (Fig. 4.1).

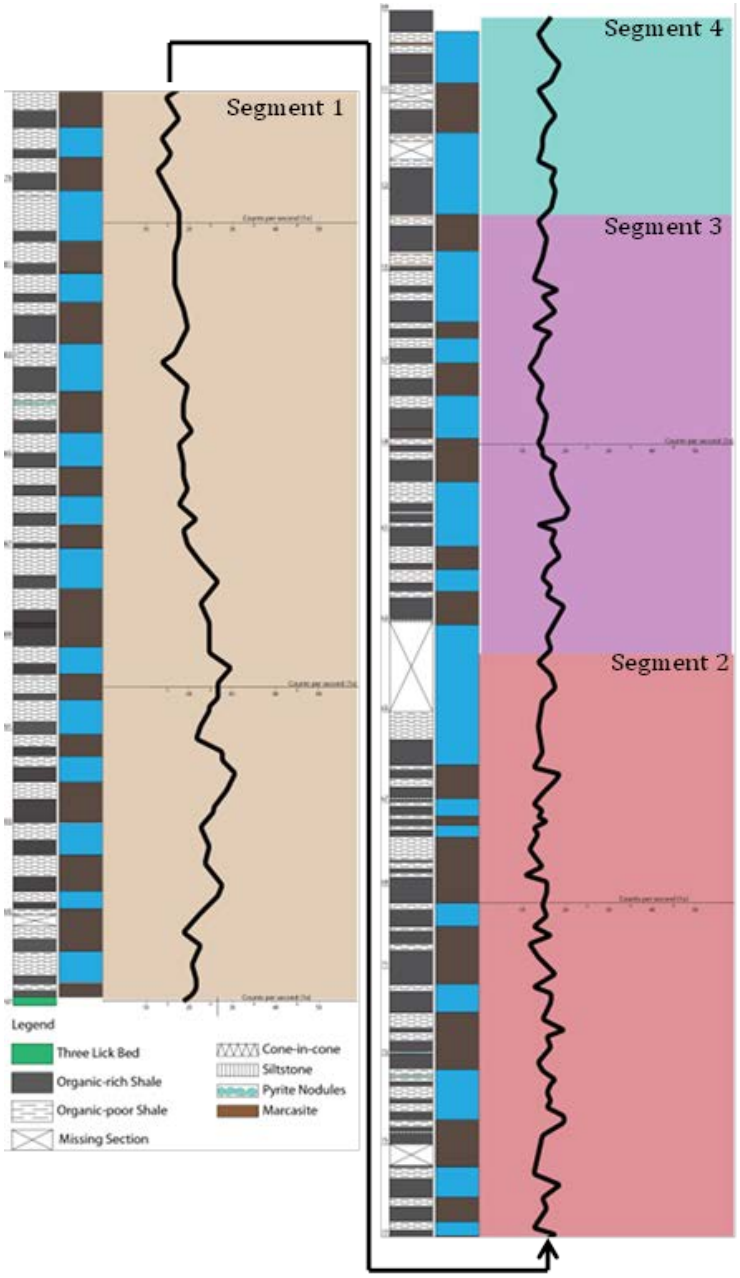


Figure 4. 1. Left-hand column shows core lithology. Second column shows lithologic cycles; color serves only to differentiate between cycles and does not represent any particular characteristic of the cycles. Curve on the far right is a synthetic gamma-ray curve in counts per second (1x). The broader color changes indicate different segments of the curve, defined in terms of wavelength (See Fig. 4.2).

### 4.2. Gamma-ray stratigraphy

The studied core segment was divided into three complete gamma-ray cycles (4th order cycles) and one incomplete cycle using complete cycle wavelengths to identify cycle boundaries (Figs. 4.2, 4.3). These cycles were designated Segment 1 through 4 (Figs. 4.2, 4.3). The cycles average approximately 14-ft (4.27-m) thick, but, in reality, the cycles at this scale become increasingly thinner toward the top of the unit. The thickest cycle, Segment 1, is 18.85-ft (5.75-m) thick, and the thinnest, Segment 4, is 5.75-ft (1.75-m) thick (Table 4.1). Each of these large cycles can be

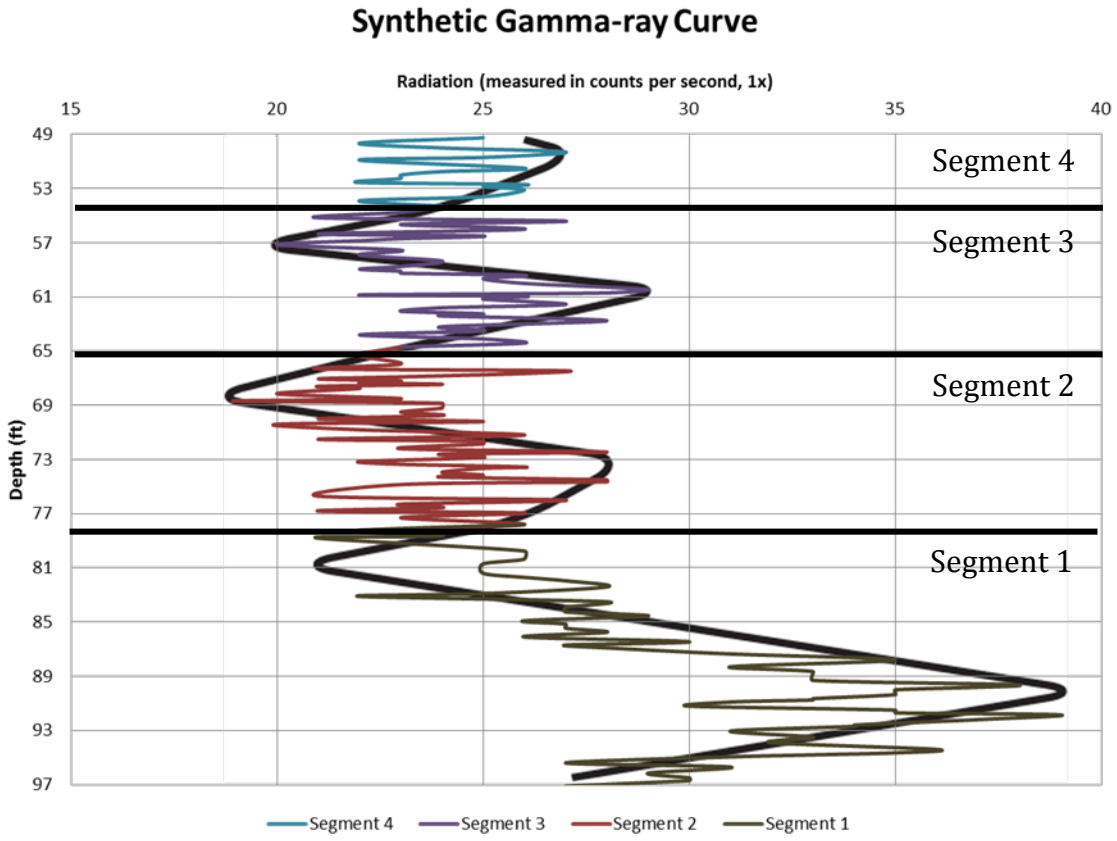


Figure 4. 2. Synthetic gamma-ray curve generated for the D2 core. Radiation was measured in counts per second (1x). The dark line shows the smoothed curve pattern and was used to define cycle segments.

subdivided into several sub-cycles that are designated by a number to indicate of which large cycle they are a part, followed by a letter, for example, 1a-1g (Table 4.2). Segment 1 was divided into seven sub-cycles, which had an average thickness of 2.76 ft. Segment 2 was divided into five sub-cycles which averaged 2.67 ft each. Segment 3 was divided into four sub-cycles which had an average thickness of 2.60 ft. Segment 4, only a partial cycle, was divided into three sub-cycles which averaged 1.68 ft each; segment 4 was the thinnest of the larger cycles and also had the thinnest sub-cycles. A complete table showing radiation values measured in counts per second is available in Appendix A.

Table 4. 1. Sub-cycle thickness within larger cycle segments, as defined in Figs. 4.1-4.3 and Table 4.1.

| Sub-cycle designation | Sub-cycle thickness (ft) | Average sub-cycle thickness (ft) |
|---|---|---|
| 4c | 1.05 | |
| 4b | 1.45 | |
| 4a | 2.55 | 1.68 |
| 3d | 2.40 | |
| 3c | 4.85 | |
| 3b | 1.65 | |
| 3a | 1.50 | 2.60 |
| 2e | 2.65 | |
| 2d | 2.85 | |
| 2c | 2.65 | |
| 2b | 2.05 | |
| 2a | 3.15 | 2.67 |
| 1g | 4.60 | |
| 1f | 2.15 | |
| 1e | 3.25 | |
| 1d | 2.55 | |
| 1c | 1.85 | |
| 1b | 2.60 | |
| 1a | 2.30 | 2.76 |

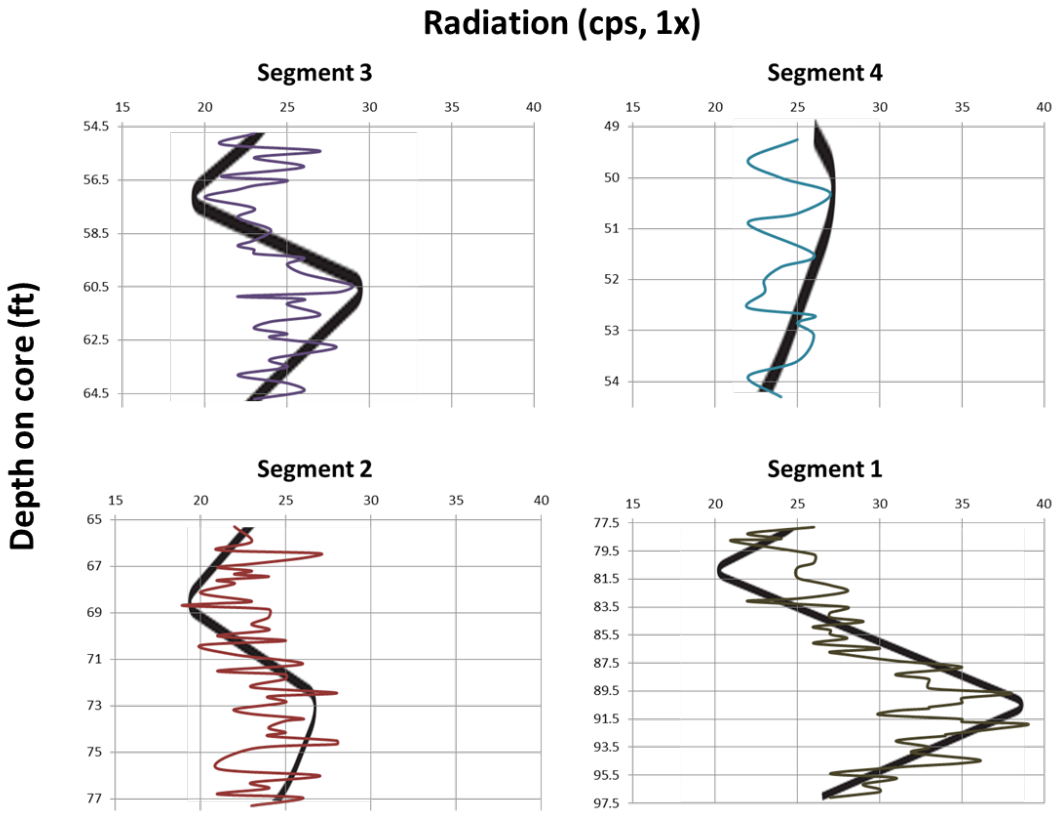


Figure 4. 3. Individual radiation cycle segments with smoothed curve patterns superimposed.

### 4.3. Organic petrography

On a whole-rock basis, vitrinite particles make up 4.38% by volume of the particles identified; the minimum volume of vitrinite counted was 0.40% at 91.82ft and the maximum volume was 14.14% at 92.51 ft. When only organic macerals are considered, vitrinite makes up an average of 36.25% of the total-maceral volume. Inertinite particles account for 2.29% of the total-rock volume and 20.67% of the maceral fraction. The minimum occurs at 89.96 ft and the maximum occurs at 93 ft. Liptinites are the most commonly identified organic macerals in the study interval. They compose 4.71% of the total whole-rock volume on average and 41.87% of the

total-organic maceral fraction. The maximum volume of liptinite occurs at 89.0 ft and the minimum occurs at 89.9 ft. (Fig.4.4; Table 4.3). The complete results of organic petrographic analysis, both whole-rock and mineral-free, are shown in Appendix B.

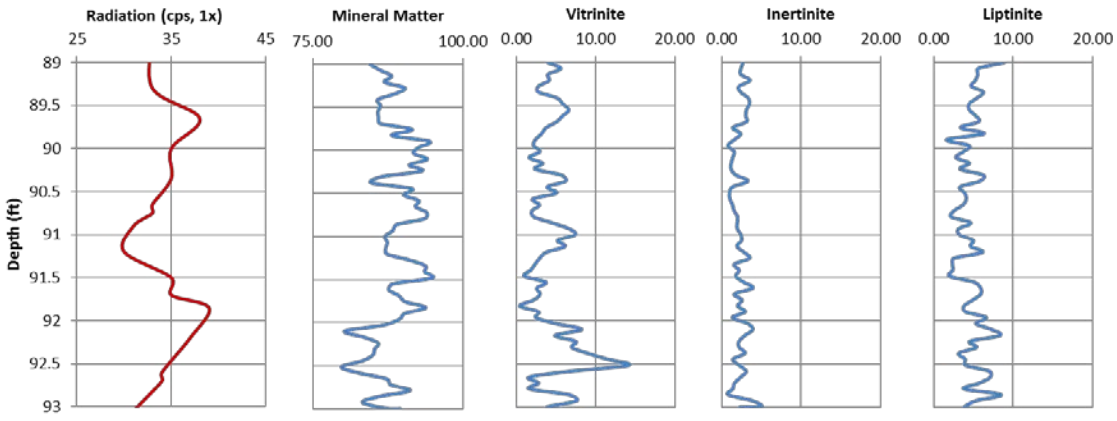


Figure 4. 4. Whole-rock percent by volume of mineral matter, vitrinite, inertinite, and liptinite determined through point counting plotted against depth in core and measured radiation.

Table 4. 2. Percent by volume on a whole-rock basis of vitrinite, inertinite, liptinite, and mineral matter.

| | **Total Vitrinite % (by volume, whole rock)** | **Total Inertinite % (by volume, whole rock)** | **Total Liptinite % (by volume, whole rock)** | **Total Mineral Matter % (by volume, whole rock)** |
|---|---|---|---|---|
| min | 0.40 | 0.78 | 1.58 | 79.68 |
| max | 14.14 | 5.04 | 8.93 | 94.94 |
| **average** | **4.38** | **2.29** | **4.71** | **88.49** |

*4.3.1. Mineral Matter*

Mineral matter composes a minimum of 79.7% and can account for up to 94.9% by volume of these samples, with an average volume of mineral matter of 88.5% (Fig. 4.5; Table 4.4). The minimum value occurs near the base of the study

interval; then, from 92 to 89.75ft, the volume of mineral matter stays high before decreasing from 89.75ft to the top of the study interval (Fig. 4.4). The large volume of clay, counted as matrix material, was the controlling variable for the previously described trend. The volume of silicate minerals (i.e., quartz) varied dramatically with depth (Fig. 4.5). A modest amount of quartz is present in the first half-foot of the study interval; then the silicate volume decreases dramatically and in some samples is completely absent. Then, at 92.25 ft, silicate minerals re-appear and the percent volume remains moderately high to high, for the rest of the study interval with the exception of half-foot intervals around 90.75 ft and 90 ft.

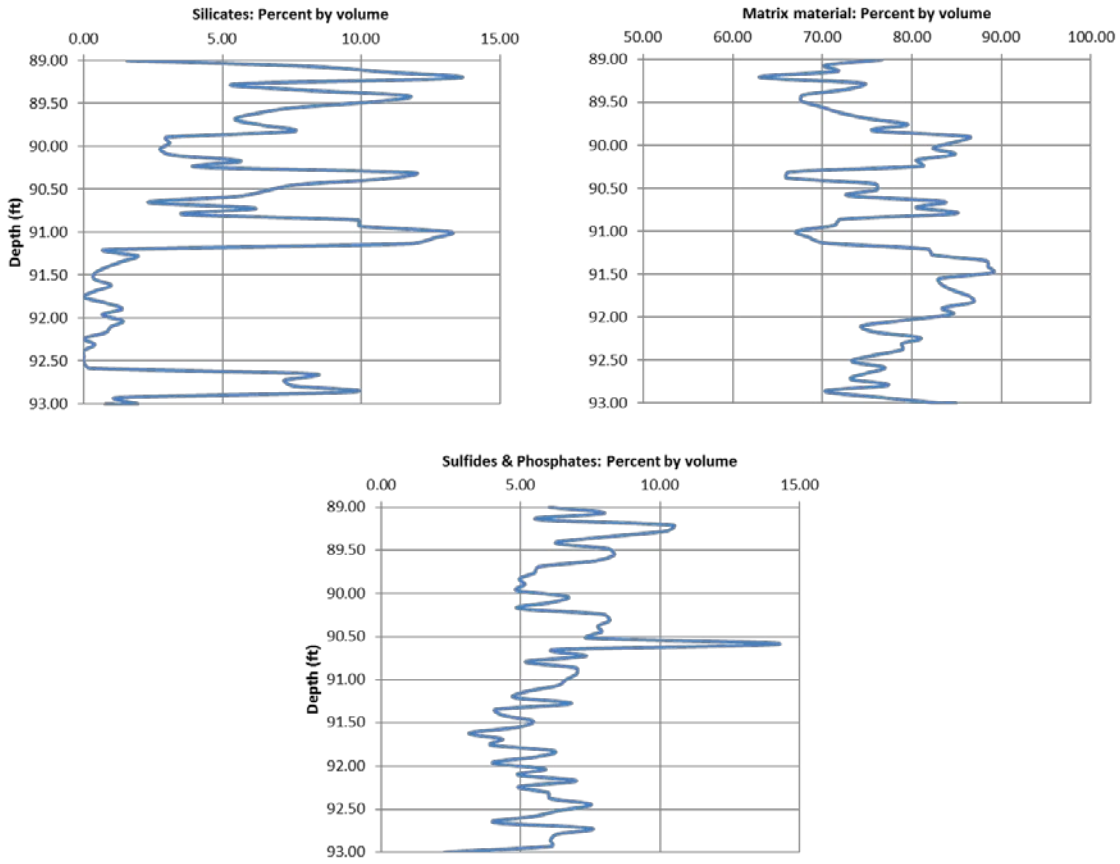


Figure 4. 5. Whole-rock percent by volume of mineral matter, including silicates, sulfides and phosphates. The percentage of clay-rich matrix material was determined by point counting and is plotted against depth in core.

Table 4. 3. Percent by volume on a whole-rock basis of silicates, sulfides and phosphates, and clay-rich matrix material.

| | Silicates % (by volume, whole rock) | Sulfides & Phosphates % (by volume, whole rock) | Clay-rich matrix % (by volume, whole rock) |
|---|---|---|---|
| **Min** | 0.00 | 2.33 | 62.99 |
| **Max** | 13.46 | 14.29 | 89.11 |
| **average** | 4.78 | 6.24 | 77.46 |

The volume of sulfides and phosphates remains fairly constant with depth, with the exception of a positive excursion near 90.5 ft where the volume of sulfides and phosphates increases to 14.3% by volume (Fig. 4.5). The last half foot of the study interval also shows slightly higher-than-average sulfide and phosphate composition (Fig. 4.5).

*4.3.2. Vitrinite and inertinite*

The total volume of vitrinite in the samples decreases up-section (Figs. 4.4, 4.6; Table 4.5). Within the vitrinite group, particles designated as vitrinite follow the same trend, whereas, particles designated as vitrodetrinite show the opposite trend and increase in volume up-section (Fig.4.6). Vitrinite macerals were not observed to fluoresce; this is most likely a function of the excitation filter used in this study. The volume of inertinite, as a group, does not vary that much in relation to core depth, staying within a 4.26% range throughout the study interval (Fig. 4.4). In contrast, however, the composition of the inertinite particles does show variance with core depth. Fusinite and semifusinite compose the majority of the inertinite from 93 to 92 ft, at which point inertodetrinite appears and begins to make up a significant portion of the inertinite. Fusinite and semifusinite continue to make up a significant

portion of the inertinite from 92 to 91 ft, but by 91 ft inertodetrinite makes up the majority of the inertinite fraction.

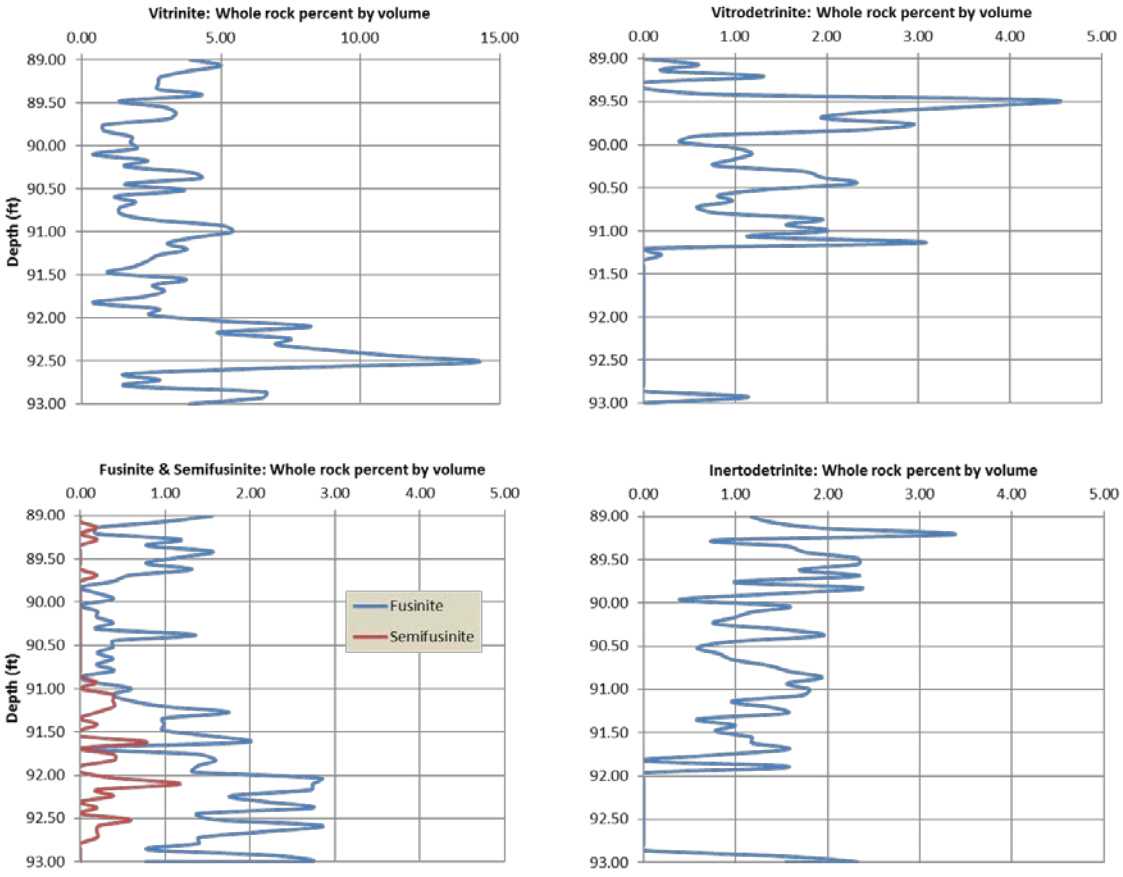


Figure 4. 6. Whole-rock percent by volume of the vitrinite group (upper row), including particulate vitrinite and vitrodetrinite, and of the inertinite group (lower row), including fusinite, semifusinite (plotted together on lower left), and inertodetrinite.

Table 4. 4. Whole-rock percent by volume of vitrinite and inertinite groups as shown in Fig. 4.6.

| | **Vitrinite** | **Vitrodetrinite** | **Fusinite** | **Semifusinite** | **Inertodetrinite** |
|---|---|---|---|---|---|
| **min** | 0.39 | 0.00 | 0.00 | 0.00 | 0.00 |
| **max** | 14.14 | 4.46 | 2.85 | 1.17 | 3.36 |
| **average** | 3.60 | 0.79 | 1.08 | 0.12 | 1.08 |

*4.3.3. Liptinite*

Like the inertinite group, the total volume of liptinitic particles in the study interval varied within a fairly restricted range (Fig. 4.4), the difference between the maximum and minimum values being only 7.35% (Fig. 4.7; Table 4.6). Once again, though, where the liptinitic macerals are viewed separately, variations with depth do emerge (Fig. 4.7). Lamalginite and bituminite are most abundant below 91.5 ft, but their volumes decrease between 91.5 ft and the top of the study interval. After initially composing a relatively high percent of the liptinite fraction, the volume of telalginite decreases between 92.5 ft and 91.5 ft, after which the total percent of

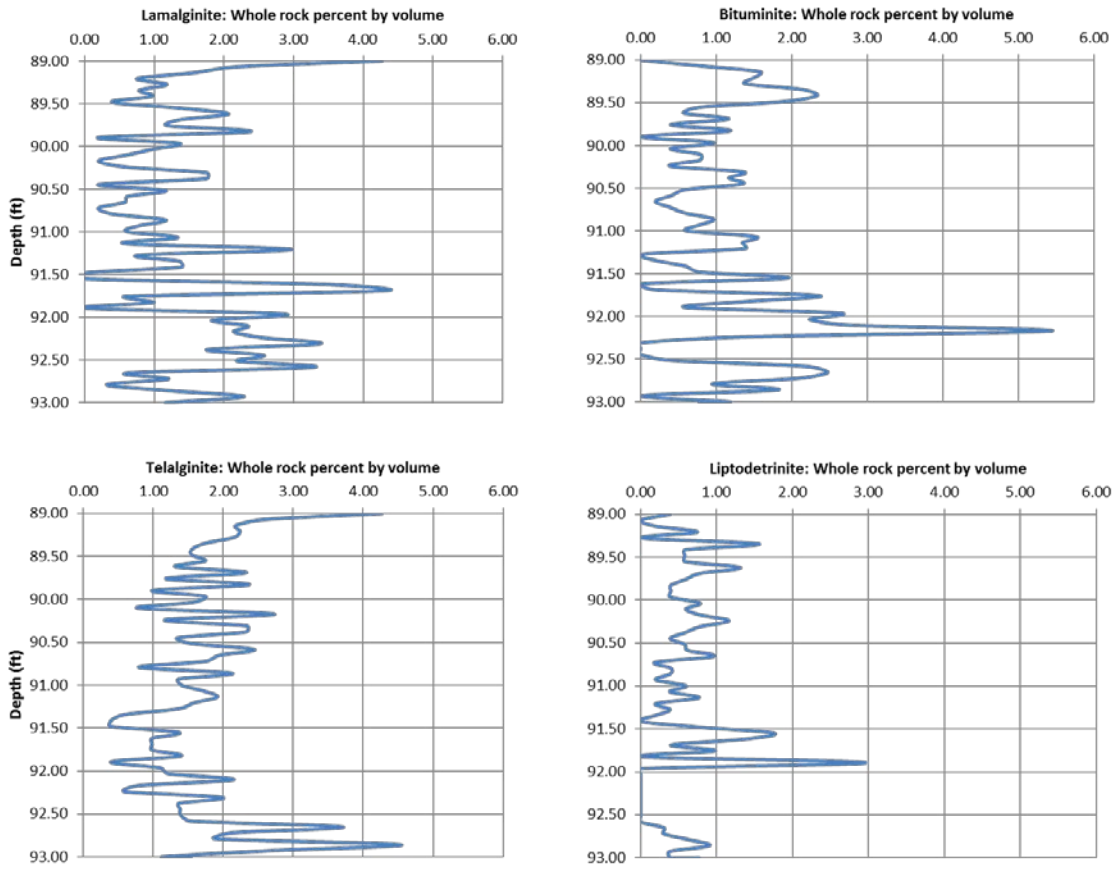


Figure 4. 7. Whole-rock percent by volume of the liptinite group, including lamalginite, bituminite, telalginite, and liptodetrinite.

telalginite increases again. Liptodetrinite is almost absent until 92 ft, where an anomalous peak occurs (Fig. 4.8). The liptodetrinite content then rapidly decreases until the volume generally stabilizes from 91.5 ft to the top of the section.

Table 4. 5. Whole-rock percent by volume of the liptinite group, including lamalginite, bituminite, telalginite, and liptodetrinite.

| | **Sporinite** | **Telalginite** | **Liptodetrinite** | **Lamalginite** | **Bituminite** |
|---|---|---|---|---|---|
| **Min** | 0.00 | 0.39 | 0.00 | 0.00 | 0.00 |
| **Max** | 0.00 | 4.55 | 2.96 | 4.34 | 5.44 |
| **average** | 0.00 | 1.68 | 0.52 | 1.41 | 1.10 |

### 4.4. X-ray Fluorescence

The measured proxies for clastic influx all show somewhat similar trends (Fig. 4.9) with high ratios occurring between 92 and 91.5 ft, followed by a low ratio, then by a high ratio that peaks at about 90.5 ft. Another interval of low ratios reaches its minimum at about 90 ft, with overlying ratios then increasing at about 89.75 ft before falling again toward the top of the study interval. R-mode cluster analysis (Dendrogram available in Appendix D) shows that Si content is primarily responsible for variations within the elemental data; nonetheless, the elements can be divided into two prominent clusters. The first group clusters under Al and contains the elements K, Ca, and Fe; this group represents the clay fraction of the clastic input. The second group clusters under Ti and appears to represent the more coarse-grained sediments; this is indicated by the presence of Zr in the group, as titanium and zircon tend to reside in rutile and zircon grains (Jaminski et al., 1998).

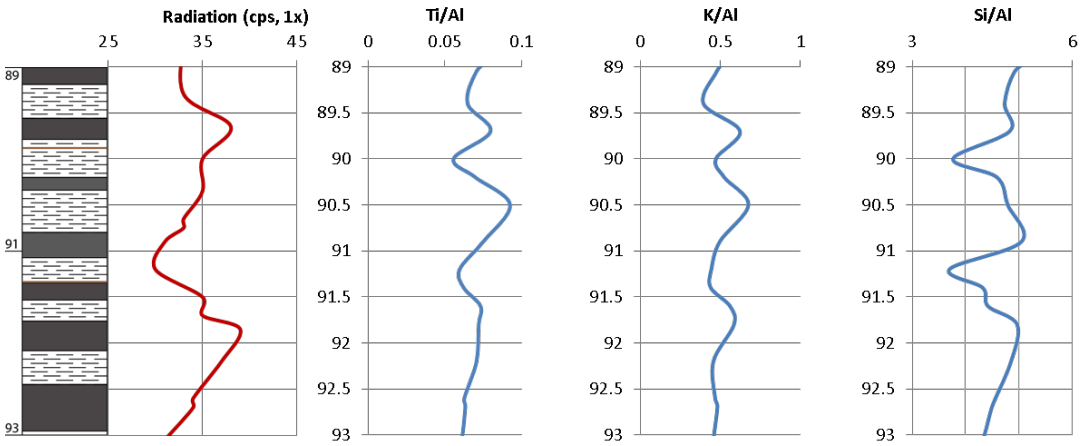


Figure 4. 8. Proxies for clastic influx, Ti/Al, K/Al, and Si/Al, plotted against depth in core, radiation (cps, 1x), and lithology.

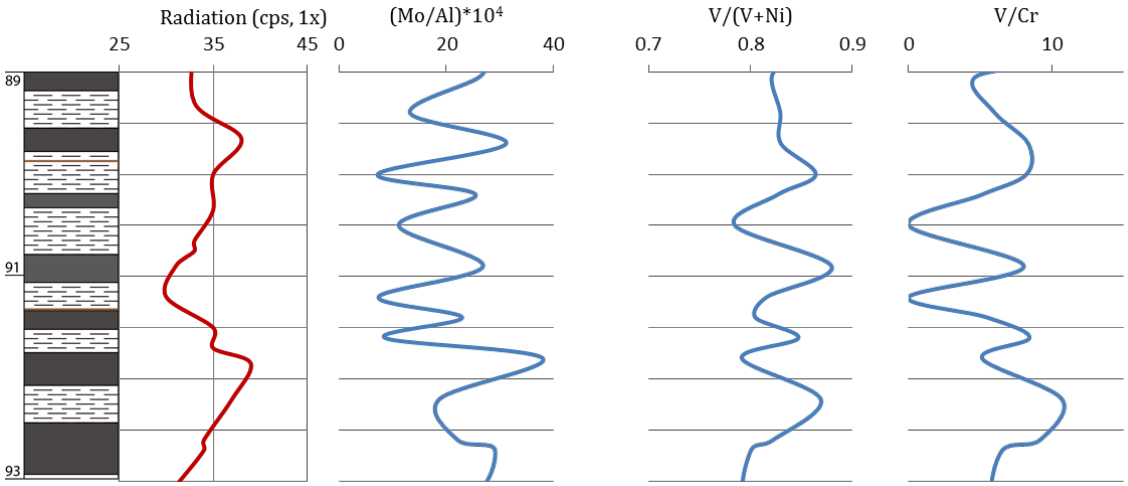


Figure 4. 9. Paleo-redox proxies Mo/Al, V/(V+Ni), and V/Cr plotted against depth in core, radiation (cps, 1x), and lithology.

Both Al-normalized and trace-element ratios can be used as paleo-redox proxies (Rimmer, 2004). For this study, (Mo/Al)x$10^4$, V/(V+Ni), and V/Cr have been used as paleo-redox proxies (Fig. 4.9). V/(V+Ni), and V/Cr displayed very similar trends when plotted against core depth, and the overall shape of these curves generally parallels that of the synthetic gamma-ray curve, with highs occurring

between 92 and 91.5 ft and again between 90 and 89.5 ft with lower values in between. The (Mo/Al)x$10^4$ curve, on the other hand, varies strongly with lithology. Peaks in the Mo/Al ratio coincided with more organic-rich sections of the core, whereas the lows coincided with the less organic-rich sections.

A complete inventory of the major and trace-element readings is available in Appendix C.

### 4.5. Total Carbon and Sulfur

Total carbon varies between 2.81 and 9.12% in the lower part of the Cleveland Shale between core depths of 97 to 87 ft (Fig. 4.10; Table 4.7). Most of the carbon in this part of the Cleveland sample is organic carbon (Fig. 4.10; Table 4.7). Inorganic carbon usually contributes less than 0.1% to the total-carbon content, with the exception of the sample at 92 ft, which contains 0.32%. Sulfur content over this interval varied between 1.64 and 2.43% (Table 4.7), most of which is thought to be pyritic sulfur based on the work of Taulbee et al (1990).

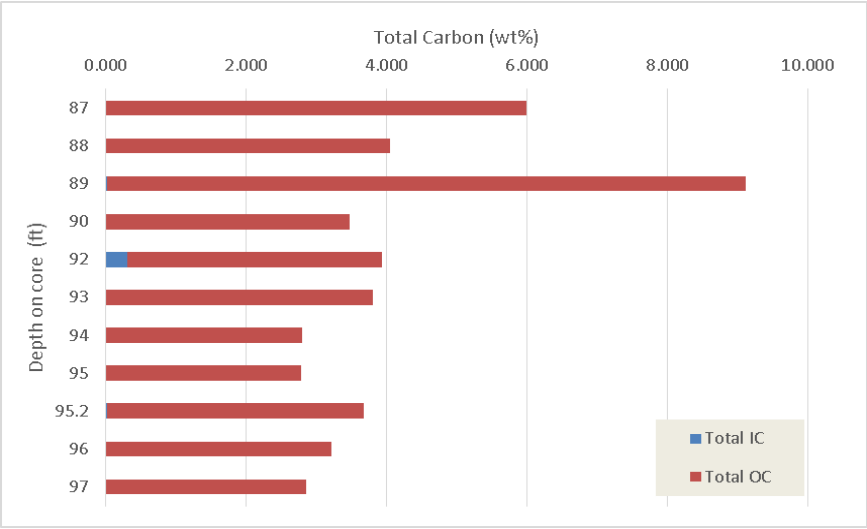


Figure 4. 10. Total carbon plotted against depth in core.

Table 4. 6. C-S weight percent.

| **Cleveland Shale Samples** | | | | |
|---|---|---|---|---|
| | | | | |
| **Sample Depth (ft)** | **Total C** | **Total IC** | **Total OC** | **Total S** |
| 87 | 6.00 | 0.000 | 6.00 | 1.78 |
| 88 | 4.06 | 0.001 | 4.06 | 1.95 |
| 89 | 9.12 | 0.021 | 9.10 | 1.64 |
| 90 | 3.47 | 0.014 | 3.46 | 2.31 |
| 92 | 3.94 | 0.316 | 3.62 | 2.34 |
| 93 | 3.81 | 0.000 | 3.81 | 1.68 |
| 94 | 2.81 | 0.000 | 2.81 | 2.06 |
| 95 | 2.79 | 0.001 | 2.79 | 2.43 |
| 95.2 | 3.69 | 0.027 | 3.66 | 1.80 |
| 96 | 3.22 | 0.001 | 3.22 | 1.85 |
| 97 | 2.87 | 0.016 | 2.85 | 2.18 |

# CHAPTER 5: DISCUSSION

## 5.1. Lithology

Conodont zonal analysis and zonation allow for the temporal correlation of units across time horizons. The original conodont zonation used for the Famennian was proposed by Ziegler (1962) and modified by Ziegler and Sandberg (1990). Using this zonation, as well as work done by Woodrow et al. (1988) and Ziegler (1990), Jaminski et al. (1998) estimated that the Cleveland Shale had been deposited over a duration of 2.5 ka. However, recent work on the Devonian *S. preasulcata* zone by Over et al. (2009) has shown that the Cleveland Shale Member of the Ohio Shale extends downward into the upper *P. expansa* zone (Fig. 5.1). Plotting this information against the Devonian radiometric timescale (Becker et al., 2012) constrains the deposition of the Cleveland to 361.7– 359.3 Ma, giving it a total

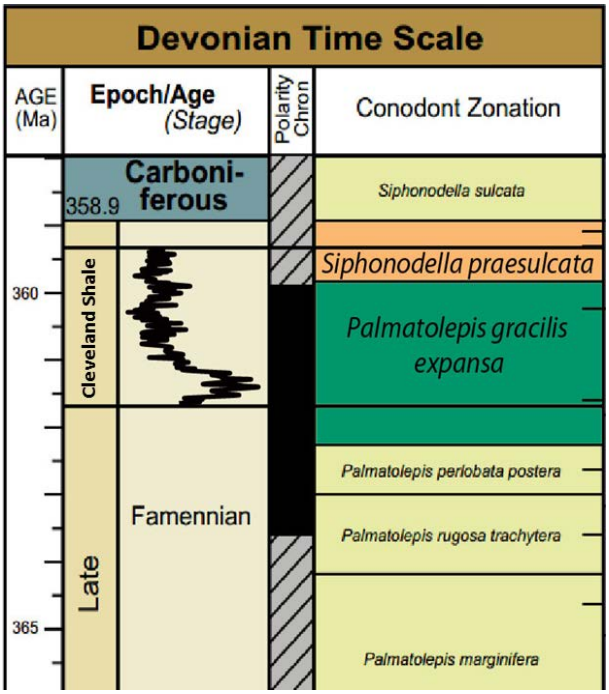


Figure 5. 1. Biostratigraphic timescale for Famennian with limits of Cleveland Shale deposition marked (Becker et al., 2012).

formation duration of 2.4 (±0.3) Ma (Figure 5.1). Based on lithologic characterization of the core, 56 complete lithologic cycles were identified (Fig. 5.2). Assuming that each cycle is of the same approximate thickness and that depositional rates were uniform, the average cycle length is therefore about 40 (± 2.5) ka (Table 5.1).

The typical gamma-ray curve for the Cleveland is commonly assumed to be a high (positive deflection) – low (negative deflection) – high (positive deflection)

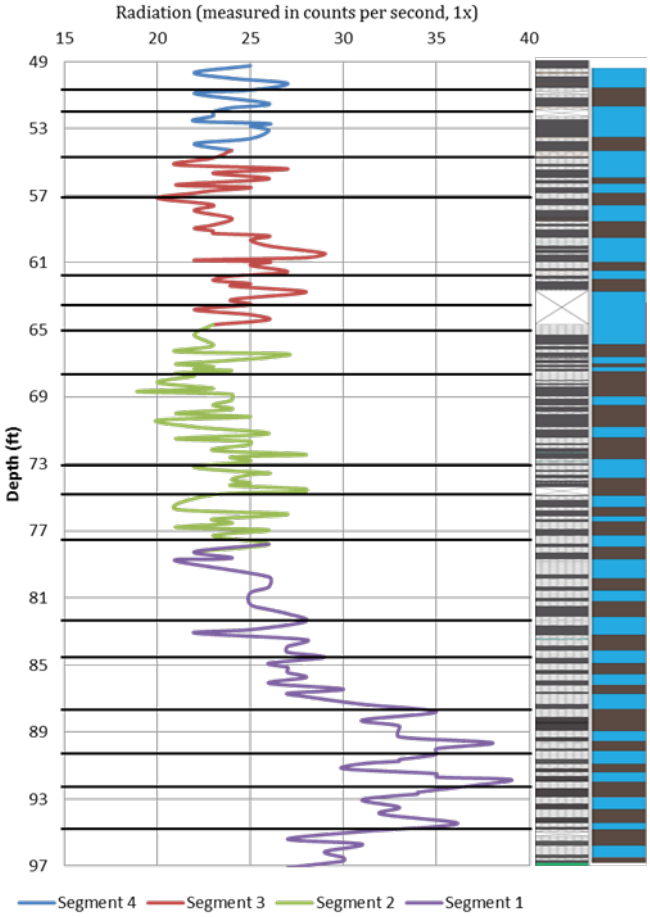


Figure 5. 2. Synthetic gamma-ray curve with third-order cycles represented by different colors and fourth-order cycles marked with black lines. To the right, core lithology and fifth-order cycles. Each brown/blue pair represents one cycle.

pattern of deflections (Ettensohn et al., 1988). However, in this core the pattern is a little more complex with a high – low – high – low – high pattern. However, when compared to Cleveland gamma-ray signatures across the Appalachian Basin (Kepferle et al., 1978), the signature is not so unusual, as these signatures change with proximity to source areas to the east–northeast and the influx of siltstones into the section. The presence of thin siltstones (< 0.05-ft thick) in this section may reflect a similar situation. Nonetheless, the synthetic gamma-ray curve generated during this study (Figs. 4.1, 4.2) shows that there were three complete cycles which can be correlated with the regional cycles observed in the "type-log" for this section. Based on the temporal scale of Becker et al. (2012), each of these cycles represents approximately 600 ka, assuming equal cycle lengths (Fig 5.2; Table 5.1). The gamma-ray curve can be further divided into 19 smaller cycles, which represented 119 (±8.1) ka on average (Fig. 5.2; Table 5.1).

Table 5. 1. Cycle order and probable cause (Mitchum and Van Wagoner, 1991; Filer, 1994) based on method and average duration.

| **Method** | **Number of Complete cycles** | **Average Duration (ka)** | **Cycle Order** | **Probable Cause** |
|---|---|---|---|---|
| **Gamma-ray** | 3 | 600 | Third to Fourth-order | Changes in mid-oceanic ridge growth and continental ice growth and decay |
| **Gamma-ray** | 19 | 120 | Fourth-order | Eccentricity |
| **Lithology** | 56 | 40 | Fifth-order | Axial tilt, obliquity |

The combined data from lithologic characterization and gamma-ray stratigraphy reveal three levels of cyclicity (Fig. 5.2). The length of the large gamma-ray cycles, which is variable but approaches a million years in the lower Cleveland, makes it possible that these cycles represent third-order cyclicity (Table 5.1). The average duration of the 19 smaller gamma-ray cycles suggests fourth-order cyclicity (Table 5.1). Finally, the 56 complete lithologic cycles represent a previously unknown fifth-order cyclicity in the Cleveland Shale (Table 5.1).

### 5.2. Discussion of organic petrography results

The reflectance of vitrinite and vitrinite-like material increases with maturity (Hutton et al., 1994). The measured vitrinite reflectance of the Cleveland Shale is approximately 0.5%, indicating that this shale is fairly immature (Rimmer et al., 1993). Although thermal alteration does occur, even at this low thermal maturity, changes in the organic material are minimal compared to samples at higher ranks (>1.0%). Therefore, it can be assumed that the geochemical and petrographic composition of the Cleveland Shale largely reflects conditions at the time of deposition (Rimmer et al., 2004).

Before interpretations about organic-maceral depositional systems can be made, the origin of the organic matter must be considered, that is, fundamentally, whether the organic matter was generated within the basin or outside the basin and then transported before being deposited. Determining where the organic matter was generated is best accomplished by comparing the relative amounts of the different maceral populations based on their likely generation points. Inertinite and vitrinite are generally accepted to have had terrestrial origins, whereas liptinite,

with the exclusion of sporinite, is typically assumed to have had a marine origin. In other words, vitrodetrinite and inertodetrinite are allochthonous and liptodetrinite is autochthonous. The terrestrial/marine ratio for this section shows an overall decrease up-section (Fig. 5.3), so that more of the organic matter is of marine origin when moving up-section. Additionally, there is a subtle cyclicity in the T/M ratio which appears to be controlled by lithology as the sections with the greatest volume of terrestrially derived organic matter coincide with less organic-rich sections of the core (Fig. 5.3). The areas adjacent to siltstones in the core also contain more terrestrial- than marine-derived organic matter, indicating that this organic matter was most likely transported with the more coarse-grained sediments.

This trend of declining terrestrial organic matter toward the top of the core appears to be contrary to previous work, which indicated that the overall amount of terrestrial organic matter increases from the base of the Cleveland to the top (Robl et al., 1987; Rimmer et al., 1993, 2004). These differences, however, are most likely explained by the location of the examined section and the fact that this study does

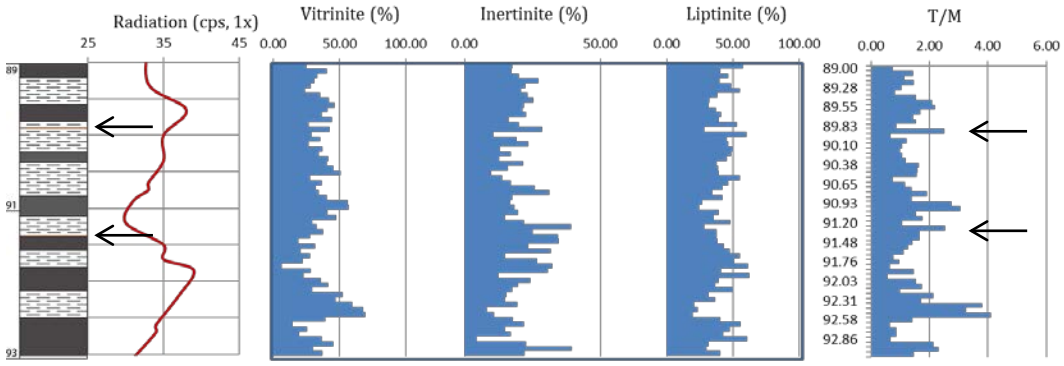


Figure 5. 3. Variation in organic petrographic composition with depth (shown as %, mineral-free basis), T/M = terrestrial/marine. Radiation and lithology are shown for comparison.

not examine the entire core. In fact, the section of core that was examined in this study was only from the base of the Cleveland. The Cleveland in the D2 core begins at 97 ft and extends upward to 49 ft, and the section that was chosen for organic petrography only includes parts of the core from 93 to 89 ft. Another possible explanation is the inherent difficulty of positively differentiating finely-divided vitrinite from bituminite. Some of the material identified as bituminite in this study may have been identified as vitrinite in previous studies, which would have altered the terrestrial/marine ratio. However, because the examined section of the core was so close to the base of the Cleveland Shale Member, it is not surprising that this section had more marine than terrestrial organic matter as this part of the section represents major deepening and transgression following the Three Lick progradation.

Of course, simply stating that a greater percent of organic matter has a marine origin than terrestrial does not fully explain the processes through which the organic matter accumulated. Changes in the depositional regime are commonly reflected in the changing volume of individual maceral groups as well as by maceral morphology and size. Hence, examining the terrestrial organic matter can provide important information about the processes through which sediment was transported into the basin. Comparison of the silicate and clay-rich matrix material with the terrestrial macerals (Fig. 5.4), for example, shows that the amounts of vitrodetrinite and inertodetrinite were related to the volume of silicate minerals ($r$=0.532 and 0.305 respectively; significant at the 99% confidence level), and that the combined volume of fusinite and semifusinite was related to the volume of the

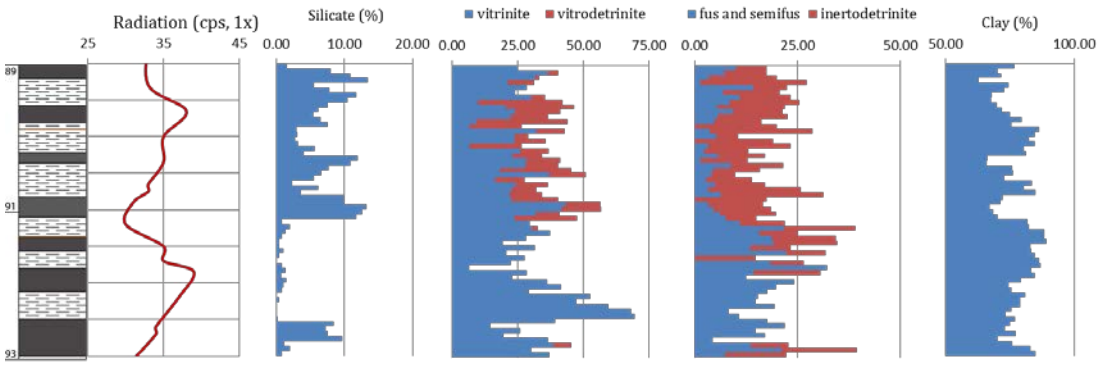


Figure 5. 4. Variation in volume of silicate minerals, clay-rich matrix material, vitrinite and vitrodetrinite, and inertinite and inertodetrinite. The mineral matter is shown as a whole-rock basis and the organic macerals are shown as %, mineral-free basis. Lithology and gamma-ray curve shown for comparison.

clay-rich matrix material ($r$=0.354). The association of very tiny fragments of terrestrial vitrinite and inertinite with silicate minerals indicates that these macerals were broken down during transportation from the source area into the Appalachian basin and suggests fluid transport. Fusinite and semifusinite (fossil charcoal) are typically transported by wind, because after wood and swamp fires, pieces of charcoal accumulate and blow away easily. The same is true for fine humus on dried-out peat surfaces, as black, carbon-rich dust settles in water to form sediment there. Therefore, the association of the clay-rich material in these samples with inertinite indicates that eolian processes deposited a significant amount of the sediment that formed the Cleveland Shale.

Another line of evidence for the concept of multiple methods of deposition and/or varying rates of deposition within the basin is the presence of two vitrinite populations. There are two populations of vitrinite observed in this study; one, which will be referred to as “true vitrinite”, and another, which will be called “dispersed vitrinite.” The true vitrinite consists of larger vitrinite particles, which

display relief against the surrounding matrix material and a medium-gray reflective surface (Fig. 5.5, left); these particles can be up to 200-µm across and locally preserve cell structure. Dispersed vitrinite, in contrast, occurs in dark, elongate bands of varying width and often has matrix material and vitrodetrinite incorporated into it (Fig. 5.5, right). The volume of vitrinite, excluding vitrodetrinite, has a negative correlation with the volume of silicate minerals in these samples (*r*=-

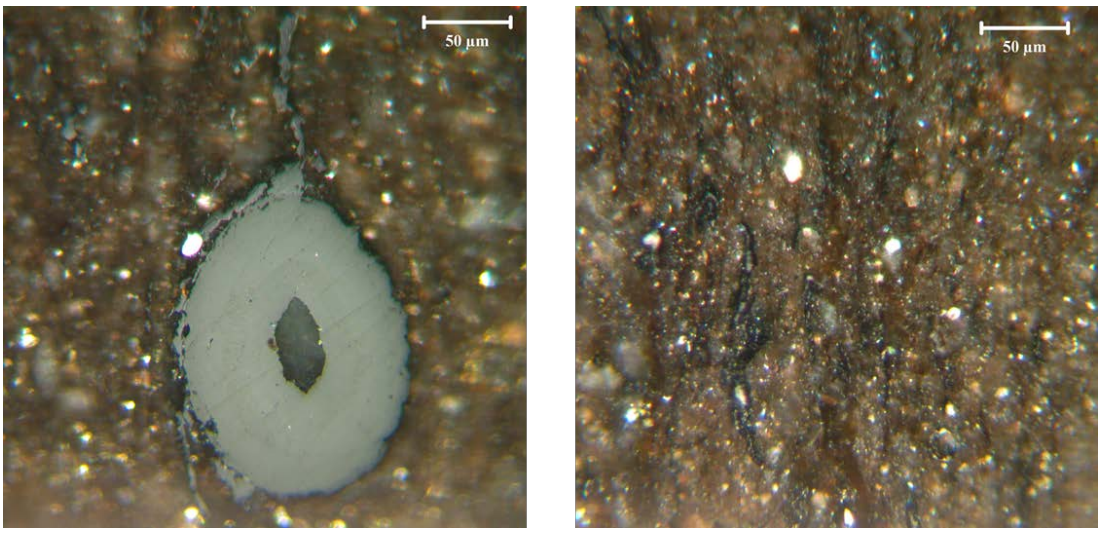


Figure 5. 5. Left: true vitrinite showing preserved cell structure. Right: stringy, dark bands of dispersed vitrinite.

0.273; significant at the 97.5% confidence level), so it appears that increased silicate sedimentation is related to decreases in the volume of vitrinite. This relationship is likely due to the previously mentioned fluid-transport mechanism of terrestrial material, which acted to break down larger pieces of vitrinite into detrinite-size particles. Due to the large size of the "true" vitrinite, it is unlikely that these particles represent windblown sediments, and, because these particles occur alone in sediment containing abundant marine organic matter, it is most likely that these

particles were transported into the basin via rafting (possibly ice rafting) as has been documented in the Campo Chico Formation in Venezuela (Berry and Fairon-Demart, 2001). Once the true vitrinite entered the basin, deposition would have been rapid and the particles would have experienced little secondary degradation.

Dispersed vitrinite, on the other hand, was likely deposited as the result of eolian processes and prolonged exposure to degradational processes in a stratified water column. This population of vitrinite macerals would have been carried into the basin by winds blowing off the Acadian highlands, possibly across glacial outwash plains, and then would have been distributed across the Appalachian Basin by Eckman transport. Due to its small size, dispersed vitrinite probably had a slower settling rate than the true vitrinite, so that these particles were exposed to oxygen and bacterial reworking in the water column for an extended period of time. This degraded vitrinite would have then been deposited in a thin film so that the observed morphology in cross section would be thin, elongate bands such as the ones observed in this study (Fig. 5.5, right). The slow settling rate would also explain the inclusion of matrix material in these bands, as the dispersed vitrinite would have been deposited at approximately the same rate as the clay minerals, or perhaps combined with the clay (mineral matrix) as floccules.

Results from this study (Figs. 4.4, 4.6, 4.7, 5.6) show that inertodetrinite and liptodetrinite began entering the sedimentary record at approximately the same point, that is, they both first appeared in the same petrographic pellet. Some of this inertodetrinite likely originated within the basin, and, in fact, up to 2-4% of the inertodetrinite could have originated through the severe degradation of algal

material (Rimmer et al., 2004). However, without clear evidence to suggest a marine origin it is assumed, based on its reflectance (Jones et al., 1991) and morphology (Jones and Chanoler, 1991), that the overwhelming majority of the inertodetrinite had a terrestrial origin. On the other hand, electron-microscope studies have shown that the most common components of liptodetrinitic materials are fragmented alginite and suberinite, as well as tiny, unicellular algae (Madler, 1968; Teichmüller and Ottenjann, 1977). However, as no suberinite was observed in these samples, and, as suberinite has only been observed in Tertiary and Mesozoic coals (Teichmüller et al. 1998), the liptodetrinite here can be assumed to be primarily composed of fragmented, marine alginite. Therefore, depositional mechanisms must be able to account for the presence of both terrestrial and marine organic matter.

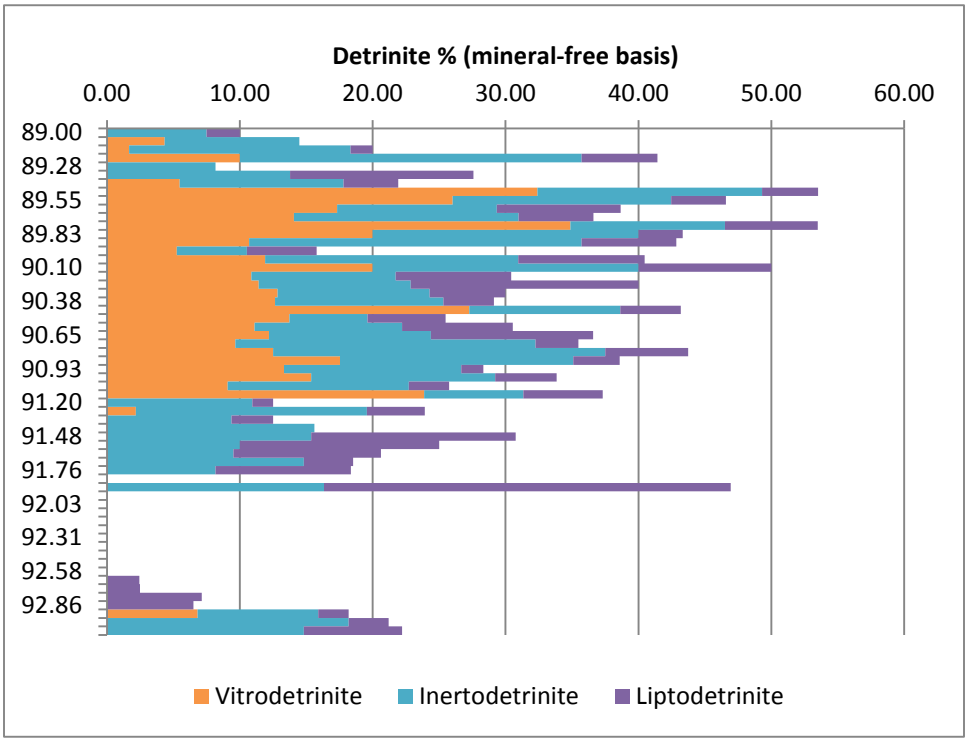


Figure 5. 6. Volume of detrinite-size macerals plotted against depth on a mineral-free basis.

One such mechanism is reflected in changes in the volume of fluvial runoff into the basin. The impact of fluvial runoff is supported by evidence from modern coastal settings, such as the Amazon River (Gibbs, 1967, 2009) and the Zaire River (Cadee, 1978; van Bennekom et al., 1978), which showed that fluvial runoff can increase productivity in estuaries and restricted areas of coastal oceans and seas (Piper and Calvert, 2009). As a restricted basin, the Black Shale Sea (Figs. 1.5, 1.10) would have been sensitive to changes in the volume of fluvial runoff. An increase in fluvial runoff would have increased the volume of inertodetrinite and vitrodetrinite that was transported into the basin, and the increased nutrient load would have stimulated the growth of marine algae and created more liptodetrinite.

Differences in the maceral ratios can also provide clues as to sedimentation rates and the amount of bacterial reworking at the time of deposition. The amount of bituminite, relative to the amount of vitrinite and alginite, is particularly useful for this. Bituminite is formed through the bacterial degradation of organic matter, and therefore, changes in the alginite/(alginite+bituminite) ratio reflect changes in the amount of bacterial degradation (Taulbee et al., 1990). The vitrinite/(vitrinite+bituminite) ratio is useful because terrestrial organic matter is more resistant to decomposition than marine organic matter (Hedges et al., 1988), so that increases in the amount of well-preserved terrestrial organic matter are indicative of slow rates of deposition (Canfield, 1994). In the lower Cleveland, the alginite/(alginite+bituminite) and the vitrinite/(vitrinite+bituminite) ratios were fairly high, with the volume of well-preserved organic matter dominating the volume of degraded organic matter (Fig. 5.7), indicating that there was little

bacterial reworking of the organic matter prior to deposition. Moreover, the consistently high vitrinite/(vitrinite+bituminite) ratio indicates that the overall rate of deposition was slow. Additionally, the alginite/(alginite+bituminite) ratio does not significantly diverge from the vitrinite/(vitrinite+bituminite) ratio, meaning that marine productivity must have remained high, because otherwise the alginite/(alginite+bituminite) ratio would have been lower than the vitrinite/(vitrinite+bituminite) ratio.

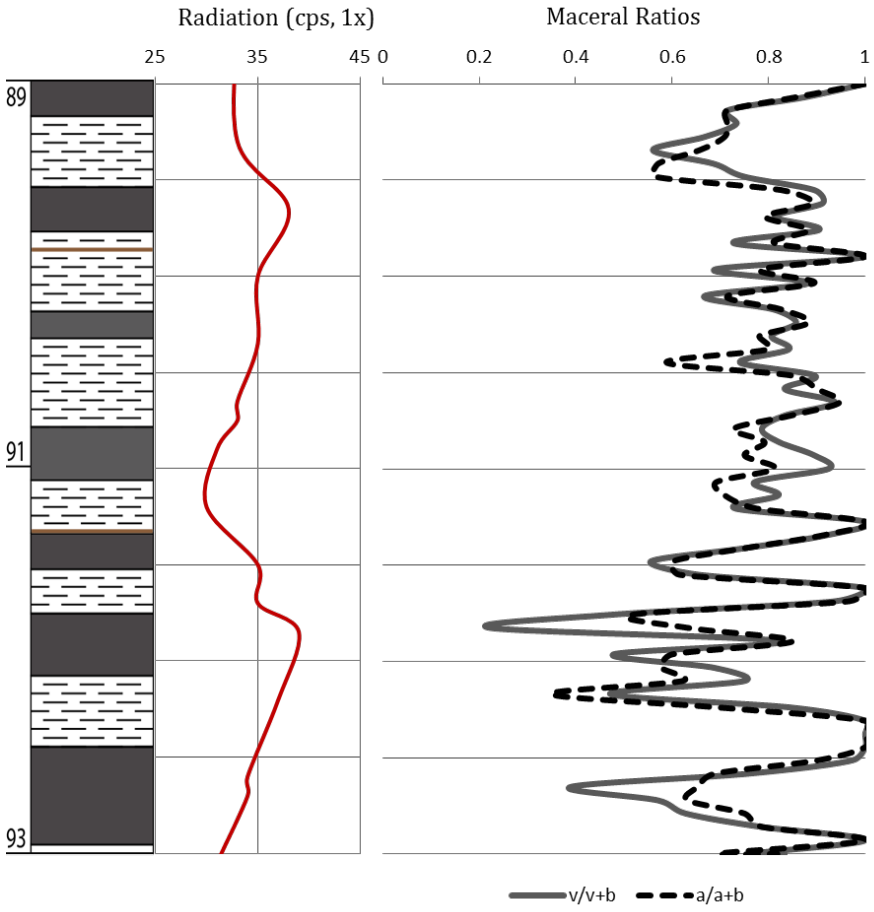


Figure 5. 7. Maceral ratios for core interval. Abbreviations for maceral ratios: v = vitrinite, b = bituminite, and a = alginite; high ratios indicate an increase in the volume of well-reserved organic matter relative to poorly preserved, bacterially reworked organic matter.

There are exceptions to these generalizations, and negative deflections are observed in the curves of these ratios at 92.75 ft, between 92.25 and 91.75 ft, at 90.50 ft, and just above 89.50 ft (Fig. 5.7). At these depths the alginite/(alginite+bituminite) and the vitrinite/(vitrinite+bituminite) ratios decrease significantly, likely the result of enhanced bacterial reworking. These decreases ratios are most likely not caused by an increase in the rate of sedimentation, because the alginite/(alginite+bituminite) ratio is significantly higher than the vitrinite/(vitrinite+bituminite) ratio, with the exception of the deflection at 90.50 ft. Large volumes of alginite and vitrinite relative to bituminite indicate periods of enhanced bacterial reworking. The relationship between the volume of bituminite and lithology is varied, likely due to the complex relationship between productivity, sediment flux, and redox conditions within the water column. However, the relative volumes of well-preserved vitrinite versus well-preserved alginite can be used to identify changes in sediment flux. Terrestrial organic matter is more resistant to bacterial reworking than marine organic matter; so where the volume of well-reserved alginite is greater than the volume of well-preserved vitrinite it is likely that marine productivity was high and that the rate of sedimentation was slow.

By comparing the combined volume of sulfides and phosphates (Fig. 4.5) in the samples to the volume of bituminite/(bituminite+alginite), it is possible to determine whether the accumulation of bituminite was controlled by the degree of anoxia or by productivity rates. High volumes of bituminite, associated with greater amounts of bacterial reworking, are related to higher rates of sulfate reduction and

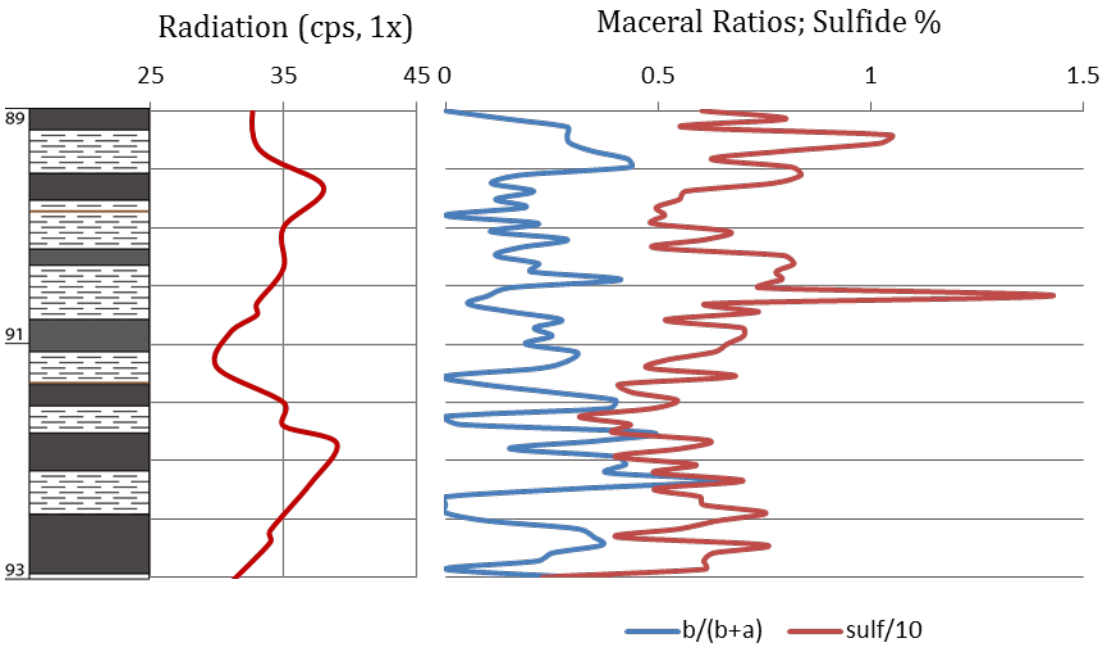


Figure 5. 8. Maceral ratios for core interval and sulfide % by volume. Abbreviations for maceral ratios: b = bituminite, and a = alginite. Note that the sulfide content has been divided by ten to more clearly demonstrate the relationship between the two.

$H_2S$ production (Jaminski et al., 1998), and, hence, to increasingly anoxic to euxinic conditions which promote the preservation of organic matter. When these two populations are plotted together (Fig. 5.8), it becomes evident that the curves generally parallel each other; therefore, where large volume of sulfides occur in the lower Cleveland, it can be assumed most of the organic matter that was deposited in the anoxic zone was preserved. Under the oxygen-depleted conditions implied by large volumes of sulfide minerals, organic matter would have experienced little post-depositional alteration so that any bacterial degradation of organic matter into bituminite must have occurred in the upper water column before deposition. It has been suggested that some bituminite is derived from algal/bacterial masses preserved in sediments beneath the oxic/anoxic interface within the water column

(Sherwood and Cooke, 1984). The volume of sulfide (Fig. 5.8) shows that the increase in bituminite production marked by the negative deflection between 92.25 and 91.75 ft (Fig. 5.7) (shown as a positive deflection in Fig. 5.8) was caused by prolonged bacterial reworking, likely due to the presence of a strongly stratified water column so that prolonged bacterial reworking in the upper water column was possible. The alginite/(alginite+bituminite) and vitrinite/(vitrinite+bituminite) ratios (Fig. 5.7) show that marine productivity was high and that the overall rate of sedimentation was slow; however, these observations alone cannot adequately explain variations in the amount of bituminite. The paleo-redox proxies discussed in section 5.3 provide further evidence to explain these changes.

### 5.3. Discussion of x-ray fluorescence results

The nature of paleo-redox conditions, or the degree of anoxia, in the Black Shale Sea is a critical question which must be answered before a depositional model can be proposed. These conditions can be determined through the use of several geochemical proxies such as V/(V+Ni), V/Cr (Fig. 5.9), (Mo/Al)x$10^4$ (Fig. 5.10), and the Mo Enrichment Factor (Fig. 5.10; Table 5.2). The results of this study show that conditions within the basin were consistently anoxic (a complete lack of oxygen in the bottom waters) to euxinic (no oxygen is present in the bottom waters and hydrogen sulfide is being produced) during deposition of the lower Cleveland.

The V/V+Ni proxy (Fig. 5.9) is especially illustrative of this situation as values between 0.54-0.82 indicate anoxia, whereas values greater than 0.84 indicate a euxinic environment (Hatch and Leventhal, 1992). All V/(V+Ni) ratios were well within the anoxic range, and at several places along the core, the V/(V+Ni) ratio

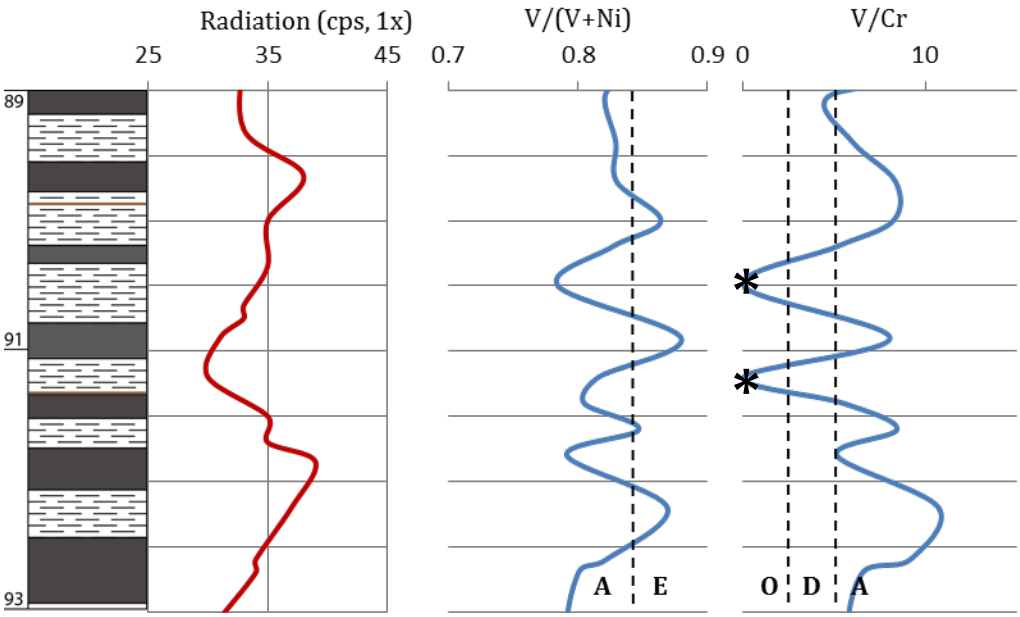


Figure 5. 9. Trace-element paleo-redox proxies V/(V+Ni) and V/Cr. Lithology and gamma-ray curve shown for comparison. O = oxic, D = dysoxic, A = anoxic, and E = euxinic. * = Cr below limit of detection.

increased into the euxinic range. The minimum value calculated for the study interval was 0.78 at 90.5 ft, indicating that the water at this point in time was the least anoxic. V/Cr ratios greater than 4.25 indicate anoxia (Jones and Manning, 1994). With the exception of the measurements taken at 91.2 and 90.5 ft, where the amount of Cr was below the detection limit of the XRF gun, all V/Cr values remain above 4.25 (Fig. 5.9) showing that the waters were anoxic at the time of deposition. The implications of the negative deflection at 90.5 ft can be confirmed by comparing the paleo-redox proxies to the alginite/(alginite+bituminite) and vitrinite/(vitrinite+bituminite) ratios (Figs. 5.7, 5.8). These ratios do show decreases at this point, which was previously interpreted to indicate a period of enhanced bacterial reworking caused by prolonged exposure to oxygenated water.

Therefore, the paleo-redox proxies and the results of organic petrography confirm each other at this point in the core.

Mo is a very redox-sensitive trace element which can be evaluated as Mo ppm, as an Al-normalized ratio, or as an enrichment factor so that comparisons can be made to "average' shale values. The lower Cleveland has Mo values ranging from 14-150 ppm with an average value of about 90 ppm (Fig. 5.10; Table 5.2). This is an enrichment factor of 15.1 when compared to the average shale which contains 2.6 ppm Mo (Table 5.2). In this section of the Cleveland, Mo values are very sensitive to changes in lithology (Fig. 5.10). The more organic-rich sections of the core have higher ppm values of Mo, higher Al-normalized ratios, and show Mo enrichment relative to the less organic-rich sections of the core. Considering the relationship between Mo and Al, it is possible that the Mo concentration responded to very subtle changes in redox conditions triggered by changing volumes of clastic input.

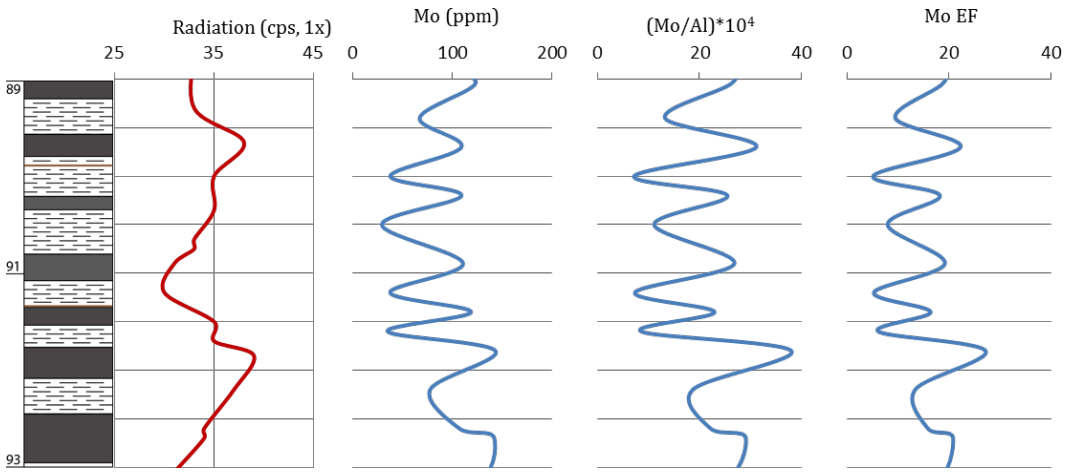


Figure 5. 10. Trace-element paleo-redox proxies, Mo ppm, (Mo/Al)x$10^4$, and Mo enrichment factor. Lithology and gamma-ray curve shown for comparison.

Table 5. 2. Published values for Mo ppm, Al ppm, and Mo-enrichment factors in average shales, average black shales, and the Cleveland Shale in the D2 core.

| Shales | Mo (ppm) | Al (ppm) | EF |
|---|---|---|---|
| **Average Shale (Wedepohl, 1971)** | 2.6 | 71,400 | - |
| **Average Black Shale (Vine and Tourtelot, 1970)** | 10 | 48,800 | 14.3 |
| **Cleveland Shale (this study)** | 89.1 | 43,100 | 15.1 |

While Mo responded to changes in lithology and amount of radioactive material in the Cleveland, neither the V/(V+Ni) nor the V/Cr curve showed parallel high peaks when compared to the synthetic gamma-ray curve. This lack of correlation can be attributed to signal dampening caused by the overwhelming influence of the clay content. While radioactivity in the Cleveland shale primarily varies with the liptinite content (on a mineral-free basis) (Fig. 5.2), it also shows a correlation with the volume of mineral matter, particularly the clay content (Fig. 5.4). This relationship is probably related to the presence of $^{40}K$ in the clay (Durrance, 1986). The clastic proxies, Si/Al, Ti/Al, and K/Al, can be used to better understand that relationship. The results of this study show that these three proxies have approximately parallel curves (Fig. 5.11). The Si/Al ratio shows greater variance than Ti/Al or K/Al ratios; however, the origin of the Si has been called into question with one study suggesting that upwards of 50% of quartz silt in Late Devonian shales is biogenic in origin (Schieber, 2000), and another supporting an eolian origin (Werne et al., 2002). These observations, if true, make drawing conclusions from the Si/Al ratio a questionable undertaking. There is a significant

positive deflection in the clastic proxy curves at 90.5 ft, which indicates an increase in clastic sedimentation at this time. Comparing the location of this deflection with the core lithology shows that this occurred during the deposition of one of the less organic-rich portions of the Cleveland Shale and occurred near the initiation of a fourth-order cycle.

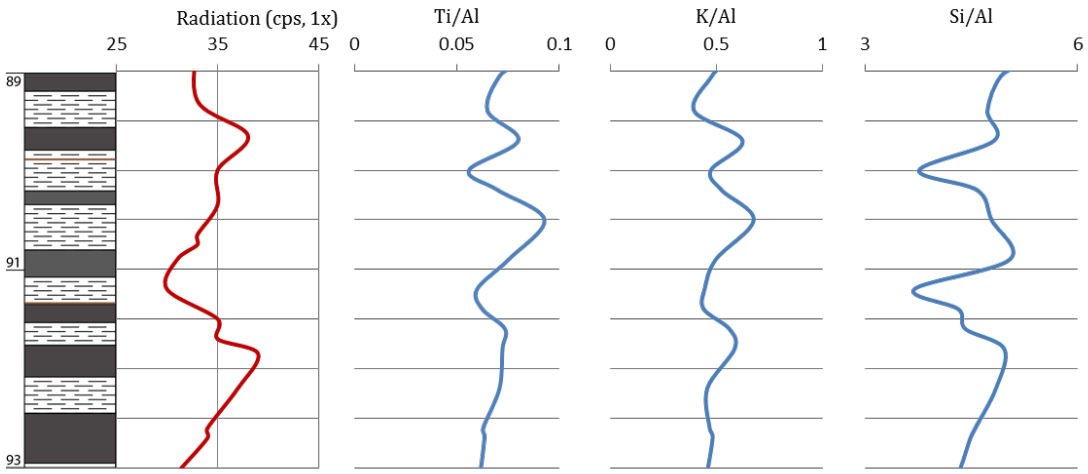


Figure 5. 11. Proxies for clastic influx Ti/Al, K/Al, and Si/Al. Lithology and gamma-ray curve shown for comparison.

Most of the clay minerals in the Cleveland Shale are illite (38%-85%) and expandable clays such as mixed-layer illite-smectite (10%-60%), with kaolinite composing only 2-7% of the clay minerals (Toth, 2004). The association of Al-normalized iron and calcium with K/Al indicates that these elements were most likely incorporated into the structure of the clay minerals (Fig. 5.12). This incorporation has implications for clastic input, because iron is commonly transported into basins as dust-borne particles (Lamy et al., 2014). Hence, where the volume of iron increases, it can be inferred that the volume of eolian dust being deposited in the basin has also increased. The increases in the Fe/Al ratio also

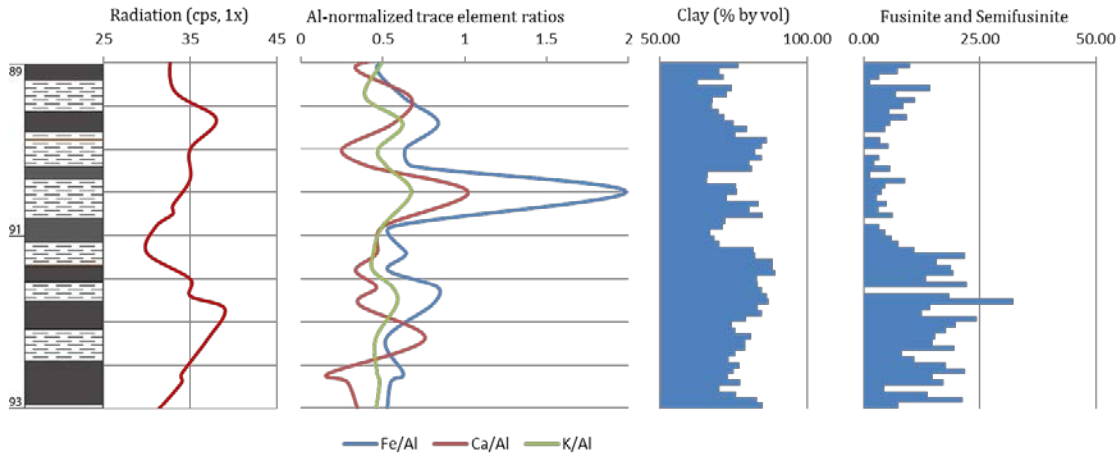


Figure 5. 12. Fe/Al, Ca/Al, and K/Al ratios compared to the volume of clay and windblown inertinite macerals (shown on a mineral-free basis).

correspond to places where the volume of fusinite and semifusinite increases (Fig. 5.12). These macerals were previously established to be related to eolian deposition, supporting the hypothesis that iron was transported into the basin via dust-borne particles. Additionally, increases in the calcium content indicate changes in the clay-mineral composition, as calcium is more commonly found in expandable clays than in illite. Hence, where the Ca/Al ratio is greater than the K/Al ratio, it is likely that expandable clays were being deposited at the expense of illite. The changing clay-mineral composition is likely the result of changing floral dynamics due to the expansion of land plants in the Late Devonian (Algeo et al., 1995, 2001). Increased arborescence (tree stature) and seed habit led to increased depth of root penetration and allowed for the colonization of drier areas (Algeo and Scheckler, 1998), providing fuel for the fires which produced the fusinite and semifusinite observed in the Cleveland (Algeo and Scheckler, 1998; Algeo et al., 2001). These changes would have enhanced chemical weathering on late Devonian land masses,

and increased riverine nutrient flux (Algeo and Scheckler, 1998) which stimulated productivity in the Black Shale Sea.

### 5.4. Depositional model for the Cleveland Shale

Analysis of the D2 core has revealed at least two orders of cyclicity within Milankovitch ranges, the 120-ka fourth-order cycles and the 40-ka fifth-order cycles, in Cleveland Shale (Fig. 5.2). These periodicities correspond to changes in the earth's orbital eccentricity (~100 ka) and obliquity of the earth's axis (~42 ka), respectively (Hays et al., 1976). These cycles, respectively, account for 25 and 50% of climatic variance in the past 450,000 years and have been convincingly correlated with the Quaternary ice ages (Hays et al., 1976; Berger et al., 1984). Similarly, results from this study and others (e.g., Ettensohn et al., 2009a) suggest that sediments in the Cleveland Shale also record evidence for periodic glaciation associated with these cycles.

The proposed depositional model (Fig. 5.13) is apparently related to alternating highstands, which correspond to gamma-ray highs, and lowstands, which correspond to gamma-ray minima. These highstands and lowstands can also be related to lithologies in the Cleveland Shale, as highstands resulted in the formation of the more organic-rich sections of the shale, whereas lowstands contributed to the formation of the less organic-rich intervals. Moreover, the highstands and lowstands seem to be linked through transitional periods, during which either more organic-rich shales or the less organic-rich shales could have formed. The different shale types were apparently related to local climatic variations controlled by Milankovitch-band cyclonic cooling and drying cycles.

These changes have also been identified through observed changes in maceral type and paleo-redox proxies.

Mid-latitude cyclonic activity during latest Famennian time is thought to have contributed to polar transport of moisture and the development of large-scale coastal glaciers in Brazil and Bolivia (Streel et al., 2002). Miospore analysis has shown that the coastal-lowland vegetation associated with these glaciers had a worldwide distribution (Streel et al., 2002); so it is possible that the same processes that led to the formation of coastal glaciers in South America, could have led to the coeval formation of glaciers in Laurussia (North America). The recent discovery of a glacial dropstone in the Cleveland Shale (Ettensohn et al., 2009a) and of coeval tillites in the Appalachian Basin (Brezinski et al., 2010), clearly indicate that glaciation was present during Cleveland deposition. In fact, Ettensohn et al. (2009a) showed that, in places, ancient tillites were deposited on top of shoreface sandstones, indicating that glaciers must have crossed coastal lowlands, perhaps during one of the proposed lowstand periods. This could have been the result of the periodic advance and retreat of mountain glaciers into the coastal lowlands, associated with the alternation between very cold, wet conditions and warmer, dry conditions caused by the cyclonic activity (Streel et al., 2002).

Cold, wet phases of the climatic cycle would have triggered the formation and advance of alpine and piedmont glaciations (Figs. 5.13A, 5.13B). As glaciers began the uptake of oceanic water, lowstand periods started to ensue. Falling sea level during these periods allowed fluvial drainage to bypass estuaries, as the drainage rapidly incised existing topography to reach the sea; this process allows increased

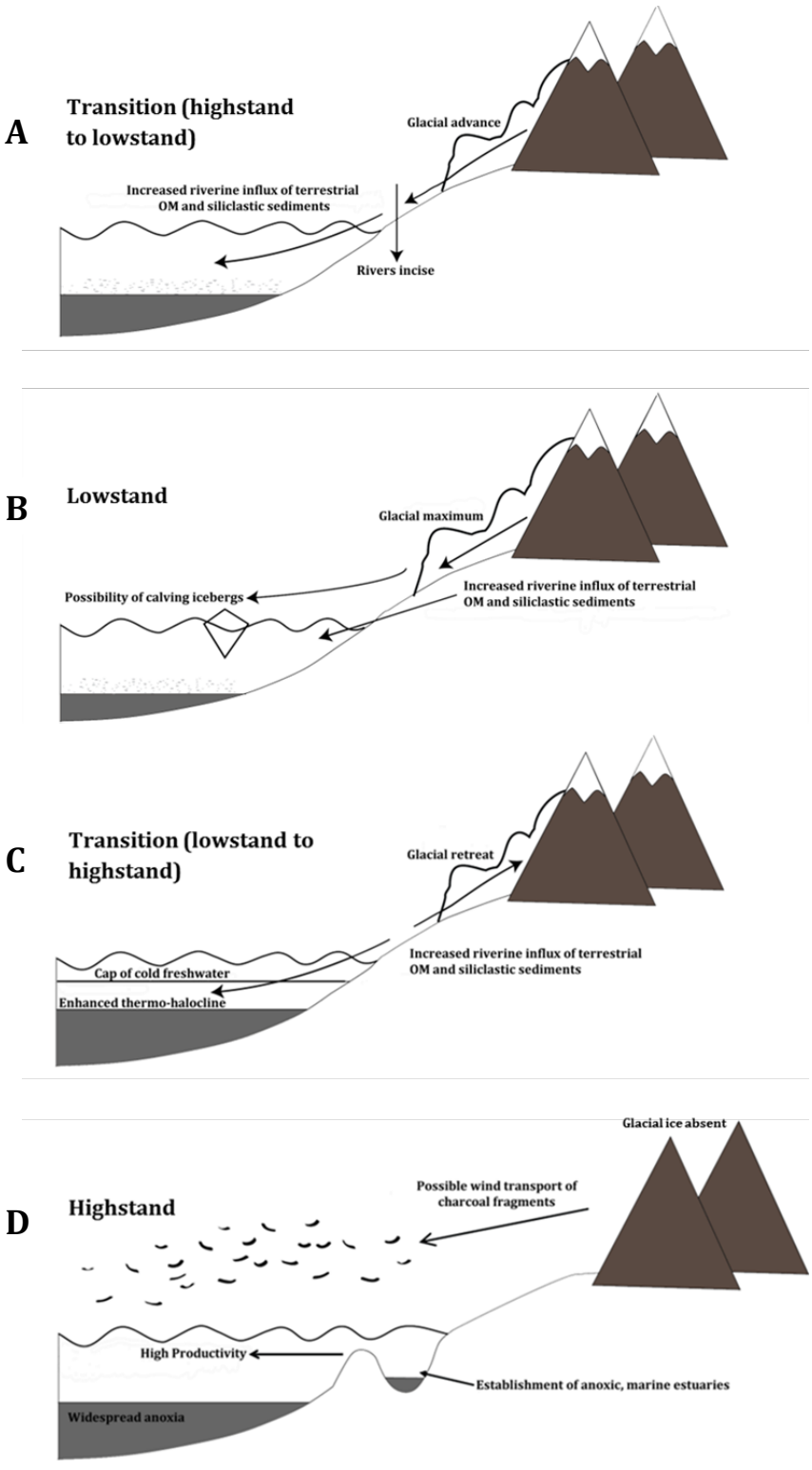


Figure 5. 13. Conditions during each part of the proposed depositional model. A: transition (highstand to lowstand); B: lowstand, cold and wet conditions; C: transition (lowstand to highstand); D: Highstand, warm and dry conditions.

volumes of terrestrial material to be transported into the basin. Therefore, the main identifying characteristic of these lowstand periods is a simultaneous increase in the volume of silicate minerals and terrestrial, detrinite-size macerals (inertodetrinite and vitrodetrinite), the small size of which indicates that depositional processes broke the macerals into increasingly smaller particles as might happen during fluvial transport.

In fact, petrography shows that the relationship between detrinite-size, terrestrial macerals and silicate minerals exhibited two levels of cyclicity, most likely related to periods of increasing fluvial runoff into the Black Shale Sea. Inertodetrinite, vitrodetrinite, and silicate minerals all began entering the sedimentary record in increased volumes between 91.5 and 91 ft, a depth in core that also marks a local gamma-ray minimum and the end of a 120-ka, fourth-order cycle (Figs. 5.2, 5.4, 5.6; Table 5.1). When compared to the lithology of the D2 core (Figs. 5.2, 5.4), it becomes clear that relatively high values for terrestrial, detrinite-size macerals and silicate minerals are related to the less organic-rich sections of the core (Figs. 5.4, 5.6). Lithologic cycles in the D2 core also show 40-ka, fifth-order cyclicity, indicating that changes in the volume of fluvial runoff also occurred on a fifth-order scale (Fig. 5.4). This conclusion is supported by the work of Cotter and Driese (1998) who documented 30-50-ka cyclicity in incised valley-fill deposits in roughly equivalent parts of the Catskill Formation in Pennsylvania. The facies succession in the Catskill Formation shows that sand, plant material, and gravel, in this study identified by the simultaneous increases in the volume of terrestrial, detrinite-size macerals and the volume of silicate minerals, were transported down

incised valleys and spread out onto a shelf depositional ramp during periods of relatively low sea level.

The formation of the more organic-rich sections of the Cleveland Shale can be largely explained by the work of Armstrong et al. (2005), who applied the "expanding puddle" model of black-shale formation, wherein anoxic bottom-water conditions are inferred beneath a stratified water column (Wignall, 1991) during the formation of black shales in Upper Ordovician strata in Jordan. In this model, sea-level rise is triggered by glacial melting that results in the flooding of incised valleys and other shoreline topography, all of which contributes to the rapid expansion of accommodation space and the trapping of sediment in near-shore estuaries (Fig. 5.13D). Hence with the trapping of sediment, sedimentation rates in the basin remain constant or slow, such that the basin becomes sediment-starved and black-shale formation expands outwardly from areas of greatest depth (Wignall, 1991; Armstrong et al., 2005).

Warm, dry climates (Fig. 5.13C, D), on the other hand, are ideal for the establishment of highstand conditions and organic-rich-shale-forming transitional periods, because organic productivity is increased at the ocean surface and bottom-water conditions are anoxic to euxinic. Moreover, as glacial melt water enters the basin and sea level rises during these warm periods, large amounts of nutrients are released into the upper water column, triggering a period of high productivity (Wignall, 1991). This is reflected in the changing volume of liptinite and liptodetrinite macerals (Figs. 4.8, 5.3, 5.6). These macerals are most commonly derived from marine algae, so that an increase in the volume of liptinite macerals

indicates a period of enhanced productivity. Additionally, density-driven circulation declines as the climate warms and glacial ice retreats, resulting in enhanced stratification of the water column (Armstrong et al., 2005). Furthermore, the relative volume of bituminite (Figs. 5.7, 5.8) and paleo-redox trends (Figs. 5.9, 5.10, 5.11, 5.12) provide additional support for the presence of Cleveland bottom-water anoxia. In particular, the results of this study show that the volume of bituminite and sulfide minerals co-vary (Fig. 5.8), as would be expected in anoxic conditions. Hence, sections of the core where large volumes of bituminite and of sulfide minerals occur together are suggestive of a stratified water column and bottom-water anoxia and correspond to the more organic-rich sections of the Cleveland Shale.

As sea level rose, the previously incised valleys were flooded, resulting in the formation of anoxic, marine estuaries in drowned river valleys and sunken coastal topography. Those estuaries would have acted as sediment traps and provided accommodation space for the deposition of coarse-grained silicate minerals and fluvially transported terrestrial detrinite. These periods of highstand sediment trapping would have contributed substantially to sediment starvation so that increasing amounts of marine organic matter (liptinite) and suspended clay minerals get deposited in the deeper, more distal areas of the Appalachian Basin. Such conditions would have resulted in deposition of the darker, more organic-rich intervals identified in the D2 core.

This concept of sea-level change is supported by the correlation between increasing relative volumes of the fusinite and semifusinite macerals (wind-

deposited, fossil charcoal) and liptodetrinite (fragmented algal material) macerals at 91.5 ft. Because the influence of fluvial sedimentation decreased, the importance of windblown debris would have increased. During dry periods, an increase in the volume of inertinite (fusinite and semifusinite) should be expected as charcoal is generated on the adjoining landmass due to the increased incidence of large-scale fires. Fusinite and semifusinite can be transported long distances (hundreds to thousands of km), which has been demonstrated by transport of the macerals with fine, Saharan dust into the Atlantic Ocean (Foda, 1983; Greeley and Iversen, 1985) after the macerals entered the atmosphere as part of a thermally buoyant plume during fires (Clark, 1988). Therefore, the association of fusinite and semifusinite with clay minerals in the lower Cleveland (Figs. 5.4, 5.12) indicates that increased clay sedimentation relates not only to highstand sediment trapping, but also to increased windblown deposition.

Hence, the prominent, decimeter-scale recesses and promontories that characterize the lower Cleveland Shale (Fig. 1.2) are most likely obliquity-related cycles on the scale of about 40-ka years and probably manifest climatic changes that played out in terms of fluvial runoff, eolian influx and sea-level rise. Coeval variation in organic macerals, clastic input and paleo-redox proxies generally support this origin. In contrast, the larger 120-ka, eccentricity-related cycles, shown best on gamma-ray logs (Figs. 4.1, 4.2, 4.3, 5.2), may represent periods of major glacial advance and retreat, in which the "expanding puddle" model of Armstrong et al. (2005) may provide the best explanation. The magnitude of these cycles, moreover,

is of the same scale as those recognized during the Pleistocene advances and retreats (Petit et al., 1999; EPICA Community Members, 2004).

## CHAPTER SIX: CONCLUSIONS

The conclusions of this study address the nature and origin of cyclicity in the Cleveland Shale. The resolution provided by the examination of Cleveland core material provided extensive insight into the association of different organic macerals and mineral materials with depositional pathways. The most important findings of this thesis are as follows:

1. There is a hierarchy of cycles in the Cleveland Shale, which can be related to Milankovitch cyclicity. These include forth-order cycles of 120 ka, representing orbital eccentricity, and 40-ka fifth-order cycles, representing obliquity.
2. Sedimentological changes (source and depositional processes of sediment) were identified through characterization of organic matter in the Cleveland and through x-ray fluorescence of core material.
    a. Detrinite-size organic macerals are related to the presence of silicate minerals and indicate increased fluvial runoff where they occur together.
    b. Fusinite and semifusinite are related to the presence of clay minerals and indicate the increased influence of eolian processes where they occur together.
    c. Increases in the volume of liptinite macerals are related to increases in the volume of clay minerals, which physically protect the organic matter and enhance the preservation of liptinite macerals.

d. The volume of bituminite in these shales is related to paleo-redox conditions and supports the presence of a stratified water column during the deposition of the Cleveland Shale.

3. Periodic glaciation during the deposition of the Cleveland Shale controlled sea-level rise and fall and led to changes in sediment flux into the Appalachian Basin. Increases in detrinite-size organic macerals and silicate minerals apparently represent periods of lowered sea level and the advance of mountain glaciers into coastal lowlands (cold-wet conditions; Fig. 5.13A, B). Periods of increased bituminite formation were related to enhanced water column stratification caused by increased freshwater runoff during periods of glacial melting (warm-dry conditions; Fig 5.13C). Periods of high fusinite and clay-mineral content seem to represent high sea levels during inter-glacial periods. Periods of increased liptinite deposition are also related to periods of high sea level and increased nutrient availability in marine estuaries (warm-dry conditions; Fig 5.13D).

## CHAPTER SEVEN: APPENDICES

### Appendix A: Measured radiation on core (counts per second, 1x) with handheld scintillometer.

**Measured radiation on core (counts per second, 1x)**

| Depth on core (ft) | Radiation (cps, 1x) | Depth on core (ft) | Radiation (cps, 1x) |
|---|---|---|---|
| 49.25 | 25 | 60 | 26 |
| 49.65 | 22 | 60.45 | 29 |
| 50 | 24 | 60.7 | 28 |
| 50.3 | 27 | 60.85 | 22 |
| 50.7 | 25 | 60.95 | 26 |
| 50.9 | 22 | 61.15 | 25 |
| 51.5 | 26 | 61.55 | 27 |
| 51.75 | 24 | 61.8 | 24 |
| 52 | 23 | 62.05 | 23 |
| 52.25 | 23 | 62.25 | 25 |
| 52.55 | 22 | 62.4 | 24 |
| 52.7 | 26 | 62.75 | 28 |
| 52.85 | 25 | 63.2 | 24 |
| 53.1 | 26 | 63.5 | 25 |
| 53.6 | 25 | 63.8 | 22 |
| 53.9 | 22 | 64.1 | 25 |
| 54.3 | 24 | 64.4 | 26 |
| 54.75 | 23 | 64.7 | 23 |
| 55.15 | 21 | 65.3 | 22 |
| 55.4 | 27 | 65.95 | 23 |
| 55.65 | 23 | 66.3 | 21 |
| 56 | 26 | 66.45 | 27 |
| 56.35 | 21 | 66.65 | 26 |
| 56.5 | 25 | 66.9 | 23 |
| 56.7 | 23 | 67.05 | 21 |
| 56.85 | 22 | 67.2 | 23 |
| 57.15 | 20 | 67.35 | 22 |
| 57.55 | 23 | 67.45 | 24 |
| 57.9 | 22 | 67.6 | 21 |
| 58.35 | 24 | 67.75 | 22 |
| 58.75 | 23 | 68.15 | 20 |
| 58.95 | 22 | 68.5 | 23 |
| 59.1 | 23 | 68.6 | 21 |
| 59.25 | 23 | 68.7 | 19 |
| 59.4 | 26 | 68.85 | 24 |
| 59.65 | 25 | 69.2 | 24 |

**Measured radiation on core (counts per second, 1x) (continued)**

| Depth on core (ft) | Radiation (cps, 1x) | Depth on core (ft) | Radiation (cps, 1x) |
|---|---|---|---|
| 69.5 | 23 | 80.35 | 26 |
| 69.75 | 24 | 80.7 | 25 |
| 70 | 21 | 81.4 | 25 |
| 70.2 | 25 | 81.7 | 26 |
| 70.4 | 20 | 81.95 | 27 |
| 70.8 | 22 | 82.4 | 28 |
| 71.2 | 26 | 82.9 | 25 |
| 71.5 | 21 | 83.1 | 22 |
| 71.65 | 25 | 83.5 | 28 |
| 71.85 | 25 | 83.9 | 27 |
| 72.2 | 23 | 84.25 | 27 |
| 72.45 | 28 | 84.55 | 29 |
| 72.6 | 24 | 84.9 | 26 |
| 72.85 | 25 | 85.15 | 27 |
| 73.15 | 22 | 85.45 | 27 |
| 73.35 | 23 | 85.75 | 28 |
| 73.55 | 26 | 86.1 | 26 |
| 73.65 | 25 | 86.45 | 30 |
| 73.95 | 24 | 86.7 | 27 |
| 74.15 | 25 | 86.9 | 28 |
| 74.3 | 24 | 87.35 | 31 |
| 74.5 | 28 | 87.8 | 35 |
| 74.65 | 28 | 88.3 | 31 |
| 74.85 | 23 | 88.65 | 33 |
| 75.7 | 21 | 89.3 | 33 |
| 76 | 27 | 89.65 | 38 |
| 76.3 | 23 | 90 | 35 |
| 76.55 | 24 | 90.35 | 35 |
| 76.8 | 21 | 90.65 | 33 |
| 76.95 | 26 | 90.75 | 33 |
| 77.3 | 23 | 90.9 | 31 |
| 77.8 | 26 | 91.2 | 30 |
| 78.25 | 22 | 91.5 | 35 |
| 78.6 | 24 | 91.7 | 35 |
| 78.7 | 23 | 91.85 | 39 |
| 78.8 | 21 | 92.2 | 37 |
| 79.75 | 26 | 92.6 | 34 |

**Measured radiation on core (counts per second, 1x) (continued)**

| Depth on core (ft) | Radiation (cps, 1x) |
|---|---|
| 92.7 | 34 |
| 93.05 | 31 |
| 93.5 | 33 |
| 93.9 | 32 |
| 94.4 | 36 |
| 94.65 | 35 |
| 94.8 | 33 |
| 94.95 | 31 |
| 95.4 | 27 |
| 95.7 | 31 |
| 96.15 | 29 |
| 96.5 | 30 |
| 96.7 | 30 |
| 96.85 | 29 |
| 97.1 | 27 |

**Appendix B: D2 Core, Organic Petrography, 93–89ft. Sample ID codes (pa, pb, pc, and others) were assigned to each 0.75 in (1.9 cm) segment of the D2 core as it was sectioned for organic petrography.**

**D2 Core, Organic Petrography, 93–89ft**

| | Sample ID code | pa | pb | pc | pd | pe |
|---|---|---|---|---|---|---|
| | **Depth on core (ft)** | **89.00** | **89.07** | **89.14** | **89.21** | **89.28** |
| **Whole-rock percent by volume** | Vitrinite | 3.9 | 5.0 | 3.8 | 2.8 | 2.8 |
| | Vitrodetrinite | 0.0 | 0.6 | 0.2 | 1.3 | 0.0 |
| | **Vitrinite Total** | **3.9** | **5.6** | **4.0** | **4.1** | **2.8** |
| | Fusinite | 1.6 | 1.0 | 0.2 | 0.2 | 1.2 |
| | Semifusinite | 0.0 | 0.0 | 0.2 | 0.0 | 0.2 |
| | Inertodetrinite | 1.2 | 1.4 | 2.0 | 3.4 | 0.8 |
| | **Inertinite Total** | **2.7** | **2.4** | **2.4** | **3.6** | **2.2** |
| | Sporinite | 0.0 | 0.0 | 0.0 | 0.0 | 0.0 |
| | Telalginite | 4.3 | 2.6 | 2.2 | 2.2 | 2.2 |
| | Liptodetrinite | 0.4 | 0.0 | 0.2 | 0.7 | 0.0 |
| | Lamalginite | 4.3 | 2.2 | 1.6 | 0.7 | 1.2 |
| | Bituminite | 0.0 | 0.8 | 1.6 | 1.5 | 1.4 |
| | **Liptinite Total** | **8.9** | **5.6** | **5.5** | **5.2** | **4.7** |
| | Silicates | 1.6 | 8.0 | 10.9 | 13.5 | 5.5 |
| | Sulfides & Phosphates | 6.0 | 8.0 | 5.5 | 10.5 | 10.2 |
| | Carbonate | 0.2 | 0.0 | 0.0 | 0.0 | 0.0 |
| | Clay-rich matrix material | 76.7 | 70.2 | 71.7 | 63.0 | 74.6 |
| | **Mineral Total** | **84.5** | **86.2** | **88.1** | **86.9** | **90.4** |
| | | | | | | |
| **Mineral-free percent by volume** | Vitrinite | 25.0 | 36.2 | 31.7 | 21.4 | 28.6 |
| | Vitrodetrinite | 0.0 | 4.3 | 1.7 | 10.0 | 0.0 |
| | **Vitrinite Total** | **25.0** | **40.6** | **33.3** | **31.4** | **28.6** |
| | Fusinite | 10.0 | 7.2 | 1.7 | 1.4 | 12.2 |
| | Semifusinite | 0.0 | 0.0 | 1.7 | 0.0 | 2.0 |
| | Inertodetrinite | 7.5 | 10.1 | 16.7 | 25.7 | 8.2 |
| | **Inertinite Total** | **17.5** | **17.4** | **20.0** | **27.1** | **22.4** |
| | Sporinite | 0.0 | 0.0 | 0.0 | 0.0 | 0.0 |
| | Telalginite | 27.5 | 18.8 | 18.3 | 17.1 | 22.4 |
| | Liptodetrinite | 2.5 | 0.0 | 1.7 | 5.7 | 0.0 |
| | Lamalginite | 27.5 | 15.9 | 13.3 | 5.7 | 12.2 |
| | Bituminite | 0.0 | 5.8 | 13.3 | 11.4 | 14.3 |
| | **Liptinite Total** | **57.5** | **40.6** | **46.7** | **40.0** | **49.0** |

**D2 Core, Organic Petrography, 93–89ft (continued)**

| | Sample ID code | pf | pg | ph | pi | pi |
|---|---|---|---|---|---|---|
| | **Depth on core (ft)** | **89.34** | **89.41** | **89.48** | **89.55** | **89.62** |
| **Whole-rock percent by volume** | Vitrinite | 2.7 | 4.3 | 1.4 | 2.9 | 3.4 |
| | Vitrodetrinite | 0.0 | 0.8 | 4.5 | 3.7 | 2.4 |
| | **Vitrinite Total** | **2.7** | **5.1** | **5.8** | **6.6** | **5.8** |
| | Fusinite | 0.8 | 1.6 | 1.2 | 0.8 | 1.3 |
| | Semifusinite | 0.0 | 0.0 | 0.0 | 0.0 | 0.0 |
| | Inertodetrinite | 1.6 | 1.8 | 2.3 | 2.3 | 1.7 |
| | **Inertinite Total** | **2.3** | **3.3** | **3.5** | **3.1** | **3.0** |
| | Sporinite | 0.0 | 0.0 | 0.0 | 0.0 | 0.0 |
| | Telalginite | 1.8 | 1.6 | 1.6 | 1.7 | 1.3 |
| | Liptodetrinite | 1.6 | 0.6 | 0.6 | 0.6 | 1.3 |
| | Lamalginite | 0.8 | 1.0 | 0.4 | 1.4 | 2.1 |
| | Bituminite | 2.1 | 2.3 | 1.9 | 0.8 | 0.6 |
| | **Liptinite Total** | **6.2** | **5.5** | **4.5** | **4.5** | **5.3** |
| | Silicates | 7.8 | 11.7 | 10.5 | 7.6 | 6.2 |
| | Sulfides & Phosphates | 8.0 | 6.2 | 8.1 | 8.3 | 7.7 |
| | Carbonate | 0.0 | 0.0 | 0.0 | 0.0 | 0.0 |
| | Clay-rich matrix material | 72.9 | 67.8 | 67.6 | 69.9 | 72.0 |
| | **Mineral Total** | **88.7** | **85.8** | **86.2** | **85.8** | **85.9** |
| | | | | | | |
| **Mineral-free percent by volume** | Vitrinite | 24.1 | 30.1 | 9.9 | 20.5 | 24.0 |
| | Vitrodetrinite | 0.0 | 5.5 | 32.4 | 26.0 | 17.3 |
| | **Vitrinite Total** | **24.1** | **35.6** | **42.3** | **46.6** | **41.3** |
| | Fusinite | 6.9 | 11.0 | 8.5 | 5.5 | 9.3 |
| | Semifusinite | 0.0 | 0.0 | 0.0 | 0.0 | 0.0 |
| | Inertodetrinite | 13.8 | 12.3 | 16.9 | 16.4 | 12.0 |
| | **Inertinite Total** | **20.7** | **23.3** | **25.4** | **21.9** | **21.3** |
| | Sporinite | 0.0 | 0.0 | 0.0 | 0.0 | 0.0 |
| | Telalginite | 15.5 | 11.0 | 11.3 | 12.3 | 9.3 |
| | Liptodetrinite | 13.8 | 4.1 | 4.2 | 4.1 | 9.3 |
| | Lamalginite | 6.9 | 6.8 | 2.8 | 9.6 | 14.7 |
| | Bituminite | 19.0 | 16.4 | 14.1 | 5.5 | 4.0 |
| | **Liptinite Total** | **55.2** | **38.4** | **32.4** | **31.5** | **37.3** |

**D2 Core, Organic Petrography, 93–89ft (continued)**

| | Sample ID code | pk | pl | pm | pn | po |
|---|---|---|---|---|---|---|
| | **Depth on core (ft)** | **89.69** | **89.76** | **89.83** | **89.90** | **89.96** |
| **Whole-rock percent by volume** | Vitrinite | 3.1 | 0.8 | 0.8 | 1.8 | 1.7 |
| | Vitrodetrinite | 1.9 | 2.9 | 2.4 | 0.6 | 0.4 |
| | **Vitrinite Total** | **5.1** | **3.7** | **3.2** | **2.4** | **2.1** |
| | Fusinite | 0.6 | 0.4 | 0.0 | 0.2 | 0.4 |
| | Semifusinite | 0.2 | 0.0 | 0.0 | 0.0 | 0.0 |
| | Inertodetrinite | 2.3 | 1.0 | 2.4 | 1.4 | 0.4 |
| | **Inertinite Total** | **3.1** | **1.4** | **2.4** | **1.6** | **0.8** |
| | Sporinite | 0.0 | 0.0 | 0.0 | 0.0 | 0.0 |
| | Telalginite | 2.3 | 1.2 | 2.4 | 1.0 | 1.7 |
| | Liptodetrinite | 0.8 | 0.6 | 0.4 | 0.4 | 0.4 |
| | Lamalginite | 1.4 | 1.2 | 2.4 | 0.2 | 1.4 |
| | Bituminite | 1.2 | 0.4 | 1.2 | 0.0 | 1.0 |
| | **Liptinite Total** | **5.6** | **3.3** | **6.3** | **1.6** | **4.5** |
| | Silicates | 5.4 | 6.5 | 7.5 | 3.0 | 3.1 |
| | Sulfides & Phosphates | 5.6 | 5.5 | 5.0 | 5.1 | 4.8 |
| | Carbonate | 0.0 | 0.0 | 0.0 | 0.0 | 0.0 |
| | Clay-rich matrix material | 75.1 | 79.6 | 75.6 | 86.3 | 84.7 |
| | **Mineral Total** | **86.2** | **91.6** | **88.1** | **94.5** | **92.6** |
| | | | | | | |
| **Mineral-free percent by volume** | Vitrinite | 22.5 | 9.3 | 6.7 | 32.1 | 23.7 |
| | Vitrodetrinite | 14.1 | 34.9 | 20.0 | 10.7 | 5.3 |
| | **Vitrinite Total** | **36.6** | **44.2** | **26.7** | **42.9** | **28.9** |
| | Fusinite | 4.2 | 4.7 | 0.0 | 3.6 | 5.3 |
| | Semifusinite | 1.4 | 0.0 | 0.0 | 0.0 | 0.0 |
| | Inertodetrinite | 16.9 | 11.6 | 20.0 | 25.0 | 5.3 |
| | **Inertinite Total** | **22.5** | **16.3** | **20.0** | **28.6** | **10.5** |
| | Sporinite | 0.0 | 0.0 | 0.0 | 0.0 | 0.0 |
| | Telalginite | 16.9 | 14.0 | 20.0 | 17.9 | 23.7 |
| | Liptodetrinite | 5.6 | 7.0 | 3.3 | 7.1 | 5.3 |
| | Lamalginite | 9.9 | 14.0 | 20.0 | 3.6 | 18.4 |
| | Bituminite | 8.5 | 4.7 | 10.0 | 0.0 | 13.2 |
| | **Liptinite Total** | **40.8** | **39.5** | **53.3** | **28.6** | **60.5** |

**D2 Core, Organic Petrography, 93–89ft (continued)**

| | Sample ID code | pp | pq | pr | ps | pt |
|---|---|---|---|---|---|---|
| | **Depth on core (ft)** | **90.03** | **90.10** | **90.17** | **90.24** | **90.31** |
| **Whole-rock percent by volume** | Vitrinite | 2.0 | 0.4 | 2.3 | 1.6 | 3.9 |
| | Vitrodetrinite | 1.0 | 1.2 | 1.0 | 0.8 | 1.8 |
| | **Vitrinite Total** | **2.9** | **1.6** | **3.3** | **2.3** | **5.7** |
| | Fusinite | 0.0 | 0.2 | 0.2 | 0.4 | 0.2 |
| | Semifusinite | 0.0 | 0.0 | 0.0 | 0.0 | 0.0 |
| | Inertodetrinite | 1.6 | 1.2 | 1.0 | 0.8 | 1.6 |
| | **Inertinite Total** | **1.6** | **1.4** | **1.2** | **1.2** | **1.8** |
| | Sporinite | 0.0 | 0.0 | 0.0 | 0.0 | 0.0 |
| | Telalginite | 1.6 | 0.8 | 2.7 | 1.2 | 2.3 |
| | Liptodetrinite | 0.8 | 0.6 | 0.8 | 1.2 | 0.8 |
| | Lamalginite | 1.0 | 0.6 | 0.2 | 0.6 | 1.8 |
| | Bituminite | 0.4 | 0.8 | 0.8 | 0.4 | 1.4 |
| | **Liptinite Total** | **3.7** | **2.8** | **4.5** | **3.3** | **6.2** |
| | Silicates | 2.7 | 3.2 | 5.7 | 4.1 | 11.9 |
| | Sulfides & Phosphates | 6.7 | 6.1 | 4.9 | 7.9 | 8.2 |
| | Carbonate | 0.0 | 0.0 | 0.0 | 0.0 | 0.0 |
| | Clay-rich matrix material | 82.4 | 84.8 | 80.5 | 81.2 | 66.3 |
| | **Mineral Total** | **91.8** | **94.1** | **91.0** | **93.2** | **86.4** |
| | | | | | | |
| **Mineral-free percent by volume** | Vitrinite | 23.8 | 6.7 | 26.1 | 22.9 | 28.6 |
| | Vitrodetrinite | 11.9 | 20.0 | 10.9 | 11.4 | 12.9 |
| | **Vitrinite Total** | **35.7** | **26.7** | **37.0** | **34.3** | **41.4** |
| | Fusinite | 0.0 | 3.3 | 2.2 | 5.7 | 1.4 |
| | Semifusinite | 0.0 | 0.0 | 0.0 | 0.0 | 0.0 |
| | Inertodetrinite | 19.0 | 20.0 | 10.9 | 11.4 | 11.4 |
| | **Inertinite Total** | **19.0** | **23.3** | **13.0** | **17.1** | **12.9** |
| | Sporinite | 0.0 | 0.0 | 0.0 | 0.0 | 0.0 |
| | Telalginite | 19.0 | 13.3 | 30.4 | 17.1 | 17.1 |
| | Liptodetrinite | 9.5 | 10.0 | 8.7 | 17.1 | 5.7 |
| | Lamalginite | 11.9 | 10.0 | 2.2 | 8.6 | 12.9 |
| | Bituminite | 4.8 | 13.3 | 8.7 | 5.7 | 10.0 |
| | **Liptinite Total** | **45.2** | **46.7** | **50.0** | **48.6** | **45.7** |

**D2 Core, Organic Petrography, 93–89ft (continued)**

| | Sample ID code | pu | pv | pw | px | py |
|---|---|---|---|---|---|---|
| | **Depth on core (ft)** | **90.38** | **90.45** | **90.52** | **90.58** | **90.65** |
| **Whole-rock percent by volume** | Vitrinite | 4.3 | 1.5 | 3.7 | 1.2 | 1.9 |
| | Vitrodetrinite | 1.9 | 2.3 | 1.4 | 0.8 | 1.0 |
| | **Vitrinite Total** | **6.2** | **3.9** | **5.0** | **2.0** | **2.9** |
| | Fusinite | 1.4 | 0.4 | 0.4 | 0.2 | 0.4 |
| | Semifusinite | 0.0 | 0.0 | 0.0 | 0.0 | 0.0 |
| | Inertodetrinite | 1.9 | 1.0 | 0.6 | 0.8 | 1.0 |
| | **Inertinite Total** | **3.3** | **1.3** | **1.0** | **1.0** | **1.4** |
| | Sporinite | 0.0 | 0.0 | 0.0 | 0.0 | 0.0 |
| | Telalginite | 2.3 | 1.3 | 1.6 | 2.4 | 1.9 |
| | Liptodetrinite | 0.6 | 0.4 | 0.6 | 0.6 | 1.0 |
| | Lamalginite | 1.7 | 0.2 | 1.2 | 0.6 | 0.6 |
| | Bituminite | 1.2 | 1.3 | 0.6 | 0.4 | 0.2 |
| | **Liptinite Total** | **5.8** | **3.3** | **3.9** | **4.1** | **3.7** |
| | Silicates | 10.9 | 7.7 | 6.6 | 5.5 | 2.3 |
| | Sulfides & Phosphates | 7.8 | 7.9 | 7.4 | 14.3 | 6.2 |
| | Carbonate | 0.0 | 0.0 | 0.0 | 0.0 | 0.0 |
| | Clay-rich matrix material | 66.0 | 75.9 | 76.1 | 72.9 | 83.6 |
| | **Mineral Total** | **84.7** | **91.5** | **90.1** | **92.7** | **92.1** |
| | | | | | | |
| **Mineral-free percent by volume** | Vitrinite | 27.8 | 18.2 | 37.3 | 16.7 | 24.4 |
| | Vitrodetrinite | 12.7 | 27.3 | 13.7 | 11.1 | 12.2 |
| | **Vitrinite Total** | **40.5** | **45.5** | **51.0** | **27.8** | **36.6** |
| | Fusinite | 8.9 | 4.5 | 3.9 | 2.8 | 4.9 |
| | Semifusinite | 0.0 | 0.0 | 0.0 | 0.0 | 0.0 |
| | Inertodetrinite | 12.7 | 11.4 | 5.9 | 11.1 | 12.2 |
| | **Inertinite Total** | **21.5** | **15.9** | **9.8** | **13.9** | **17.1** |
| | Sporinite | 0.0 | 0.0 | 0.0 | 0.0 | 0.0 |
| | Telalginite | 15.2 | 15.9 | 15.7 | 33.3 | 24.4 |
| | Liptodetrinite | 3.8 | 4.5 | 5.9 | 8.3 | 12.2 |
| | Lamalginite | 11.4 | 2.3 | 11.8 | 8.3 | 7.3 |
| | Bituminite | 7.6 | 15.9 | 5.9 | 5.6 | 2.4 |
| | **Liptinite Total** | **38.0** | **38.6** | **39.2** | **55.6** | **46.3** |

**D2 Core, Organic Petrography, 93–89ft (continued)**

| | Sample ID code | pz | paa | pbb | pcc | pdd |
|---|---|---|---|---|---|---|
| | **Depth on core (ft)** | **90.72** | **90.79** | **90.86** | **90.93** | **91.00** |
| **Whole-rock percent by volume** | Vitrinite | 1.4 | 1.4 | 2.5 | 5.1 | 5.4 |
| | Vitrodetrinite | 0.6 | 0.8 | 1.9 | 1.6 | 2.0 |
| | **Vitrinite Total** | **1.9** | **2.2** | **4.5** | **6.6** | **7.4** |
| | Fusinite | 0.2 | 0.4 | 0.0 | 0.2 | 0.6 |
| | Semifusinite | 0.0 | 0.0 | 0.0 | 0.2 | 0.0 |
| | Inertodetrinite | 1.4 | 1.6 | 1.9 | 1.6 | 1.8 |
| | **Inertinite Total** | **1.5** | **2.0** | **1.9** | **1.9** | **2.4** |
| | Sporinite | 0.0 | 0.0 | 0.0 | 0.0 | 0.0 |
| | Telalginite | 1.7 | 0.8 | 2.1 | 1.4 | 1.4 |
| | Liptodetrinite | 0.2 | 0.4 | 0.4 | 0.2 | 0.6 |
| | Lamalginite | 0.2 | 0.4 | 1.2 | 0.8 | 0.6 |
| | Bituminite | 0.4 | 0.6 | 1.0 | 0.8 | 0.6 |
| | **Liptinite Total** | **2.5** | **2.2** | **4.7** | **3.1** | **3.2** |
| | Silicates | 6.2 | 3.6 | 9.9 | 9.9 | 13.2 |
| | Sulfides & Phosphates | 7.4 | 5.2 | 7.0 | 7.0 | 6.6 |
| | Carbonate | 0.0 | 0.0 | 0.0 | 0.0 | 0.0 |
| | Clay-rich matrix material | 80.5 | 84.9 | 72.1 | 71.4 | 67.1 |
| | **Mineral Total** | **94.0** | **93.7** | **89.0** | **88.3** | **87.0** |
| | | | | | | |
| **Mineral-free percent by volume** | Vitrinite | 22.6 | 21.9 | 22.8 | 43.3 | 41.5 |
| | Vitrodetrinite | 9.7 | 12.5 | 17.5 | 13.3 | 15.4 |
| | **Vitrinite Total** | **32.3** | **34.4** | **40.4** | **56.7** | **56.9** |
| | Fusinite | 3.2 | 6.3 | 0.0 | 1.7 | 4.6 |
| | Semifusinite | 0.0 | 0.0 | 0.0 | 1.7 | 0.0 |
| | Inertodetrinite | 22.6 | 25.0 | 17.5 | 13.3 | 13.8 |
| | **Inertinite Total** | **25.8** | **31.3** | **17.5** | **16.7** | **18.5** |
| | Sporinite | 0.0 | 0.0 | 0.0 | 0.0 | 0.0 |
| | Telalginite | 29.0 | 12.5 | 19.3 | 11.7 | 10.8 |
| | Liptodetrinite | 3.2 | 6.3 | 3.5 | 1.7 | 4.6 |
| | Lamalginite | 3.2 | 6.3 | 10.5 | 6.7 | 4.6 |
| | Bituminite | 6.5 | 9.4 | 8.8 | 6.7 | 4.6 |
| | **Liptinite Total** | **41.9** | **34.4** | **42.1** | **26.7** | **24.6** |

**D2 Core, Organic Petrography, 93–89ft (continued)**

| | Sample ID code | pee | pff | P30 | P26 | P25 |
|---|---|---|---|---|---|---|
| | **Depth on core (ft)** | **91.07** | **91.14** | **91.20** | **91.27** | **91.34** |
| **Whole-rock percent by volume** | Vitrinite | 4.0 | 3.1 | 3.8 | 1.8 | 1.0 |
| | Vitrodetrinite | 1.1 | 3.1 | 0.0 | 0.0 | 0.0 |
| | **Vitrinite Total** | **5.2** | **6.1** | **3.8** | **1.8** | **1.0** |
| | Fusinite | 0.4 | 0.6 | 1.0 | 1.0 | 1.0 |
| | Semifusinite | 0.4 | 0.4 | 0.4 | 0.2 | 0.0 |
| | Inertodetrinite | 1.7 | 1.0 | 1.4 | 1.0 | 0.8 |
| | **Inertinite Total** | **2.5** | **1.9** | **2.8** | **2.2** | **1.8** |
| | Sporinite | 0.0 | 0.0 | 0.0 | 0.0 | 0.0 |
| | Telalginite | 1.7 | 1.9 | 1.6 | 0.4 | 0.4 |
| | Liptodetrinite | 0.4 | 0.8 | 0.2 | 0.0 | 0.8 |
| | Lamalginite | 1.3 | 0.6 | 3.0 | 1.4 | 0.0 |
| | Bituminite | 1.5 | 1.3 | 1.4 | 0.6 | 0.8 |
| | **Liptinite Total** | **5.0** | **4.6** | **6.2** | **2.4** | **1.9** |
| | Silicates | 12.6 | 11.7 | 0.8 | 0.8 | 0.4 |
| | Sulfides & Phosphates | 6.3 | 5.2 | 4.8 | 4.4 | 5.4 |
| | Carbonate | 0.0 | 0.0 | 0.0 | 0.0 | 0.0 |
| | Clay-rich matrix material | 68.5 | 70.2 | 81.7 | 88.5 | 89.1 |
| | **Mineral Total** | **87.4** | **87.1** | **87.3** | **93.7** | **94.9** |
| | | | | | | |
| **Mineral-free percent by volume** | Vitrinite | 31.8 | 23.9 | 29.7 | 28.1 | 19.2 |
| | Vitrodetrinite | 9.1 | 23.9 | 0.0 | 0.0 | 0.0 |
| | **Vitrinite Total** | **40.9** | **47.8** | **29.7** | **28.1** | **19.2** |
| | Fusinite | 3.0 | 4.5 | 7.8 | 15.6 | 19.2 |
| | Semifusinite | 3.0 | 3.0 | 3.1 | 3.1 | 0.0 |
| | Inertodetrinite | 13.6 | 7.5 | 10.9 | 15.6 | 15.4 |
| | **Inertinite Total** | **19.7** | **14.9** | **21.9** | **34.4** | **34.6** |
| | Sporinite | 0.0 | 0.0 | 0.0 | 0.0 | 0.0 |
| | Telalginite | 13.6 | 14.9 | 12.5 | 6.3 | 7.7 |
| | Liptodetrinite | 3.0 | 6.0 | 1.6 | 0.0 | 15.4 |
| | Lamalginite | 10.6 | 4.5 | 23.4 | 21.9 | 0.0 |
| | Bituminite | 12.1 | 10.4 | 10.9 | 9.4 | 15.4 |
| | **Liptinite Total** | **39.4** | **35.8** | **48.4** | **37.5** | **38.5** |

**D2 Core, Organic Petrography, 93–89ft (continued)**

| | Sample ID code | P24 | P28 | P23 | P22 | P21 |
|---|---|---|---|---|---|---|
| | **Depth on core (ft)** | **91.41** | **91.48** | **91.55** | **91.62** | **91.69** |
| **Whole-rock percent by volume** | Vitrinite | 3.7 | 2.6 | 3.0 | 2.2 | 0.4 |
| | Vitrodetrinite | 0.0 | 0.0 | 0.0 | 0.0 | 0.0 |
| | **Vitrinite Total** | **3.7** | **2.6** | **3.0** | **2.2** | **0.4** |
| | Fusinite | 1.6 | 2.0 | 0.0 | 1.4 | 1.6 |
| | Semifusinite | 0.0 | 0.8 | 0.0 | 0.4 | 0.4 |
| | Inertodetrinite | 1.2 | 1.2 | 1.6 | 0.8 | 0.0 |
| | **Inertinite Total** | **2.7** | **3.9** | **1.6** | **2.6** | **2.0** |
| | Sporinite | 0.0 | 0.0 | 0.0 | 0.0 | 0.0 |
| | Telalginite | 1.4 | 1.0 | 1.0 | 1.0 | 1.4 |
| | Liptodetrinite | 1.8 | 1.4 | 0.4 | 1.0 | 0.0 |
| | Lamalginite | 0.0 | 3.5 | 4.3 | 0.6 | 1.0 |
| | Bituminite | 2.0 | 0.0 | 0.2 | 2.4 | 1.4 |
| | **Liptinite Total** | **5.1** | **5.9** | **5.9** | **4.9** | **3.8** |
| | Silicates | 0.4 | 1.0 | 0.4 | 0.0 | 0.8 |
| | Sulfides & Phosphates | 4.9 | 3.1 | 4.3 | 3.9 | 6.2 |
| | Carbonate | 0.0 | 0.2 | 0.0 | 0.0 | 0.0 |
| | Clay-rich matrix material | 83.0 | 83.3 | 84.6 | 86.4 | 86.8 |
| | **Mineral Total** | **88.3** | **87.6** | **89.3** | **90.4** | **93.8** |
| | | | | | | |
| **Mineral-free percent by volume** | Vitrinite | 31.7 | 20.6 | 27.8 | 22.4 | 6.5 |
| | Vitrodetrinite | 0.0 | 0.0 | 0.0 | 0.0 | 0.0 |
| | **Vitrinite Total** | **31.7** | **20.6** | **27.8** | **22.4** | **6.5** |
| | Fusinite | 13.3 | 15.9 | 0.0 | 14.3 | 25.8 |
| | Semifusinite | 0.0 | 6.3 | 0.0 | 4.1 | 6.5 |
| | Inertodetrinite | 10.0 | 9.5 | 14.8 | 8.2 | 0.0 |
| | **Inertinite Total** | **23.3** | **31.7** | **14.8** | **26.5** | **32.3** |
| | Sporinite | 0.0 | 0.0 | 0.0 | 0.0 | 0.0 |
| | Telalginite | 11.7 | 7.9 | 9.3 | 10.2 | 22.6 |
| | Liptodetrinite | 15.0 | 11.1 | 3.7 | 10.2 | 0.0 |
| | Lamalginite | 0.0 | 28.6 | 40.7 | 6.1 | 16.1 |
| | Bituminite | 16.7 | 0.0 | 1.9 | 24.5 | 22.6 |
| | **Liptinite Total** | **43.3** | **47.6** | **55.6** | **51.0** | **61.3** |

**D2 Core, Organic Petrography, 93–89ft (continued)**

| | Sample ID code | P20 | P19 | P18 | P17 | P16 |
|---|---|---|---|---|---|---|
| | **Depth on core (ft)** | **91.76** | **91.82** | **91.89** | **91.96** | **92.03** |
| **Whole-rock percent by volume** | Vitrinite | 2.8 | 2.4 | 4.9 | 8.2 | 4.9 |
| | Vitrodetrinite | 0.0 | 0.0 | 0.0 | 0.0 | 0.0 |
| | **Vitrinite Total** | **2.8** | **2.4** | **4.9** | **8.2** | **4.9** |
| | Fusinite | 1.4 | 1.3 | 2.8 | 2.7 | 2.7 |
| | Semifusinite | 0.0 | 0.0 | 0.4 | 1.2 | 0.2 |
| | Inertodetrinite | 1.6 | 0.0 | 0.0 | 0.0 | 0.0 |
| | **Inertinite Total** | **3.0** | **1.3** | **3.2** | **3.9** | **2.9** |
| | Sporinite | 0.0 | 0.0 | 0.0 | 0.0 | 0.0 |
| | Telalginite | 0.4 | 1.1 | 1.2 | 2.2 | 0.8 |
| | Liptodetrinite | 3.0 | 0.0 | 0.0 | 0.0 | 0.0 |
| | Lamalginite | 0.0 | 2.9 | 1.8 | 2.3 | 2.1 |
| | Bituminite | 0.6 | 2.6 | 2.2 | 2.7 | 5.4 |
| | **Liptinite Total** | **4.0** | **6.6** | **5.3** | **7.2** | **8.3** |
| | Silicates | 1.4 | 0.7 | 1.4 | 1.0 | 0.8 |
| | Sulfides & Phosphates | 5.5 | 4.0 | 5.9 | 4.9 | 7.0 |
| | Carbonate | 0.0 | 0.2 | 0.0 | 0.0 | 0.0 |
| | Clay-rich matrix material | 83.4 | 84.5 | 79.3 | 74.4 | 75.7 |
| | **Mineral Total** | **90.3** | **89.4** | **86.6** | **80.2** | **83.5** |
| | | | | | | |
| **Mineral-free percent by volume** | Vitrinite | 28.6 | 22.9 | 36.4 | 41.6 | 29.4 |
| | Vitrodetrinite | 0.0 | 0.0 | 0.0 | 0.0 | 0.0 |
| | **Vitrinite Total** | **28.6** | **22.9** | **36.4** | **41.6** | **29.4** |
| | Fusinite | 14.3 | 12.5 | 21.2 | 13.9 | 16.5 |
| | Semifusinite | 0.0 | 0.0 | 3.0 | 5.9 | 1.2 |
| | Inertodetrinite | 16.3 | 0.0 | 0.0 | 0.0 | 0.0 |
| | **Inertinite Total** | **30.6** | **12.5** | **24.2** | **19.8** | **17.6** |
| | Sporinite | 0.0 | 0.0 | 0.0 | 2.0 | 2.4 |
| | Telalginite | 4.1 | 10.4 | 9.1 | 10.9 | 4.7 |
| | Liptodetrinite | 30.6 | 0.0 | 0.0 | 0.0 | 0.0 |
| | Lamalginite | 0.0 | 27.1 | 13.6 | 11.9 | 12.9 |
| | Bituminite | 6.1 | 25.0 | 16.7 | 13.9 | 32.9 |
| | **Liptinite Total** | **40.8** | **62.5** | **39.4** | **36.6** | **50.6** |

**D2 Core, Organic Petrography, 93–89ft (continued)**

| | Sample ID code | P15 | P14 | P13 | P12 | P11 |
|---|---|---|---|---|---|---|
| | **Depth on core (ft)** | **92.10** | **92.17** | **92.24** | **92.31** | **92.38** |
| **Whole-rock percent by volume** | Vitrinite | 7.5 | 7.0 | 9.0 | 11.5 | 14.1 |
| | Vitrodetrinite | 0.0 | 0.0 | 0.0 | 0.0 | 0.0 |
| | **Vitrinite Total** | **7.5** | **7.0** | **9.0** | **11.5** | **14.1** |
| | Fusinite | 1.8 | 2.2 | 2.7 | 1.4 | 1.6 |
| | Semifusinite | 0.4 | 0.0 | 0.2 | 0.0 | 0.6 |
| | Inertodetrinite | 0.0 | 0.0 | 0.0 | 0.0 | 0.0 |
| | **Inertinite Total** | **2.2** | **2.2** | **2.9** | **1.4** | **2.2** |
| | Sporinite | 0.0 | 0.0 | 0.0 | 0.0 | 0.0 |
| | Telalginite | 0.6 | 2.0 | 1.4 | 1.4 | 1.4 |
| | Liptodetrinite | 0.0 | 0.0 | 0.0 | 0.0 | 0.0 |
| | Lamalginite | 2.6 | 3.4 | 1.8 | 2.6 | 2.2 |
| | Bituminite | 1.4 | 0.0 | 0.0 | 0.0 | 0.4 |
| | **Liptinite Total** | **4.5** | **5.4** | **3.1** | **4.0** | **4.0** |
| | Silicates | 0.0 | 0.4 | 0.0 | 0.0 | 0.0 |
| | Sulfides & Phosphates | 4.9 | 6.0 | 6.1 | 7.5 | 6.4 |
| | Carbonate | 0.0 | 0.0 | 0.0 | 0.0 | 0.0 |
| | Clay-rich matrix material | 80.9 | 78.9 | 78.9 | 75.6 | 73.3 |
| | **Mineral Total** | **85.9** | **85.3** | **85.0** | **83.2** | **79.7** |
| | | | | | | |
| **Mineral-free percent by volume** | Vitrinite | 52.8 | 47.3 | 59.7 | 68.2 | 69.6 |
| | Vitrodetrinite | 0.0 | 0.0 | 0.0 | 0.0 | 0.0 |
| | **Vitrinite Total** | **52.8** | **47.3** | **59.7** | **68.2** | **69.6** |
| | Fusinite | 12.5 | 14.9 | 18.2 | 8.2 | 7.8 |
| | Semifusinite | 2.8 | 0.0 | 1.3 | 0.0 | 2.9 |
| | Inertodetrinite | 0.0 | 0.0 | 0.0 | 0.0 | 0.0 |
| | **Inertinite Total** | **15.3** | **14.9** | **19.5** | **8.2** | **10.8** |
| | Sporinite | 0.0 | 0.0 | 0.0 | 0.0 | 0.0 |
| | Telalginite | 4.2 | 13.5 | 9.1 | 8.2 | 6.9 |
| | Liptodetrinite | 0.0 | 0.0 | 0.0 | 0.0 | 0.0 |
| | Lamalginite | 18.1 | 23.0 | 11.7 | 15.3 | 10.8 |
| | Bituminite | 9.7 | 0.0 | 0.0 | 0.0 | 2.0 |
| | **Liptinite Total** | **31.9** | **36.5** | **20.8** | **23.5** | **19.6** |

**D2 Core, Organic Petrography, 93–89ft (continued)**

| | Sample ID code | P10 | P9 | P8 | P7 | P6 |
|---|---|---|---|---|---|---|
| | **Depth on core (ft)** | **92.45** | **92.51** | **92.58** | **92.65** | **92.72** |
| **Whole-rock percent by volume** | Vitrinite | 6.8 | 1.6 | 2.8 | 1.6 | 6.6 |
| | Vitrodetrinite | 0.0 | 0.0 | 0.0 | 0.0 | 0.0 |
| | **Vitrinite Total** | **6.8** | **1.6** | **2.8** | **1.6** | **6.6** |
| | Fusinite | 2.9 | 2.2 | 1.4 | 1.4 | 0.8 |
| | Semifusinite | 0.2 | 0.2 | 0.2 | 0.0 | 0.0 |
| | Inertodetrinite | 0.0 | 0.0 | 0.0 | 0.0 | 0.0 |
| | **Inertinite Total** | **3.1** | **2.4** | **1.6** | **1.4** | **0.8** |
| | Sporinite | 0.0 | 0.0 | 0.0 | 0.0 | 0.0 |
| | Telalginite | 1.5 | 3.7 | 2.1 | 1.9 | 4.5 |
| | Liptodetrinite | 0.0 | 0.3 | 0.3 | 0.6 | 0.9 |
| | Lamalginite | 3.3 | 0.6 | 1.2 | 0.3 | 1.2 |
| | Bituminite | 2.2 | 2.5 | 2.1 | 0.9 | 1.8 |
| | **Liptinite Total** | **7.0** | **7.1** | **5.7** | **3.8** | **8.5** |
| | Silicates | 0.2 | 8.4 | 7.2 | 7.5 | 9.7 |
| | Sulfides & Phosphates | 5.5 | 4.0 | 7.5 | 6.3 | 6.1 |
| | Carbonate | 0.0 | 0.0 | 0.0 | 0.0 | 0.0 |
| | Clay-rich matrix material | 77.0 | 74.9 | 73.2 | 77.4 | 70.3 |
| | **Mineral Total** | **82.7** | **87.3** | **88.0** | **91.2** | **86.1** |
| | | | | | | |
| **Mineral-free percent by volume** | Vitrinite | 39.2 | 14.5 | 25.9 | 19.5 | 36.7 |
| | Vitrodetrinite | 0.0 | 0.0 | 0.0 | 0.0 | 0.0 |
| | **Vitrinite Total** | **39.2** | **14.5** | **25.9** | **19.5** | **36.7** |
| | Fusinite | 16.5 | 20.0 | 13.0 | 17.1 | 4.4 |
| | Semifusinite | 1.3 | 1.8 | 1.9 | 0.0 | 0.0 |
| | Inertodetrinite | 0.0 | 0.0 | 0.0 | 0.0 | 0.0 |
| | **Inertinite Total** | **17.7** | **21.8** | **14.8** | **17.1** | **4.4** |
| | Sporinite | 0.0 | 0.0 | 0.0 | 0.0 | 0.0 |
| | Telalginite | 8.9 | 29.3 | 17.5 | 21.4 | 32.6 |
| | Liptodetrinite | 0.0 | 2.4 | 2.5 | 7.1 | 6.5 |
| | Lamalginite | 19.0 | 4.9 | 10.0 | 3.6 | 8.7 |
| | Bituminite | 12.7 | 19.5 | 17.5 | 10.7 | 13.0 |
| | **Liptinite Total** | **40.5** | **56.1** | **47.5** | **42.9** | **60.9** |

**D2 Core, Organic Petrography, 93–89ft (continued)**

| | Sample ID code | P5 | P4 | P3 |
|---|---|---|---|---|
| | **Depth on core (ft)** | **92.79** | **92.86** | **93.00** |
| **Whole-rock percent by volume** | Vitrinite | 6.5 | 3.9 | 3.9 |
| | Vitrodetrinite | 1.1 | 0.0 | 0.0 |
| | **Vitrinite Total** | **7.6** | **3.9** | **3.9** |
| | Fusinite | 2.3 | 2.7 | 0.8 |
| | Semifusinite | 0.0 | 0.0 | 0.0 |
| | Inertodetrinite | 1.5 | 2.3 | 1.5 |
| | **Inertinite Total** | **3.8** | **5.0** | **2.3** |
| | Sporinite | 0.0 | 0.0 | 0.0 |
| | Telalginite | 2.7 | 1.2 | 1.5 |
| | Liptodetrinite | 0.4 | 0.4 | 0.8 |
| | Lamalginite | 2.3 | 1.2 | 1.2 |
| | Bituminite | 0.0 | 1.2 | 0.8 |
| | **Liptinite Total** | **5.3** | **3.9** | **4.2** |
| | Silicates | 1.1 | 1.9 | 0.8 |
| | Sulfides & Phosphates | 6.1 | 2.3 | 3.9 |
| | Carbonate | 0.0 | 0.0 | 0.0 |
| | Clay-rich matrix material | 76.0 | 82.9 | 84.9 |
| | **Mineral Total** | **83.2** | **87.2** | **89.6** |
| | | | | |
| **Mineral-free percent by volume** | Vitrinite | 38.6 | 30.3 | 37.0 |
| | Vitrodetrinite | 6.8 | 0.0 | 0.0 |
| | **Vitrinite Total** | **45.5** | **30.3** | **37.0** |
| | Fusinite | 13.6 | 21.2 | 7.4 |
| | Semifusinite | 0.0 | 0.0 | 0.0 |
| | Inertodetrinite | 9.1 | 18.2 | 14.8 |
| | **Inertinite Total** | **22.7** | **39.4** | **22.2** |
| | Sporinite | 0.0 | 0.0 | 0.0 |
| | Telalginite | 15.9 | 9.1 | 14.8 |
| | Liptodetrinite | 2.3 | 3.0 | 7.4 |
| | Lamalginite | 13.6 | 9.1 | 11.1 |
| | Bituminite | 0.0 | 9.1 | 7.4 |
| | **Liptinite Total** | **31.8** | **30.3** | **40.7** |

**Appendix C: Major– and Trace–Element Inventories, readings taken from TYCO portable XRF gun on loan to KGS from CIMAREX; gun set to 75 sec for three filters; 30 sec, 30 sec, 15 sec.**

**Major– and Trace–Element Inventories**

| Reading Number | 1400 | 1399 | 1398 | 1397 | 1396 | 1388 | 1387 |
|---|---|---|---|---|---|---|---|
| Depth on core (ft) | 86.1 | 87.5 | 88.1 | 88.5 | 88.85 | 89.05 | 89.4 |
| Si | 203163 | 213861 | 128260 | 260652 | 191858 | 231862 | 240866 |
| Al | 35975.5 | 39023.6 | 27262 | 51400.3 | 35987.9 | 47148.3 | 50950.7 |
| Ti | 2917.35 | 3049.81 | 2474.13 | 3410.78 | 2953.01 | 3338.26 | 3307.53 |
| Zr | 135.28 | 145.39 | 109.72 | 159.34 | 148.17 | 144.87 | 142.48 |
| Rb | 79.87 | 78.51 | 98.1 | 76.07 | 81.31 | 83.54 | 81.58 |
| Th | 13.83 | 14.44 | 14.69 | 17.47 | 17.78 | 17.74 | 17.26 |
| K | 20768 | 20179.7 | 20278.6 | 21679.1 | 19549.3 | 22534 | 20089.2 |
| Pb | 18.26 | 13.71 | 25.13 | 16.14 | 18.12 | 14.02 | 32.01 |
| Ni | 95.4 | 116.97 | 109.81 | 84.74 | 94.69 | 115.61 | 115.17 |
| Fe | 23248.6 | 24143.2 | 39855.3 | 18337.1 | 24099.5 | 21859.6 | 31959.4 |
| Cr | 71 | 69.75 | < LOD | 90.46 | 45.98 | 114.16 | 92.83 |
| Nb | 16.18 | 17.43 | 15.72 | 18.48 | 17.28 | 18.79 | 20.07 |
| S | 75146.5 | 89069.4 | 83285.5 | 64040 | 111442 | 71397.4 | 109189 |
| Zn | 132.25 | 127.22 | 198.45 | 141.06 | 138.17 | 126.13 | 113 |
| V | 496 | 439 | 453.89 | 483.94 | 487.66 | 529.61 | 559.52 |
| U | 44.47 | 50.91 | 30.31 | 46.16 | 41.55 | 46.74 | 45.58 |
| Mo | 128.43 | 153.3 | 58.95 | 123.79 | 98.97 | 123.22 | 67.5 |
| Mn | 222.63 | < LOD | 236.83 | 236.08 | 201.77 | 162.9 | 558.37 |
| Ca | 17292 | 19668.1 | 20877.3 | 16519.6 | 26947.4 | 15683.2 | 34162.8 |
| Bal | 609168 | 578483 | 662902 | 551437 | 574646 | 574064 | 494532 |
| Sr | 79.86 | 73.41 | 79.96 | 70.4 | 84.49 | 79.32 | 80.8 |
| Bi | 11.02 | 9.86 | 10.21 | 15.73 | 12.89 | 14.45 | 13.88 |
| Cl | 507.22 | 520.9 | 529.63 | 516.2 | 526.03 | 523.16 | 736.84 |
| Se | < LOD | 6.07 | < LOD | < LOD | < LOD | < LOD | 6.99 |
| As | 12.02 | 15.25 | 28.79 | 13.69 | 11.15 | 14.94 | 38.1 |
| Hg | < LOD | < LOD | < LOD | < LOD | < LOD | < LOD | < LOD |
| Au | < LOD | < LOD | 8.99 | < LOD | < LOD | < LOD | < LOD |
| Cu | < LOD | 40.15 | 23.45 | 48.4 | 27.59 | 30.43 | 50.85 |

**Major– and Trace–Element Inventories (continued)**

| Reading Number | 1386 | 1385 | 1384 | 1383 | 1382 | 1395 | 1394 |
|---|---|---|---|---|---|---|---|
| Depth on core (ft) | 89.7 | 90 | 90.2 | 90.5 | 90.9 | 91.2 | 91.4 |
| Si | 169547 | 198974 | 196674 | 126820 | 208544 | 189616 | 224001 |
| Al | 35153.7 | 52863.4 | 42934.4 | 26504.1 | 41361.4 | 51316.4 | 51895.4 |
| Ti | 2810.95 | 2953.29 | 3003.04 | 2456.07 | 3110.36 | 3069.24 | 3238.59 |
| Zr | 129.51 | 100.94 | 134.18 | 114.12 | 139.49 | 114.8 | 132.74 |
| Rb | 86.79 | 97.99 | 88.69 | 90.36 | 83.11 | 101.17 | 86.54 |
| Th | 14.79 | 21.37 | 16.38 | 12.63 | 16.97 | 18.53 | 17.92 |
| K | 21871.2 | 25006.1 | 22477.8 | 17879.9 | 20526.7 | 22770.7 | 22830.3 |
| Pb | 23.47 | 23.42 | 21.05 | 40.27 | 15.16 | 25.16 | 24.57 |
| Ni | 88.38 | 76.89 | 90.65 | 95.31 | 71.99 | 89.72 | 108.39 |
| Fe | 29525.2 | 33653 | 29267.2 | 52599.2 | 22817.4 | 33045.4 | 27631 |
| Cr | 51.57 | 59.32 | 84.68 | < LOD | 65.32 | < LOD | 81.34 |
| Nb | 16.61 | 13.44 | 18.77 | 13.82 | 16.81 | 15.81 | 16.89 |
| S | 106462 | 70586 | 88794.6 | 118372 | 86507.4 | 106026 | 84360.8 |
| Zn | 105.66 | 121.01 | 119.56 | 61.68 | 132.89 | 69.82 | 90.84 |
| V | 431.04 | 488.86 | 431.87 | 347.33 | 526.28 | 398.18 | 446.88 |
| U | 40.62 | 26.34 | 37.38 | 30.73 | 41.88 | 30.87 | 35.64 |
| Mo | 109.51 | 38.06 | 109.49 | 29.52 | 111.11 | 37.84 | 119.15 |
| Mn | 224.63 | 203.79 | 249.41 | 235.39 | 172.54 | 257.15 | 286.67 |
| Ca | 19916.1 | 13292.5 | 17645.1 | 27070.9 | 20627.2 | 23880 | 17351.1 |
| Bal | 601156 | 589614 | 585708 | 613152 | 584252 | 556045 | 555120 |
| Sr | 87.47 | 79.08 | 75.69 | 106.83 | 93.44 | 97.67 | 95.22 |
| Bi | 10.65 | 17.94 | 13.55 | < LOD | 13.07 | 12.68 | 14.83 |
| Cl | 518.73 | 740.1 | 437.05 | 536.57 | 582.85 | 487.88 | 573.89 |
| Se | < LOD | < LOD | < LOD | < LOD | < LOD | < LOD | < LOD |
| As | 12.45 | 26.93 | 19.26 | 44.22 | 14.31 | 28.31 | 19.36 |
| Hg | < LOD | < LOD | < LOD | < LOD | < LOD | < LOD | 8.9 |
| Au | < LOD | 7.12 | < LOD | < LOD | < LOD | < LOD | 8.33 |
| Cu | 41.31 | 36.86 | 36.34 | 39.54 | 23.6 | 34.67 | 32.91 |

**Major– and Trace–Element Inventories (continued)**

| Reading Number | 1393 | 1392 | 1391 | 1390 | 1389 | 1375 | 1374 |
|---|---|---|---|---|---|---|---|
| Depth on core (ft) | 91.6 | 91.8 | 92.2 | 92.6 | 92.7 | 93.2 | 93.5 |
| Si | 181595 | 187502 | 202172 | 220547 | 219624 | 216036 | 215713 |
| Al | 41128.4 | 37784.6 | 41708.2 | 48408.6 | 48948.4 | 51271.4 | 58436 |
| Ti | 3020.77 | 2730.14 | 2952.61 | 3040.91 | 3106.22 | 3063.58 | 3045.78 |
| Zr | 122.42 | 130.71 | 149.91 | 149.3 | 130.85 | 126.35 | 120.52 |
| Rb | 94.42 | 82.34 | 79.31 | 83.57 | 87.59 | 89.62 | 96.37 |
| Th | 14.73 | 12.32 | 18.2 | 16.38 | 19.24 | 15.84 | 18.44 |
| K | 23041.3 | 22097.5 | 19030.2 | 22639.2 | 23576.1 | 22681.8 | 23784.7 |
| Pb | 25.84 | 20.91 | 18.02 | 15.49 | 20.44 | 22.37 | 25.81 |
| Ni | 76.12 | 87.56 | 77.11 | 105.32 | 127.5 | 124.4 | 91.26 |
| Fe | 34391.7 | 30353.7 | 21631 | 30337.1 | 26850.7 | 26652.1 | 28979.6 |
| Cr | 49.92 | 64.66 | 47.73 | 53.03 | 78.13 | 82.99 | 61.74 |
| Nb | 15.95 | 16.9 | 18.27 | 18.32 | 19.46 | 18.02 | 16.57 |
| S | 102727 | 94125.1 | 99649.7 | 76727.8 | 76687.9 | 88287.2 | 109875 |
| Zn | 90.52 | 114.78 | 249.94 | 172.43 | 163.77 | 93.76 | 63.5 |
| V | 421.79 | 332.43 | 511.64 | 485.98 | 511.53 | 480.87 | 478.3 |
| U | 33.65 | 45.59 | 48.74 | 45.06 | 53.15 | 46.46 | 26.62 |
| Mo | 35.32 | 143.63 | 78.02 | 107.38 | 142.44 | 122.2 | 14.46 |
| Mn | 213.64 | 178.4 | 277.26 | 224.28 | 264.6 | 222.67 | 309.42 |
| Ca | 19008.2 | 13414.9 | 31584.1 | 7999.37 | 14059.7 | 19852.9 | 31392 |
| Bal | 580750 | 598106 | 569345 | 576480 | 573722 | 558932 | 515110 |
| Sr | 85.88 | 82.56 | 73.04 | 84.67 | 97.29 | 89.46 | 99.32 |
| Bi | 14.56 | 9.72 | 15.09 | 11.64 | 16.09 | 12.48 | 17.71 |
| Cl | 538.9 | 798.22 | 480.21 | 446.98 | 535.11 | 552.64 | 474.57 |
| Se | < LOD | < LOD | < LOD | < LOD | < LOD | < LOD | < LOD |
| As | 22.26 | 16.71 | 19.61 | 20.91 | 12.14 | 14.32 | 21.52 |
| Hg | 9.29 | < LOD | < LOD | 10.99 | < LOD | < LOD | < LOD |
| Au | < LOD | < LOD | < LOD | < LOD | < LOD | < LOD | 6.36 |
| Cu | 32.67 | 34.94 | 45.27 | 32.41 | 29.11 | 36.83 | 47.02 |

**Major– and Trace–Element Inventories (continued)**

| Reading Number | 1373 | 1372 |
|---|---|---|
| Depth on core (ft) | 93.9 | 94.5 |
| Si | 195033 | 136472 |
| Al | 43448.9 | 29249.6 |
| Ti | 3124.79 | 2360.24 |
| Zr | 124.48 | 117.58 |
| Rb | 87.35 | 93.37 |
| Th | 15.44 | 19.08 |
| K | 22490.7 | 18849.4 |
| Pb | 18.55 | 36.88 |
| Ni | 95.49 | 94.42 |
| Fe | 25602.6 | 39489.7 |
| Cr | 83.26 | 75.31 |
| Nb | 16.75 | 13.4 |
| S | 61274 | 104966 |
| Zn | 131.93 | 41.34 |
| V | 770.07 | 418.97 |
| U | 28.79 | 16.61 |
| Mo | 82.24 | 14.49 |
| Mn | 203.48 | 246.81 |
| Ca | 16315.6 | 29729.2 |
| Bal | 619341 | 624124 |
| Sr | 96.37 | 117.63 |
| Bi | 13.58 | 14.46 |
| Cl | 703.33 | 473.94 |
| Se | 5.61 | 7.32 |
| As | 16.37 | 25.75 |
| Hg | < LOD | < LOD |
| Au | < LOD | 9.12 |
| Cu | 30.6 | 42.42 |

| Clusters | Distance | Leader | Joiner |
|---|---|---|---|
| 19 | 0.00010063 | Th | Nb |
| 18 | 0.00019881 | Pb | As |
| 17 | 0.00032717 | Th | Pb |
| 16 | 0.00035477 | Rb | Sr |
| 15 | 0.00074080 | Rb | Ni |
| 14 | 0.00083769 | Th | U |
| 13 | 0.00153015 | Zr | Zn |
| 12 | 0.00165056 | Rb | Mo |
| 11 | 0.00164064 | Zr | Rb |
| 10 | 0.00294152 | Zr | Th |
| 9 | 0.00496293 | V | Cl |
| 8 | 0.01666735 | Zr | V |
| 7 | 0.10534565 | Ti | Zr |
| 6 | 0.28985562 | K | Ca |
| 5 | 0.39491428 | K | Fe |
| 4 | 0.80864284 | Al | K |
| 3 | 1.05203126 | Al | Ti |
| 2 | 3.14678015 | Al | S |
| 1 | 7.03686201 | Si | Al |

## REFERENCES


Algeo, T. J., Berner, R. A., Maynard, J. B., and Scheckler, S. E., 1995, Late Devonian oceanic anoxic events and biotic crises: "Rooted" in the evolution of vascular land plants: GSA Today, v. 5, no. 3, p. 63-66.

Algeo, T. J., and Scheckler, S. E., 1998, Terrestrial-marine teleconnections in the Devonian: links between the evolution of land plants, weathering processes, and marine anoxic events: Philosophical Transactions of the Royal Society of London. Series B: Biological Sciences, v. 353, no. 1365, p. 113-130.

Algeo, T. J., Scheckler, S. E., and Maynard, J. B., 2001, Effects of the Middle to Late Devonian spread of vascular land plants on weathering regimes, marine biotas, and global climate: Plants invade the land: Evolutionary and environmental perspectives, p. 213-236.

Araujo, C. V., Mendonca-Filho., J. G., Menezes, T., Flores, D., Kalaitzids, S., Zivotic, D., Misz-Kennan, M., Sykorova, I., Hamor-Vido, M., Suarez-Ruiz, I., Hackley, P., Kommeren, K., and Borrego, A. G., 2010, Identification of dispersed organic matter in working group, *in* Kus, J., convenor, 2009 Round Robin Exercise - Final Report: Hanover, ICCP Commission II, 11 p.

Armstrong, H. A., Turner, B. R., Makhlouf, I. M., Weedon, G. P., Williams, M., Al Smadi, A., and Abu Salah, A., 2005, Origin, sequence stratigraphy and depositional environment of an upper Ordovician (Hirnantian) deglacial black shale, Jordan: Palaeogeography, Palaeoclimatology, Palaeoecology, v. 220, no. 3, p. 273-289.

Becker, R. T., Gradstein, F. M., and Hammer, O., 2012, Chapter 22 - The Devonian Period, *in* Gradstein, F. M., Ogg, J. G., Schmitz, M. D., and Ogg, G. M., eds., The Geologic Time Scale: Boston, Elsevier, p. 559-601.

Berger, A., Imbrie, J., Hays, J., Kukla, G., and Saltzman, B., 1984, Milankovitch and climate: Understanding the response to orbital forcing: Boston, D. Reidel Publishing Company, 329 p.

Berry, C. M., and Fairon-Demaret, M., 2001, The middle Devonian flora revisited: Plants invade the land: evolutionary and environmental perspectives. Columbia University Press, New York, p. 120-139.

Bertrand, P., Shimmield, G., Martinez, P., Grousset, F., Jorissen, F., Paterne, M., Pujol, C., Bouloubassi, I., Menard, P. B., Peypouquet, J. P., Beaufort, L., Sicre, M. A., Lallier-Verges, E., Foster, J. M., and Ternois, Y., 1996, The glacial ocean productivity hypothesis: the importance of regional temporal and spatial studies: Marine Geology, v. 130, no. 1–2, p. 1-9.

Bjerstedt, T. W., and Kammer, T. W., 1988, Genetic stratigraphy and depositional systems of the Upper Devonian-Lower Mississippian Price-Rockwell deltaic complex in the Central Appalachians, USA: Sedimentary Geology, v. 54, no. 4, p. 265-301.

Boyle, E. A., 1983, Chemical accumulation variations under the Peru current during the past 130,000 years: Journal of Geophysical Research, v. 88, no. C12, p. 7667-7680.

Brezinski, D. K., Cecil, C. B., and Skema, V. W., 2010, Late Devonian glacigenic and associated facies from the central Appalachian Basin, eastern United States: Geological Society of America Bulletin., v. 52, no. 1, p. 265-281.
Brezinski, D. K., Cecil, C. B., Skema, V. W., and Kertis, C. A., 2009, Evidence for long-term climate change in Upper Devonian strata of the central Appalachians: Palaeogeography, Palaeoclimatology, Palaeoecology, v. 284, no. 3–4, p. 315-325.
Brezinski, D. K., Cecil, C. B., Skema, V. W., and Stamm, R., 2008, Late Devonian glacial deposits from the eastern United States signal an end of the mid-Paleozoic warm period: Palaeogeography, Palaeoclimatology, Palaeoecology, v. 268, no. 3–4, p. 143-151.
Cadée, G. C., 1978, Primary production and chlorophyll in the Zaire river, estuary and plume: Netherlands Journal of Sea Research, v. 12, no. 3–4, p. 368-381.
Canfield, D. E., 1994, Factors influencing organic carbon preservation in marine sediments: Chemical Geology, v. 114, no. 3, p. 315-329.
Caputo, M. V., 1985, Late Devonian glaciation in South America: Palaeogeography, Palaeoclimatology, Palaeoecology, v. 51, no. 1, p. 291-317.
Clark, J. S., 1988, Particle motion and the theory of charcoal analysis: source area, transport, deposition, and sampling: Quaternary Research, v. 30, no. 1, p. 67-80.
Conant, L. C., and Swanson, V. E., 1961, Chattanooga Shale and related rocks of central Tennessee and nearby areas: Geological Survey Professional Paper, v. 357, 91 p.
Cotter, E., and Driese, S. G., 1998, Incised-valley fills and other evidence of sea-level fluctuations affecting deposition of the Catskill Formation (Upper Devonian), Appalachian foreland basin, Pennsylvania: Journal of Sedimentary Research, v. 68, no. 2, p. 347-361.
Durrance, E. M., 1986, Radioactivity in geology: Principles and applications, Chichester [West Sussex]; New York, Ellis Horwood; Halsted Press, 441 p.
Elrick, M., Berkyová, S., Klapper, G., Sharp, Z., Joachimski, M., and Frýda, J., 2009, Stratigraphic and oxygen isotope evidence for My-scale glaciation driving eustasy in the Early–Middle Devonian greenhouse world: Palaeogeography, Palaeoclimatology, Palaeoecology, v. 276, no. 1, p. 170-181.
Elrick, M., and Scott, L. A., 2010, Carbon and oxygen isotope evidence for high-frequency (10^4-10^5yr) and My-scale glacio-eustasy in Middle Pennsylvanian cyclic carbonates (Gray Mesa Formation), central New Mexico: Palaeogeography, Palaeoclimatology, Palaeoecology, v. 285, no. 3, p. 307-320.
EPICA Community Members, 2004, Eight glacial cycles from an Antarctic ice core: Nature, v. 429, no. 6992, p. 623-628.
Ettensohn, F. R., 1985, The Catskill delta complex and the Acadian orogeny: A model: Geological Society of America Special Papers, v. 201, p. 39-50.
Ettensohn, F. R., 1995, Global and regional controls on the origin and burial of organic matter in Devonian-Mississippian black shales of North America: Houston Geological Society Bulletin, v. 37, p. 12-17.

Ettensohn, F. R., 2008, Chapter 4, The Appalachian Foreland Basin in Eastern United States, *in* Miall, A., ed., The sedimentary basins of United States and Canada: Sedimentary Basins of the World, Elsevier, Amsterdam, v. 5, no. C, p. 105-179.

Ettensohn, F. R., Fulton, L. P., and Kepferle, R. C., 1979, Use of scintillometer and gamma-ray logs for correlation and stratigraphy in homogeneous black shales: Summary: Geological Society of America Bulletin, v. 90, no. 5, p. 421-423.

Ettensohn, F. R., and Lierman, R. T., 2012, Large-scale tectonic controls on the origin of paleozoic dark-shale source-rock basins: Examples from the Appalachian foreland-basin, eastern United States, *in* Gao, D., ed., Tectonics and sedimentation: Implications for Petroleum Systems: American Association of Petroleum Geologists Memoir 100, p. 95-124.

Ettensohn, F.R., Lierman, R.T., and Mason, C.E., 2009a, Upper Devonian–Lower Mississippian clastic rocks in northeastern Kentucky: Evidence for Acadian alpine glaciation and models for source-rock and reservoir-rock development in the eastern United States, Guidebook, Spring Field Trip, April 18, 2009: American Institute for Professional Geologists-Kentucky Section, Lexington, 64 p.

Ettensohn, F.R., Lierman, T.R., and Mason, C.E., 2009b, Inferences from a glacial dropstone in Late Devonian black shales, Eastern Kentucky, U.S.A., in Pascussi, V., and Andreucci, S., eds., Book of Abstracts, 27th International Association of Sedimentologists (IAS), Meeting: Sassari, Editrice Democratica Sarda, p. 506.

Ettensohn, F.R., Lierman, R.T., Mason, C.E., and Anderson, E.D., 2008, Kentucky dropstone "ices" the case for Late Devonian alpine glaciation in the central Appalachians: Implications for Appalachian tectonics and black-shale sedimentation, *in* Upper Devonian–Lower Mississippian clastic rocks in northeastern Kentucky: Evidence for Acadian alpine glaciation and models for source-rock and reservoir-rock development in the eastern United States, Ettensphn, F. R., Lierman, R. T., and Mason, C. E., Guidebook, Spring Field Trip, April 18, 2009: American Institute for Professional Geologists-Kentucky Section, Lexington, p. 29-34.

Ettensohn, F. R., Miller, M., Dillman, S., Elam, T., Geller, K., Swager, D., Markowitz, G., Woock, R., and Barron, L., 1988, Characterization and implications of the Devonian-Mississippian black shale sequence, eastern and central Kentucky, USA: Pycnoclines, transgression, regression, and tectonism, *in* McMillan, N.J., Embry, A.F., and Glass, D.J., eds., Devonian of the World, Proceedings of the Second International Symposium on the Devonian System: Canadian Society of Petroleum Geologists Memoir 14, v. 1, p. 277-301.

Fertl, W., 1983, Gamma ray spectral logging: a new evaluation frontier Part III--Measuring source rock potential: World Oil, v. 196, no. 6, p. 147-155.

Filer, J. K., 1994, High frequency eustatic and siliciclastic sedimentation cycles in a foreland basin, Upper Devonian, Appalachian basin, *in* Dennison, J. M., and Ettensohn, F. R., eds., Tectonic and eustatic controls on sedimentary cycles, SEPM Concepts in Sedimentology and Paleontology 4, p. 133–145

Foda, M. A., 1983, Dry-fall of fine dust on sea: Journal of Geophysical Research: Oceans (1978–2012), v. 88, no. C10, p. 6021-6026.
Frakes, L. A., Francis, J. E., and Syktus, J. I., 1992, Climate modes of the Phanerozoic, Cambridge, Cambridge University Press, 274 p.
Gibbs, R. J., 1967, The geochemistry of the Amazon River system: Part I. The factors that control the salinity and the composition and concentration of the suspended solids: Geological Society of America Bulletin, v. 78, no. 10, p. 1203-1232.
Gibbs, R. J., 1980, Wind-controlled coastal upwelling in the western equatorial Atlantic: Deep Sea Research Part A. Oceanographic Research Papers, v. 27, no. 10, p. 857-866.
Greeley, R., and Iversen, J. D., 1985, Wind as a geological process: on Earth, Mars, Venus and Titan, Cambridge, Cambridge University Press, 333 p.
Hackley, P. C., 2011, ICCP working group identification of primary vitrinite in shale 2011 report: Porto, ICCP Commission II, 16 slides.
Hatch, J., and Leventhal, J., 1992, Relationship between inferred redox potential of the depositional environment and geochemistry of the Upper Pennsylvanian (Missourian) Stark Shale Member of the Dennis Limestone, Wabaunsee County, Kansas, USA: Chemical Geology, v. 99, no. 1, p. 65-82.
Hawkins, S. J., 2006, Fossil charcoal in Devonian-Mississippian shales: Implications for the expansion of land plants, paleo-atmospheric oxygen levels and organic-rich black shale accumulation (unpublished M.S. thesis): University of Kentucky, Lexington, 151 p.
Hays, J. D., Imbrie, J., and Shackleton, N. J.,1976 Variations in the Earth's orbit: Pacemaker of the ice ages: Science, v. 194, no. 4270, pp. 1121–1132
Hedges, J. I., Clark, W. A., and Cowie, G. L., 1988, Fluxes and reactivities of organic matter in a coastal marine bay: Limnology & Oceanography, v. 33, no. 5, p. 1137-1152.
Huffman, E., 1977, Performance of a new automatic carbon-dioxide coulometer: Microchemical Journal, v. 22, no. 4, p. 567-573.
Hutton, A., Bharati, S., and Robl, T., 1994, Chemical and petrographic classification of kerogen/macerals: Energy & Fuels, v. 8, no. 6, p. 1478-1488.
Hutton, A. C., 1987, Petrographic classification of oil shales: International Journal of Coal Geology, v. 8, no. 3, p. 203-231.
International Committee for Coal Petrology, 1976, International handbook of coal petrography, Second supplement to the 2nd edition; Paris, Centre National de la Recherche Scientifique.
International Committee for Coal and Organic Petrography, 1998, The new vitrinite classification (ICCP System 1994): Fuel, v. 77, p. 349-358.
International Committee for Coal and Organic Petrography, 2001, The new inertinite classification (ICCP System 1994): Fuel, v. 80, p. 459-471.
Jaminski, J., Algeo, T. J., Maynard, B., and Hower, J. C., 1998, Climatic origin of dm-scale compositional cyclicity in the Cleveland Member of the Ohio Shale (Upper Devonian), Central Appalachian Basin, USA, *in* Schiber, J., Zimmerle, W., and Sethi, P. S., eds., Shales and Mudstones, Stuttgart, v. 1, pp. 217–242.

Joachimski, M. M., Breisig, S., Buggisch, W., Talent, J. A., Mawson, R., Gereke, M., Morrow, J. R., Day, J., and Weddige, K., 2009, Devonian climate and reef evolution: Insights from oxygen isotopes in apatite: Earth and Planetary Science Letters, v. 284, no. 3-4, p. 599-609.

Jones, B., and Manning, D. A., 1994, Comparison of geochemical indices used for the interpretation of palaeoredox conditions in ancient mudstones: Chemical Geology, v. 111, no. 1, p. 111-129.

Jones, T. P., and Chaloner, W. G., 1991, Fossil charcoal, its recognition and palaeoatmospheric significance: Global and Planetary Change, v. 5, no. 1–2, p. 39-50.

Jones, T. P., Scott, A. C., and Cope, M., 1991, Reflectance measurements and the temperature of formation of modern charcoals and implications for studies of fusain: Bulletin - Societe Geologique de France, v. 162, no. 2, p. 193-200.

Kepferle, R. C., Wilson, E. N., and Ettensohn, F. R., 1978, Preliminary stratigraphic cross section showing radioactive zones in the Devonian black shales in the southern part of the Appalachian Basin: U.S. Geological Survey.

Lamy, F., Gersonde, R., Winckler, G., Esper, O., Jaeschke, A., Kuhn, G., Ullermann, J., Martinez-Garcia, A., Lambert, F., and Kilian, R., 2014, Increased Dust Deposition in the Pacific Southern Ocean During Glacial Periods: Science, v. 343, no. 6169, p. 403-407.

Mendonça Filho, J., Araujo, C., Borrego, A., Cook, A., Flores, D., Hackley, P., Hower, J., Kern, M., Kommeren, K., and Kus, J., 2010, Effect of concentration of dispersed organic matter on optical maturity parameters:: Interlaboratory results of the organic matter concentration working group of the ICCP: International Journal of Coal Geology, v. 84, no. 3, p. 154-165.

Milici, R. C., Ryder, R. T., Swezey, C. S., Charpentier, R. R., Cook, T. A., Crovelli, R. A., Klett, T. R., Pollastro, R. M., and Schenk, C. J., 2003, Assessment of undiscovered oil and gas resources of the Appalachian Basin Province, 2002. USGS National Assessment of Oil and Gas Fact Sheet (FS-009-03).

Mitchum., R. M., Jr., and Van Wagoner, J. C., 1991, High-frequency sequences and their stacking patterns: sequence-stratigraphic evidence of high-frequency eustatic cycles: Sedimentary Geology, v. 70, no. 2, p. 131-160.

Over, D. J., Lazar, R., Baird, G. C., Schieber, J., and Ettensohn, F. R., 2009, *Protosalvinia* Dawson and associated conodonts of the upper *trachytera* Zone, Famennian, Upper Devonian, in the eastern United States: Journal of Paleontology, v. 83, no. 1, p. 70-79.

Petit, J. R., Jouzel, J., Raynaud, D., Barkov, N. I., Barnola, J. M., Basile, I., Bender, M., Chappellaz, J., Davis, M., Delaygue, G., Delmotte, M., Kotlyakov, V. M., Legrand, M., Lipenkov, V. Y., Lorius, C., Pepin, L., Ritz, C., Saltzman, E., and Stievenard, M., 1999, Climate and atmospheric history of the past 420,000 years from the Vostok ice core, Antarctica: Nature, v. 399, no. 6735, p. 429-436.

Piper, D. Z., and Calvert, S. E., 2009, A marine biogeochemical perspective on black shale deposition: Earth Science Reviews., v. 95, no. 1, p. 63.

Pontolillo, J., and Stanton, R., 1994, Coal petrographic laboratory procedures and safety manual II: US Geological Survey Open File Report, p. 94-631.

Rider, M. H., 1986, The geological interpretation of well logs: Glasgow [Strathclyde], Blackie, 175 p.
Rimmer, S. M., 2004, Geochemical paleoredox indicators in Devonian–Mississippian black shales, central Appalachian Basin (USA): Chemical Geology, v. 206, no. 3, p. 373-391.
Rimmer, S. M., Cantrell, D. J., and Gooding, P. J., 1993, Rock-eval pyrolysis and vitrinite reflectance trends in the Cleveland Shale Member of the Ohio Shale, eastern Kentucky: Organic Geochemistry, v. 20, no. 6, p. 735-745.
Rimmer, S. M., Thompson, J. A., Goodnight, S. A., and Robl, T. L., 2004, Multiple controls on the preservation of organic matter in Devonian–Mississippian marine black shales: geochemical and petrographic evidence: Palaeogeography, Palaeoclimatology, Palaeoecology, v. 215, no. 1, p. 125-154.
Robl, T., Taulbee, D., Barron, L., and Jones, W., 1987, Petrologic chemistry of a Devonian type II kerogen: Energy & Fuels, v. 1, no. 6, p. 507-513.
Robl, T. L., Rimmer, S. M., and Barron, L. S., 1992, Organic petrography of Mississippian and Devonian shales in east-central Kentucky: Fuel, v. 71, no. 3, p. 267-271.
Sageman, B. B., Murphy, A. E., Werne, J. P., Ver Straeten, C. A., Hollander, D. J., and Lyons, T. W., 2003, A tale of shales: The relative roles of production, decomposition, and dilution in the accumulation of organic-rich strata, Middle–Upper Devonian, Appalachian Basin: Chemical Geology, v. 195, no. 1, p. 229-273.
Schieber, J., Krinsley, D., and Riciputi, L., 2000, Diagenetic origin of quartz silt in mudstones and implications for silica cycling: Nature, v. 406, no. 6799, p. 981-985.
Sevon, W., 1969, The Pocono Formation in northeastern Pennsylvania, Guidebook, 34th Annual Field Conference of Pennsylvania Geologists, October 3-4, 1969: Pennsylvania Geological Survey, Harrisburg, PA, 129 p.
Sevon, W., 1979, Polymictic diamictite in the Spechty Kopf and Rockwell Formations, *in* Proceedings Devonian Shales in South-Central Pennsylvania and Maryland: 44th Annual Conference of Pennsylvania Geologists: Harrisburg, Pennsylvania, Pennsylvania Geological Survey, p. 61-66.
Sevon, W., Woodrow, D., Costolnick, D., Richardson, J., and Attrep Jr, M., 1997, Convulsive geologic events and the origin of diamictite in the Spechty Kopf Formation in northeastern Pennsylvania, *in* Proceedings Geology of the Wyoming–Lackawanna Valley and Its Mountain Rim, Northeastern Pennsylvania: 62nd Annual Conference of Pennsylvania Geologists: Harrisburg, Pennsylvania, Pennsylvania Geological Survey, p. 34-131.
Sherwood, N. R., and Cook, A. C., 1984, Low Rank Oil Shales. Part 1 – Organic Petrology: The University of Wollongong, Department of Geology, Final Project Report to the Department of National Development and Energy on NERD & D Program Project 79/9014, 320 p.
Shimmield, G. B., 1992, Can sediment geochemistry record changes in coastal upwelling palaeoproductivity? Evidence from northwest Africa and the Arabian Sea, *in* Summerhayes, C. P., Prell, W. L., and Emeis, K. C., eds.,

Upwelling Systems: Evolution since the Early Miocene, Geological Society of London Special Publications, vol. 64, p. 29–46.
Smith, J. A., Bentley, M. J., Hodgson, D. A., Roberts, S. J., Leng, M. J., Lloyd, J. M., Barrett, M. S., Bryant, C., and Sugden, D. E., 2007, Oceanic and atmospheric forcing of early Holocene ice shelf retreat, George VI Ice Shelf, Antarctica Peninsula: Quaternary Science Reviews, v. 26, no. 3, p. 500-516.
Stasiuk, L., and Goodarzi, F., 1988, Organic Petrology of Second White Speckled Shale, Saskatchewan, Canada-A Possible Link Between Bituminite and Biogenic Gas?: Bulletin of Canadian Petroleum Geology, v. 36, no. 4, p. 397-406.
Streel, M., Caputo, M. V., Loboziak, S., and Melo, J. H. G., 2000, Late Frasnian–Famennian climates based on palynomorph analyses and the question of the Late Devonian glaciations: Earth-Science Reviews, v. 52, no. 1, p. 121-173.
Taulbee, D. N., Seibert, E. D., Barron, L. S., and Robl, T. L., 1990, Comparison of maceral group chemistries for a New Albany and an Ohio oil shale kerogen: Energy & Fuels, v. 4, no. 3, p. 254-263.
Teichmüller, M., 1974, Über neue Macerale der Liptinit-Gruppe und die Entstehung von Micrinits: Fortschritte in der Geologie von Rheinland und Westfalen, v. 243, p. 37-64.
Teichmüller, M., 1986, Organic petrology of source rocks, history and state of the art: Organic Geochemistry, v. 10, no. 1, p. 581-599.
Teichmüller, M., 1998, Chapter 4, The nature of organic matter - macerals and associated minerals, *in* Taylor, G., and Glick, D., 1998, Organic petrology: A new handbook incorporating some revised parts of Stach's textbook of coal petrology, Gebrüder Borntraeger, p. 175-275.
Teichmüller, M., and Durand, B., 1983, Fluorescence microscopical rank studies on liptinites and vitrinites in peat and coals, and comparison with results of the rock-eval pyrolysis: International Journal of Coal Geology, v. 2, no. 3, p. 197-230.
Teichmüller, M., Ottenjann, K., 1977, Art und Diagenese von Liptiniten und lipoiden Stoffen in einem Erdölmuttergestein auf Grund fluoreszenzmikroskopischer Untersuchungen: Erdöl Kohle, v. 30, p. 387–398.
Thiessen, R., 1925, Microscopic examination of Kentucky oil shales: Oil shales of Kentucky. Kentucky Geological Survey Series VI, v. 21, p. 1-48.
Toth, K. S., 2004, The role of clay-mineral surface area in the accumulation of organic carbon in marine shales (unpublished M.S. thesis): University of Kentucky, Lexington, 155 p.
Van Bennekom, A. J., Berger, G. W., Helder, W., and De Vries, R. T. P., 1978, Nutrient distribution in the Zaire estuary and river plume: Netherlands Journal of Sea Research, v. 12, no. 3–4, p. 296-323.
Vine, J. D., and Tourtelot, E. B., 1970, Geochemistry of black shale deposits; a summary report: Economic Geology, v. 65, no. 3, p. 253-272.
Wedepohl, K., 1971, Environmental influences on the chemical composition of shales and clays: Physics and Chemistry of the Earth, v. 8, p. 305-333.

Werne, J. P., Sageman, B. B., Lyons, T. W., and Hollander, D. J., 2002, An integrated assessment of a "type euxinic" deposit: Evidence for multiple controls on black shale deposition in the middle Devonian Oatka Creek Formation: American Journal of Science, v. 302, p. 110-143.

Wignall, P. B., 1991, Model for transgressive black shales?: Geology, v. 19, no. 2, p. 167-170.

Woodrow, D., Dennison, J., Ettensohn, F., Sevon, W., and Kirchgasser, W., 1988, Middle and Upper Devonian stratigraphy and paleogeography of the central and southern Appalachians and eastern Midcontinent, USA, *in* McMillan, N.J., Embry, A.F., and Glass, D.J., eds., Devonian of the World, Proceedings of the Second International Symposium on the Devonian System: Canadian Society of Petroleum Geologists Memoir 14, v. 1, p 277-301.

Ziegler, W., 1960, Conodonten aus dem Rheinischen Unterdevon (Gedinnian) des Remscheider Sattels (Rheinisches Schiefergebirge): Paläontologische Zeitschrift, v. 34, no. 2, p. 169-201.

Ziegler, W., and Sandberg, C. A., 1990, The Late Devonian standard conodont zonation: Courier Forschungsinstitut Senckenberg, Frankfurt, v. 121, 115 p.

## VITA

Alice C. O'Bryan

Education:
B.S., Geology, Northern Kentucky University

Professional Positions:

| | |
|---|---|
| 08/11-08/14 | Graduate Research and Teaching Assistant, University of Kentucky |
| 06/13-08/13 | Geological Technology Intern, ConocoPhillips |
| 06/11-08/11 | Biological Sciences Laboratory Technician, U.S. Environmental Protection Agency |

Scholastic and Professional Honors:
Pioneer Natural Resources Fellowship (August 2013)
Pirtle Fellowship (May 2012, May 2013)
Outstanding Teaching Assistant Award (May 2012)

Professional Publications:
Saikia, B., Ward, L. O., Hower, J. C., Leao, D. F., Johnston, M. N., **O'Bryan, A. C.**, Sharma, A., Baruah, B., and Silva, L. F., Geochemistry and nano-mineralogy of feed coals, mine overburden, and coal-derived fly ashes from Assam (North-east India): Potentially recoverable rare earth elements in fly ash: Fuel, in Review

Student Full Name: Alice Capri O'Bryan